ULTRASONIC ASSISTED DRILLING

BY

SIMON, SHUET FUNG, CHANG

Simon Chang

A Thesis

Submitted to the School of Graduate Studies

in Partial Fulfillment of the Requirements

for the Degree

Master of Applied Science

McMaster University

March 2003

MASTER OF ENGINEERING (2003) McMaster University

(Mechanical Engineering) Hamilton, Ontario

TITLE: Ultrasonic Assisted Drilling

AUTHOR: Simon, Shuet Fung, Chang, B. Eng. (Mech. Eng.)

McMaster University

SUPERVISOR: Dr. M. Elbestawi

Dr. G. Bone

NUMBER OF PAGES: xi, 111

ABSTRACT

Accuracy and surface finishes play an important role in modern industry. However, the deformability of ductile materials induces challenges in achieving high accuracy and surface finish. Undesired projections of material produced during metal cutting, known as burrs, significantly reduces the accuracy of the parts and affect both the assembly process and product quality. Around 30% of total production costs are used for deburring processes. This thesis presents one modern and promising method in reducing burr size through the use of ultrasonic assistance. With ultrasonic assistance, high frequency vibrations are added in the feed direction during cutting. In particular, ultrasonic assisted drilling of 1100-0 aluminum using high speed steel standard twist drills was investigated.

Two simulation studies were conducted. Firstly, a finite element model of orthogonal cutting with and without ultrasonic assistance was developed. The results predicted that ultrasonic assistance should produce smaller burrs for the simulated operating conditions. Secondly, a drilling exit burr model was created based on a circular plate deflection model. Unfortunately this simulation failed to predict the experimentally observed burr sizes and thus the model requires further development.

To provide the ultrasonic vibration a preloaded workpiece holder and a drive circuit were designed and implemented for use with a commercial piezoelectric actuator. This equipment was cost effective (costing about 400 CAN$) and functional.

The effects of ultrasonic assistance under different vibration and cutting conditions were investigated experimentally. The experimental results demonstrated that, for certain combinations of vibration frequency and amplitude, burr size reduction can be achieved. Under these conditions the ultrasonic impact actions become significant, causing chip segmentation and smaller burrs. The results also show that ultrasonic assisted drilling allows a higher spindle speed and feed to be used without increasing burr size. However, ultrasonic assistance has a negative impact on tool life. Compared with conventional drilling, chipping of the chisel edge and greater wear of the cutting lips was observed after drilling 10 holes. This situation may be improved in the future if drills with suitable coating are used in place of the standard high speed steel drills.

ACKNOWLEDGEMENTS

Thank God my Lord for His guidance and providence throughout these years.

I would like to express my gratitude to both of my supervisors Dr. M. Elbestawi, who has provided grateful guidance and support throughout the duration of this work, and Dr. G. Bone, who has provided his experienced advises and guidance, which contributed significantly to the success of this.work.

I would also like to express my appreciations to Dr. S. Veldhuis and Dr. D. Metezger for their support in vibration control and modeling techniques respectively.

My appreciations are also extended to Ron Lodewyks, Dave Schick and Andrew Buyers, who have shared their valuable experiences in machining; Joe Verhaeghe, who has shared his specialized experience in electronics and circuit analysis; Warren Renold, who has provided his guidance in operating the machines; and Miky Dumitrescu, who has provided her guidance regarding all measuring equipments.

I wish to thank my parents, who have given me tremendous support throughout the duration of this work. Finally, special thanks to my colleagues, who have always been supportive and encouraging.

TABLE OF CONTENTS

LIST OF FIGURES

LIST OF TABLES

CHAPTER 1

INTRODUCTION

Drilling ductile materials has always been a challenge to industry because of the formations of burrs. Burrs are defined as undesirable projections of material resulting from plastic deformation as the cutting tool approaches an edge (see Fig. 1.1). The allowable burr sizes vary for different applications. The plasticity of ductile materials promotes the formation of burrs. Typically deburring accounts for 30% of production costs. This number includes automated deburring and manual deburring. If the machining process can be altered to reduce the burr size then the deburring effort required will be reduced or even eliminated.

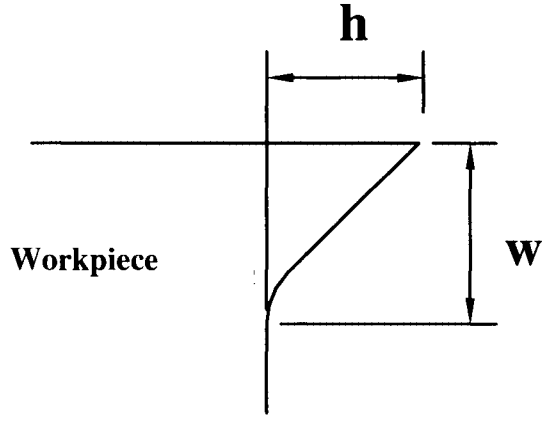

Figure 1.1: Idealized burr cross-section.

Before methods for burr size reduction are discussed, the common types of burrs must be defined. In general, there are 5 types of burrs: Poisson burrs, entrance burrs, rollover burrs, tear burrs and cut-off burrs. A Poisson burr results from the plastic deformation that occurs when a material is being compressed, as shown in Figure 1.2(a). An entrance burr may be formed when the tool first engages the material and plastically deforms them, see Figure 1.2(b). A rollover burr results from plastic deformation of material near the edge of the cutting path, where the work needed to deform the material plastically is less than the work needed to perform the desired cut, as illustrated in Figure 1.2(c). With this type of burr the cutting tool simply pushes a portion of material out of its path. A tear burr results from tearing of material instead of shearing it. A fractured burr results from material fracture before a cut is completed.

This thesis is concerned with burr formation in drilling. The largest burr is produced when the drill exits the hole and is termed an 'exit burr' (see Fig. 1.3). It is a combination of a rollover burr and a tear burr. The rollover burr is the dominant burr mechanism and will be discussed in detail in chapter 2.

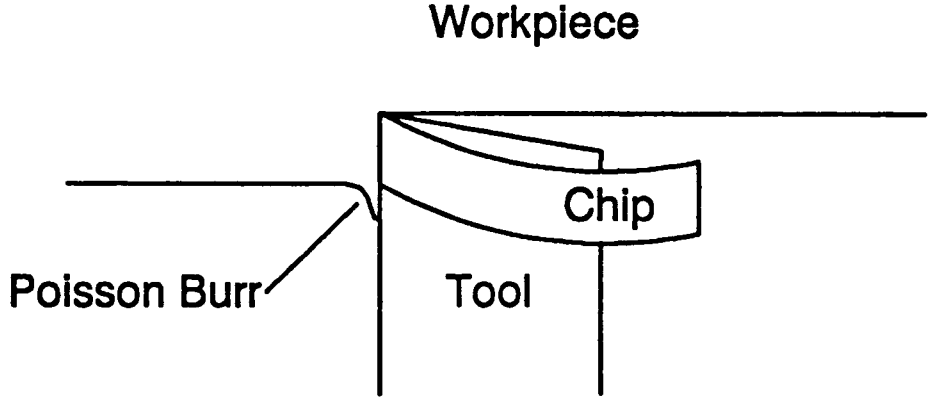

(a) Poisson Burr.

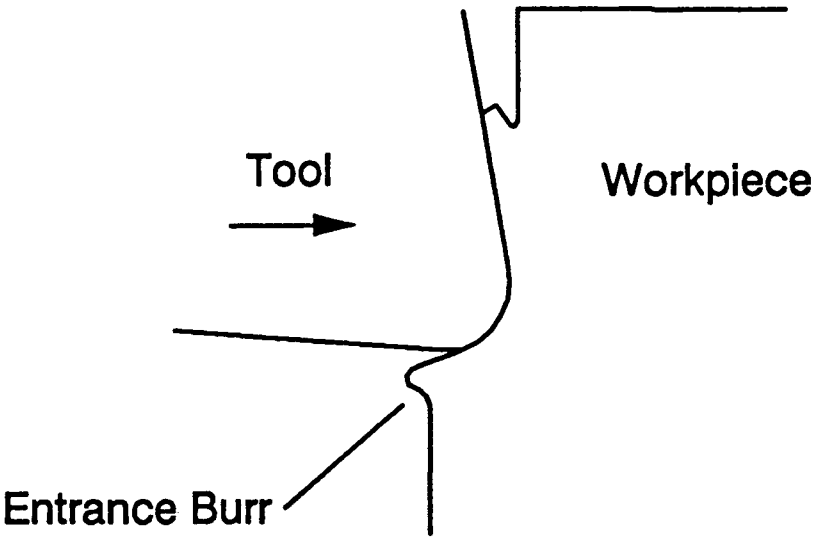

(b) Entrance Burr.

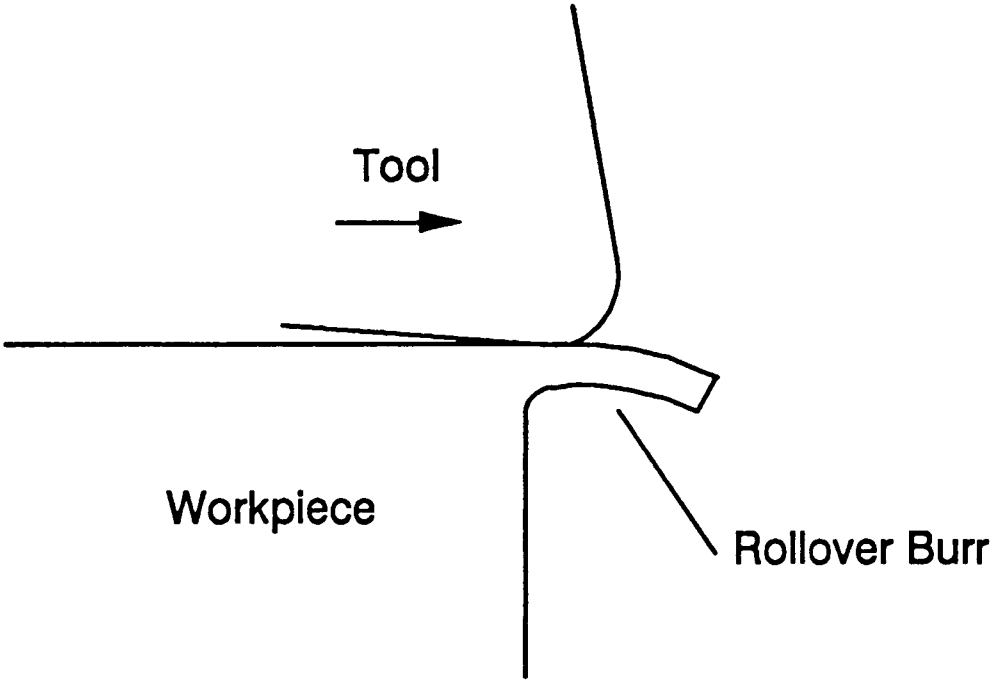

(c) Rollover Burr.

Figure 1.2: Different types of burr (taken from Bone [1]).

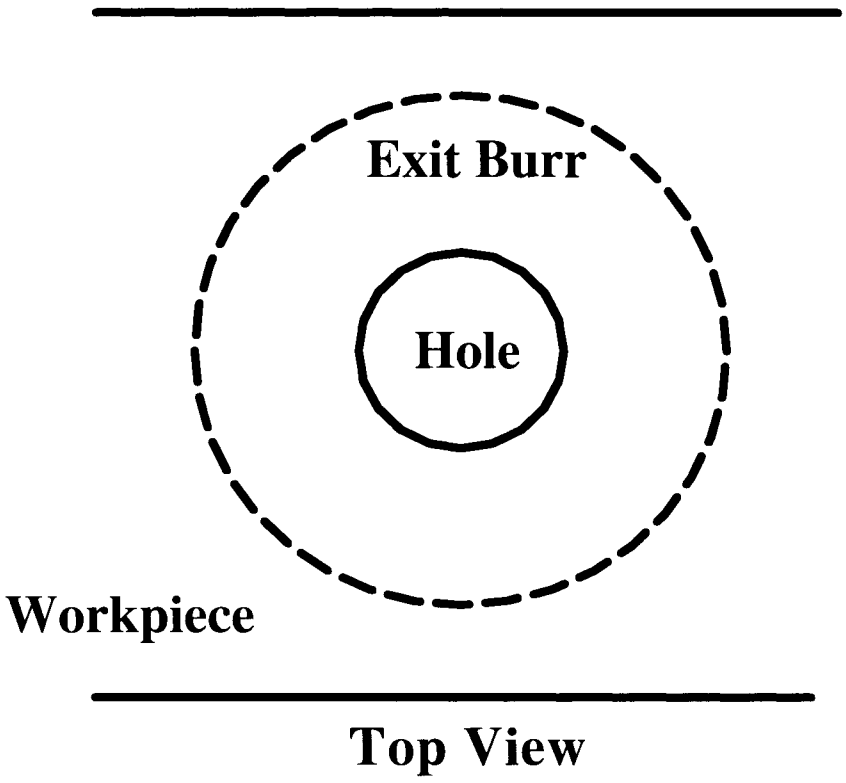

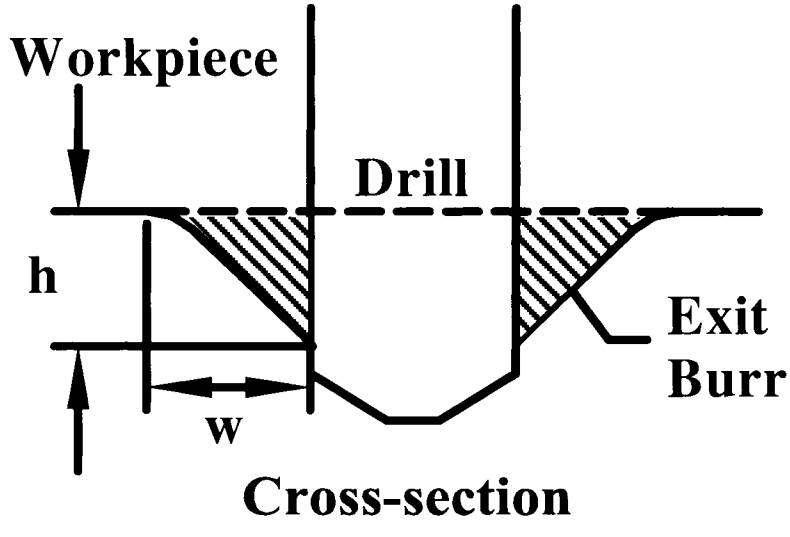

Figure 1.3: Exit burr produced by drilling.

There are different methods for burr reduction. Altering the cutting feed and spindle speed, drill geometry, using suitable coolant and even suitable coatings on the tool can all reduce burr size.

The influence of feed on burr size is not linear. At low feed range, chip thickness is small relative to the cutting edge radius. This results in a tool plowing action and increases stress level on the workpiece, thus increasing plastic deformation and burr size. On the other hand, thrust force is high at higher feed range. This results in larger burr size. Note that the definitions of low and high feed range depend on cutting different materials.

Based on previous literature, a spindle speed below 800rpm does not influence the burr size. However, a linear increase in burr size with spindle speed above 800rpm is observed. This increase is significant when drilling is performed at a high feed range.

In general, using a drill with high point angle and low helix angle can reduce burr size. It was found that helical point drill produces much smaller burrs than split point drill as well. Radial periphery drill also produces much smaller burrs than standard drill. However, this type of drill is not commonly available.

Using suitable coolant and tool coating can reduce the friction between the tool and the workpiece. This reduces the heat generated and the stress level on the workpiece, results in smaller burr size.

A recent and very promising technique is known as 'vibration drilling' or 'ultrasonic assisted drilling'. The principle of this technique is adding high frequency (above 20kHz) and low amplitude (7-10μm is commonly used) in the direction of drill

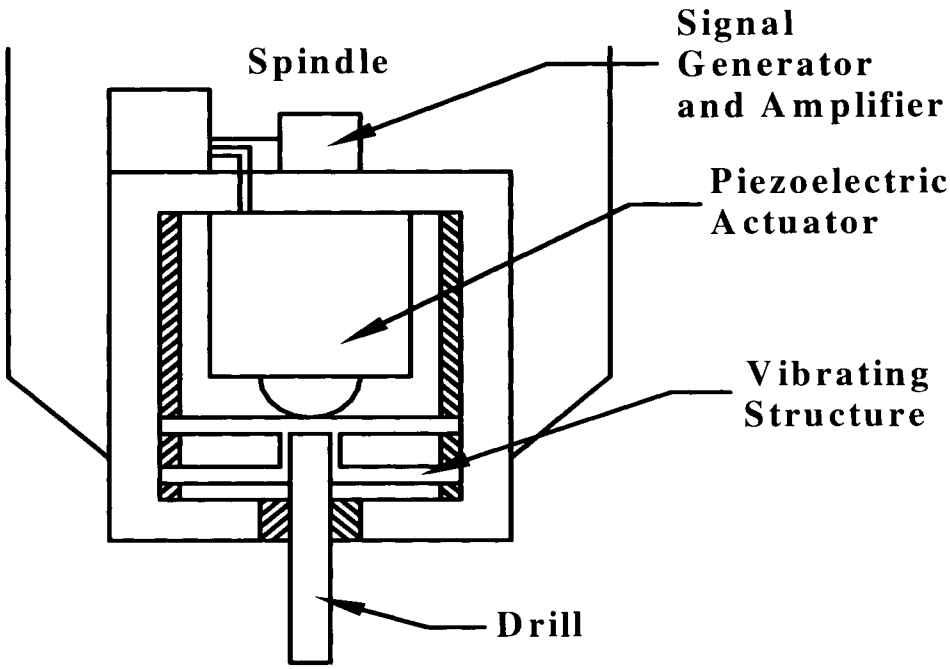

a) Typical machine with ultrasonic assistance on the tool.

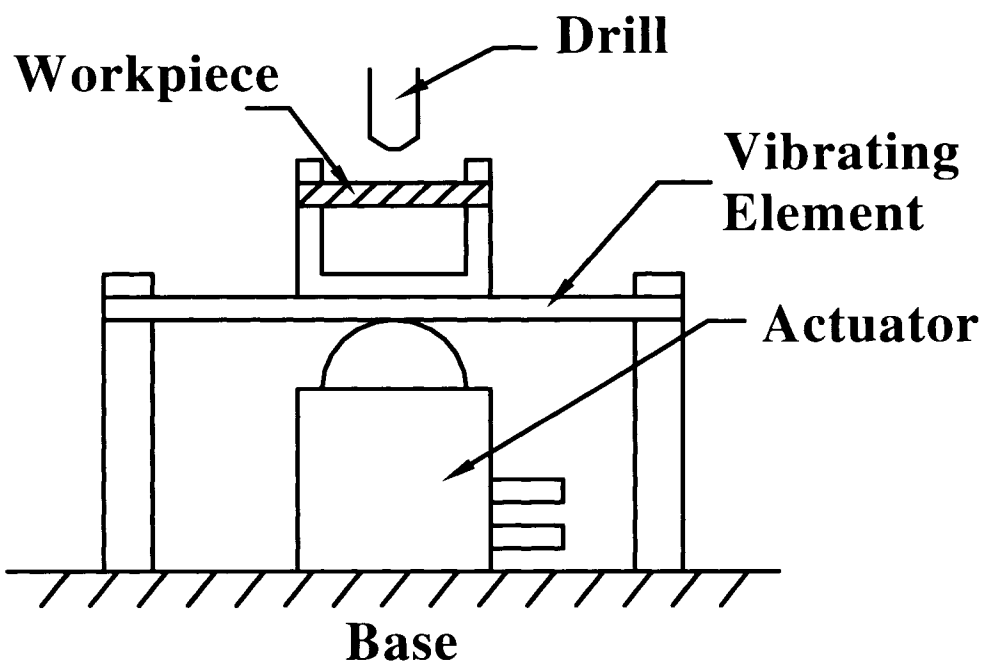

b) Typical machine with ultrasonic assistance on workpiece.

Figure 1.4: Typical ultrasonic assisted machine.

feed to the motion of the tool or the workpiece (see Fig. 1.4). Typically a piezoelectric actuator is used as the vibration source.

This thesis includes theoretical and experimental investigations of ultrasonic assisted drilling in machining aluminum based on an industrial milling machine equipped with a custom built ultrasonically oscillated workpiece holder. The workpieces were excited at 10, 15 and 20kHz to obtain the ultrasonic assistance. In chapter 2 the current state of research in the area is reviewed. In chapter 3 an orthogonal cutting model with ultrasonic assistance is presented, and a better vibration combination exists for thrust and burr minimization is concluded. In chapter 4, a simplified exit burr model in ultrasonic assisted drilling and the corresponding simulation results are presented. The workpiece holder and the drive circuit are designed in chapter 5. The designs are then manufactured and used in the experiments for ultrasonic assisted drilling. In chapter 6 the experimental results and theoretical explanation of the behavior of the workpiece is presented. In chapter 7, the conclusion of this thesis and suggested future work are presented.

CHAPTER 2

LITERATURE REVIEW

2.1 Introduction

In this chapter the current literature related to ultrasonic assisted drilling is reviewed. This has been broken down into 3 areas: drilling process modeling, analysis and modeling of burr formation, and ultrasonic assisted drilling.

2.2 Drilling Process Modeling

Models predicting forces produced during drilling on the workpiece are desirable. They can be used to help alter the drilling process in order to minimize thrust forces and burr size. They can also be used to predict burr size in order to help plan the deburring operation. Several researchers have studied and modeled the forces produced during drilling.

Drilling is often modeled as a combination of orthogonal cutting and indentation along the chisel edge, and oblique cutting along the cutting edge, usually known as the lip, as shown in Fig. 2.1.

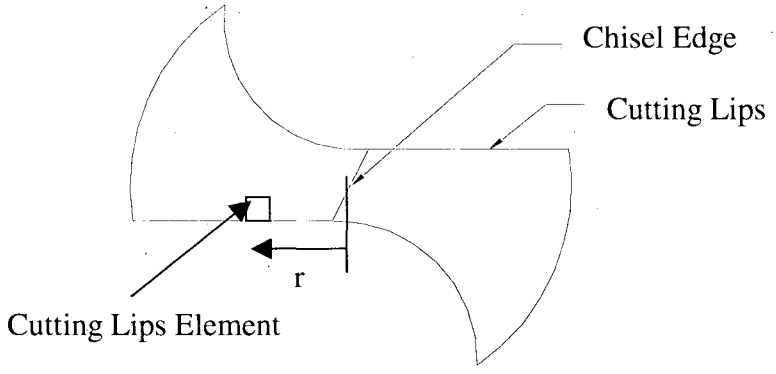

Figure 2.1: Basic geometry of drill.

In contrast to other cutting processes, drilling does not has a fixed set of parameters, such as rake angle. Hence, the cutting edges are usually broken down into elements or use differential techniques for detailed analysis, although approximation, such as using average rake angle, are sometimes acceptable. However, empirical equations, which are limited to a set of specific cutting conditions and drill geometries, are often used.

A recent work by Elhachimi and his fellows [2] developed a theoretical model to predict thrust and torque in high speed drilling using conventional twist drill. Similar to the previous works, the drill is broken down into 2 cutting region, the cutting lip and chisel edge.

Elhachimi et. al. broke down the cutting lips into elements. By determining the differential thrust dF_l and torque dC_l on each element, the total thrust and torque can be computed. Using the terminology used by Elhachimi et. al. [2], each element has a

length of *dl*, located at a radius *r* away from the drill axis (Fig. 2.1). Thrust and torque analysis will be done with an oblique cutting model.

The inclination angle *i* and rake angle γn at each element can be computed geometrically. The cutting geometry of each element on the cutting lip is shown in Fig. 2.2.

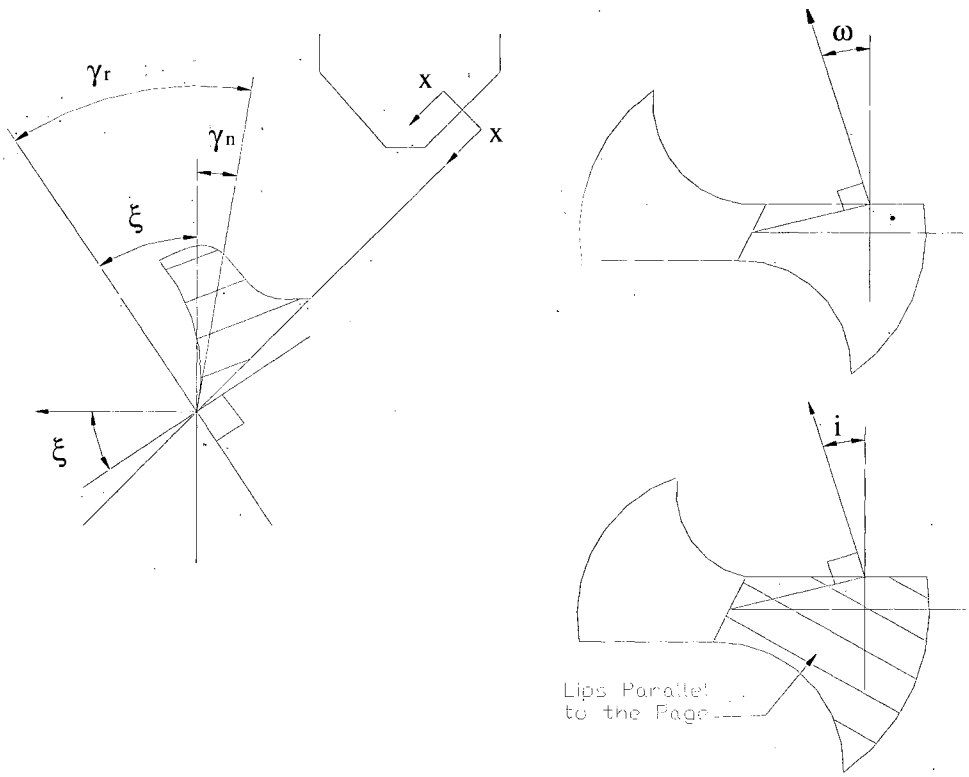

Figure 2.2: Cutting geometry on the cutting lip (after Elhachimi et. al. [2]).

The differential shear force of each element can then be computed:

$$dF_s = \frac{k_{AB} t_1 dl}{\sin \phi_n} \tag{2.1}$$

where t_1 is the depth of cut, k_{AB} is the specific cutting pressure, and ϕ_n is the shear angle at each element. The thrust force and torque produced by each element can then be computed.

Elhachimi et. al. [2] divided the chisel edge into 2 regions. The region closer to the drill axis is an indentation region, where practically no material is being cut but loaded in the feed direction. The outer region is a cutting region, which can be modeled by an orthogonal cutting model with a negative rake angle. Since in conventional drilling, the magnitude of thrust and torque contributed by the indentation zone is negligible, only the cutting region of the chisel edge has been modeled.

The cutting region is defined by the outer end of the chisel edge and r_a, where:

$$r_a = \frac{f \tan p \sin \psi}{2\pi} \tag{2.2}$$

where f is the feed, p is half of the point angle of the drill, and ψ is the web angle.

Since the dynamic rake angle varies with radius, the chisel edge is divided into differential elements. The dynamic rake angle γ_d at each element can again be computed geometrically, using the aid from Fig. 2.3.

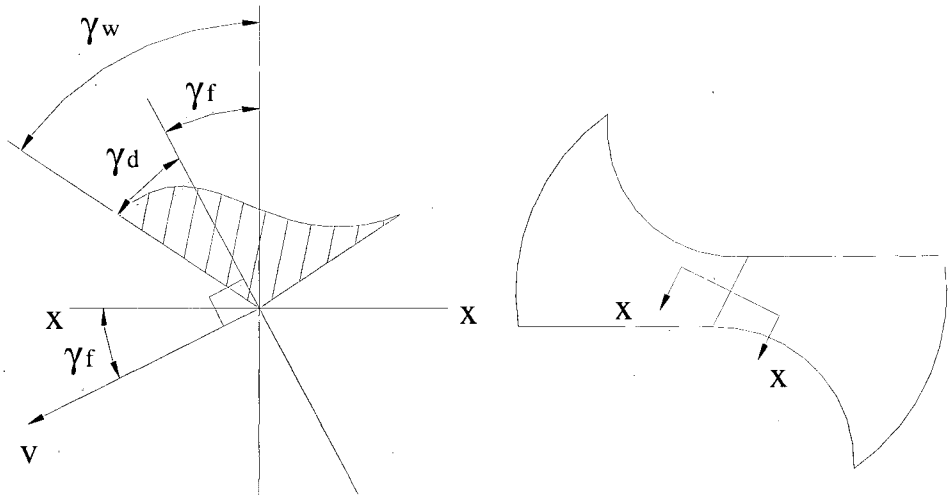

Figure 2.3: Cutting geometry on the chisel edge (after Elhachimi et. al. [2]).

The shear force element dF_s for each element is:

$$dF_s = \frac{k_{AB} t_1}{\sin \phi_n} dr \tag{2.3}$$

This differential shear force can then be used to compute the thrust force and torque produced by each element.

Based on the theoretical model of drilling presented by Elhachimi et. al. [2], Zhang et al. [3] had developed a theoretical model for vibration assisted drilling. The variation of cutting angles and uncut chip thickness with time complicates the analysis of vibration drilling.

The total displacement and velocity of the tool in vibration drilling (after Zhang et al. [3]) is:

$$x(t) = A\sin(2\pi f_u t) + fnt \tag{2.4}$$

$$v(t) = 2\pi Ft\cos(2\pi f_u t) + fn \tag{2.5}$$

where A is the vibration amplitude, f_u is the vibration frequency, t represents the time, f is the feed rate and n is the spindle speed in rpm. Expressing equations (2.4) in terms of the rotation angle of the drill θ gives:

$$x(t) = A\sin\left(\frac{F}{n}\theta\right) + \frac{f}{2\pi}\theta \tag{2.6}$$

where $\theta = 2\pi nt$. Equation (2.6) expresses the axial displacement equation for one of the cutting lip, say, lip A. The other cutting lip, lip B, will be 180° out of phase. The equations set for axial displacement of the two lips can then be expressed as:

$$Z_A(\theta) = A\sin\left(\frac{F}{n}\theta\right) + \frac{f}{2\pi}\theta \tag{2.7}$$

$$Z_B(\theta) = A\sin\left(\frac{F}{n}\theta + \pi\right) + \frac{f}{2\pi}(\theta + \pi) \tag{2.8}$$

In order to find the actual dynamic uncut chip thickness, Zhang et al. [3] found an equation expressing the machined surface and compared it to the instantaneous location of the tool.

Zhang et al. [3] expressed the machined surface after the first m cuts as:

$$Z_k(\theta) = A\sin\left[\frac{F(\theta - k\pi)}{n}\right] + \frac{f(\theta - k\pi)}{2\pi} \tag{2.9}$$

where $k = 1, 2, \ldots, m$, where m is the minimum value that satisfies the expression:

$$\max\{Z_k(\theta)\} > Z_{m+1}(\theta) \tag{2.10}$$

Hence, the 'counter' m stops as soon as the drill withdraws from the material, and no cuts can be preformed.

The axial uncut chip thickness can now be expressed as (after Zhang et al. [3]):

$$h_f = Z(\theta) - \max\{Z_k(\theta)\} \tag{2.11}$$

If h_f is negative, that means the tool is not in contact with material and no cutting can occur. In that case, $h_f = 0$.

The dynamic uncut chip thickness can then be expressed again using the geometrical properties of the drill. It is important to note that these geometrical properties vary with time as well in vibration assisted drilling.

Although the force model for conventional drilling has been developed, more work is needed to understand the force produced in vibration drilling. Zhang et al.'s [3] work has shown such models are possible, but involve complicated computation. The author's [3] model also ignores the dynamic responses of the workpiece, which might contribute to the total force analysis.

2.3 Analysis and Modeling of Burr Formation

2.3.1 Burr Formation Theories

Models for the prediction of burr formation are desirable. They can be used to determine the burr size to help planning the deburring process. Moreover, by understanding the burr formation mechanism, they can help alter the cutting process correctly to minimize the burr formation.

Dornfeld had investigated the process of roll-over burr using plasticine as working material. Roll-over burr results from material being deformed rather then being cut. When the work required to cut the material equals the work required to deform it,

the transition period occurs. The author [4] had divided the burr forming process into 3 stages – initiation, development and final burr formation. As the tool approaches the end of the workpiece, the aforementioned transition period occurs, initializing burr formation.

According to Dornfeld's terminology, a negative shear plane, which connects the cutting tool edge to a plastic hinge on the exit surface of the workpiece, is developed at the transition period. The negative shear angle is then defined as the angle between the cutting surface and negative shear plane, see Fig 2.4.

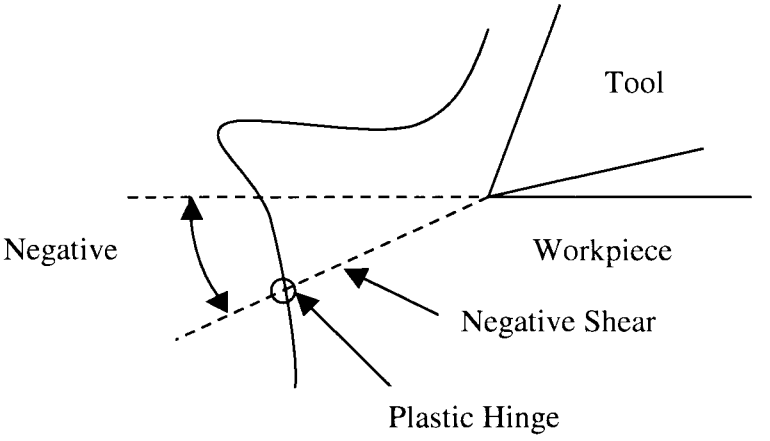

Figure 2.4: Negative shear angle and negative shear plane.

As the tool advances, burrs develop as the negative shear plane rotates about the fixed plastic hinge. The material above the negative shear plane rotates rigidly, and both the strain along the negative shear plane and the magnitude of negative shear angle increases. The burr finally forms as the tool exits the cutting surface. Fracture may form along the negative shear plane because of the increase in strain, and burr size may be reduced. However, if fracture occurs during the burr formation process, it results in a fractured exit surface on the workpiece (Fig. 2.5).

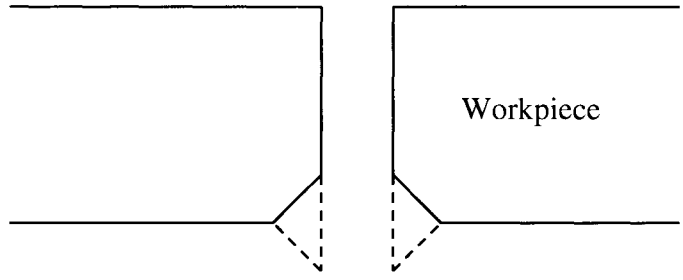

Figure 2.5: Burr fractured.

Dornfeld et al. [5] had further defined 4 types of burrs from drilling, which are shown in Fig.2.6.

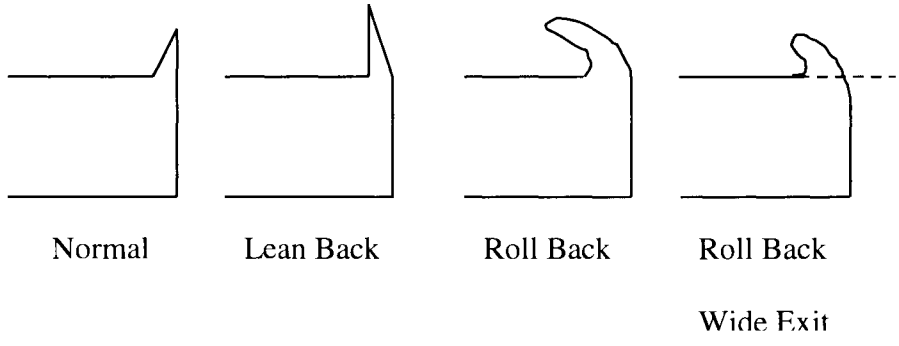

Figure 2.6: Different types of burr.

As the drill approaches the exit surface, materials under the chisel edge begin to deform plastically (Fig.2.7). Thickness t depends on the thrust force of the drill in classic drilling operation, and in general, depends on the stress concentration on the workpiece. As the drill advances, the deformation zone expands to the edge of the drill, and may cause the separation of deformed materials from the hole perimeter, forming a drill cap. The material around the hole perimeter deforms and a burr form. Since no cutting occurs, i.e. no chip formation, during burr formation, the heat generated cannot be dissipated, and a localized temperature increase occurs at the inner surface of the burr.

This results in thermal expansion, causing the lean back and roll back burrs to form (type 2 and 3). With the addition of suitable coolant, these lean and roll back phenomenon should be reduced. Type 4 burr is formed when there is fracture along the negative shear plane during burr formation, and part of the materials on the exit surface is removed.

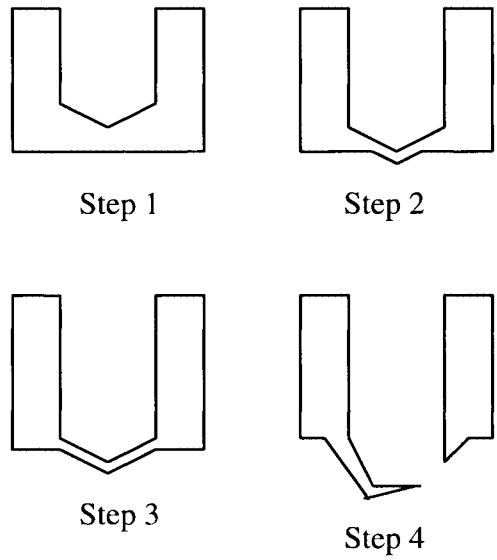

Figure 2.7: Burr formation in drilling.

2.3.2 Finite Element Modeling of the Burr Formation Process

There are few models of burr formation in drilling, although burr formation mechanisms and models are well developed for orthogonal cutting operations such as turning. Dornfeld et. al. [6-9] completed a series of finite element models with analysis. The simulation results for burr formation in drilling showed consistency with the theories developed for the burr formation mechanism in orthogonal cutting. Fig.2.8 (taken from Dornfeld [6]) shows the development of the negative shear zone.

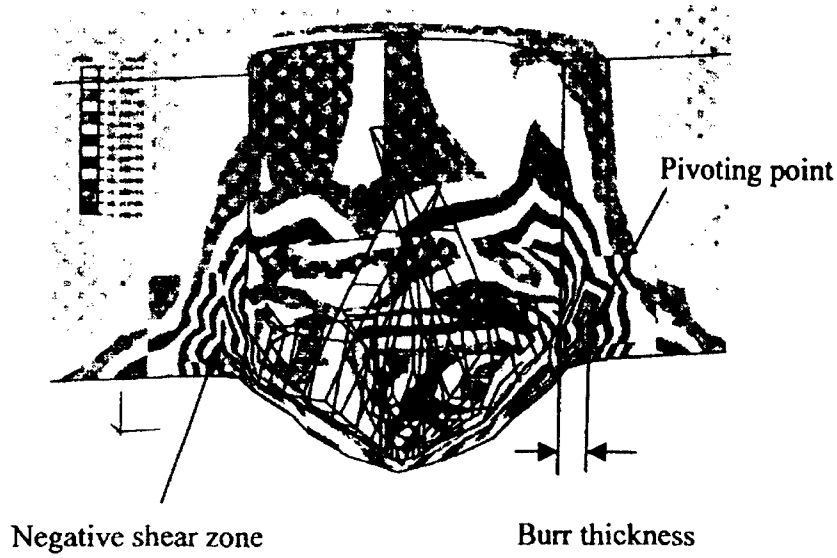

Figure 2.8: Finite element model of burr formation (taken from Dornfeld [6]).

2.3.2 Theoretical Model of Burr Formation

A simple theoretical model was developed later by Lauderbaugh and Mauch [10]. The model involves breaking down a drilling process in 2 cases. Case 1 modeled the process until breakthrough of material occurs, and case 2 modeled the rest of the process.

i) Case 1

The plate under the tool can be modeled by the following plate equation:

$$D\frac{d}{dr}\left[\frac{d\phi}{dr}+\frac{\phi}{r}\right]+\frac{dD}{dr}\left[\frac{d\phi}{dr}+v\frac{\phi}{r}\right]=-Q \tag{2.12}$$

where $D = EH^3/12(1-v^2)$ (2.13)

In equation (2.12) and (2.13), Q is the total shear force, ν is Poisson's ratio, E the Young's Modulus, ϕ is the angle of the neutral plane and H is the height of the plate.

Rearranging equation (12) and (13) yields:

$$KH^3\frac{d^2\phi}{dr^2}+\left[K\frac{H^3}{r}+3KH^2F\right]\frac{d\phi}{dr}+\left[3\nu K\frac{H^2}{r}F-K\frac{H^2}{r^2}\right]\phi=-Q \tag{2.14}$$

$$K=\frac{E}{12\left(1-\nu^2\right)} \tag{2.15}$$

$$F=\left[U\left(r-R_0\right)\frac{h-h_0}{R}\right] \tag{2.16}$$

Solving equation (2.14) with 2nd order Euler's method, the radial and tangential stresses can be expressed by:

$$\sigma_r=\frac{6M_r}{a^2} \tag{2.15}$$

$$\sigma_t=\frac{6M_t}{a^2} \tag{2.16}$$

where $M_r=D\left[\frac{d\phi}{dr}+\nu\frac{\phi}{r}\right]$ and $M_t=D\left[\frac{\phi}{r}+\nu\frac{d\phi}{dr}\right]$, a is the distance from the neutral plane to the stress element. These 2 stress components are used to compute von Mises stress along the bottom of the plate. If the von Mises stress exceeds the ultimate strength of the material, the plate fails and breakthrough occurs. If the von Mises stress does not exceed the ultimate strength, no failure occurs and the deflection of material can be computed, and the tool advances and a new axial depth of cut equals the axial movement of the tool minus the deflection of the plate. New stress components can be recalculated and this process is repeated until breakthrough occurs, where case 2 start.

ii) Case 2

Case 2 occurs as soon as breakthrough occurs. In this case, $H = cr$ where c is the slope of the plate, and r is the radius of an arbitrary position. Substituting the value of H into equation (2.13), and the transformation $r = e^z$, equation (2.12) can be expressed as:

$$\frac{d^2\phi}{dz^2} + 3\frac{d\phi}{dz} + (3\nu - 1)r\phi = \frac{-16q\left(1 - R_0^2 e^{-2z}\right)}{3Ec^3} \tag{2.16}$$

and the solution of equation (2.16) is:

$$\phi = A + \frac{B}{r^3} - \frac{16q}{3Ec^3}\left[\frac{1}{3}\ln r + \frac{R_0^2}{2r^2}\right] \tag{2.17}$$

$$A = \frac{16q}{3Ec^3}\left[\frac{1}{3}\ln R + \frac{R_0^2}{2R^2}\right] - \frac{B}{R^3} \tag{2.18}$$

$$B = \frac{16}{3Ec^3} R^3 R_0^2 \left[\frac{1}{3}\ln\frac{R_0}{R} - 1.5 - \frac{R_0^2}{2R^2}\right]\left[\frac{1}{-8R^3 - R_0^2}\right] \tag{2.19}$$

The radial and tangential stresses can be computed by equations (2.15) and (2.16), and von Mises stress can then be computed at the periphery of the hole. If the von Mises stress exceeds the workpiece's ultimate strength, the material at the periphery fails and burrs form. Their length can be computed by:

$$l_{burr} = R - R_f \tag{2.20}$$

Likewise, if failure does not occur, the tool advances and the new depth of cuts equals the axial displacement of the tool minus the deflection of the plate, which can be computed by:

$$w = \int_{R_0}^{R} \phi dr \tag{2.21}$$

and the analysis repeats until failure at point B occurs. Zhang et al. concluded, both theoretically and experimentally, that there exists an optimal vibration amplitude and frequency such that the thrust and torque are minimized. This conclusion contradicted the usual misconception that the higher frequency and amplitude, the better the result, as suggested by Takeyama and Kato [11].

Clearly more work is needed to accurately predict the burr size theoretically. With an accurate model, minimizing burr size might be possible.

2.4 Ultrasonic Assisted Drilling

Ultrasonic assistance was found to be effective in reducing burrs from drilling. Takeyama and Kato [11] had experimentally shown the improvement in drilling aluminum. However, the mechanism cannot be simply explained by the theories from conventional ultrasonic machining.

When the drill advances and half of the thickness t becomes equal to or smaller than the amplitude of the induced ultrasonic vibration, the primary cutting motion is converted from rotational drilling action to the ultrasonic impact action. These impact actions generate stress concentration on the primary cutting path, and the material is successfully cut with less thrust force. This postpones plastic deformation along the negative shear plane, hence postponing initiation of burr formation. As a result, burr formation can be reduced significantly.

In addition, the oscillatory motion provides a slicing path at the tool edge, and material at the hole perimeter can be sliced away. Hence, less material can be plastically deformed to form burrs, thus reducing burr size.

Larger amplitude of ultrasonic vibration will promote the conversion of primary cutting motion, resulting in more effective prevention of burr formation. However, larger amplitude motion with same frequency leads to higher loads on the tool, which increases tool wear and reduces tool life. Stein and Dornfeld [8] have found that drill wear will increase the burr size. Hence, the amplitude should be chosen carefully.

Although Takeyama and Kato [11] have shown this method can drastically reduce burr size, the equipment that is required is not economically viable. Thus, more work is needed before the mechanism of ultrasonic assisted drilling can be understood, such that the vibration condition can be varied.

2.5 Conclusion

There are many attempts in deburring and reducing burr size in drilling recorded in the literature, however there are few accounts for ultrasonic assisted drilling. Models predicting thrust and torque in conventional and vibration drilling can also be found, although many of them requires empirical relations, which limits the models to a particular range of conditions only, and required experimental investigations to find the values of some parameters.

Models predicting burr size from drilling are rarely found, although extensive research has been done on burr modeling in orthogonal cutting such as turning. This

thesis presents a simplified model in predicting thrust in ultrasonic assisted drilling, and the corresponding exit burr model.

CHAPTER 3

FINITE ELEMENT MODELING OF ULTRASONIC ASSISTED ORTHOGONAL CUTTING

3.1 Introduction

In this chapter a simple orthogonal cutting process is modeled and simulated using the finite element method. Ultrasonic vibration was added to the simulation to allow its effects to be studied.

3.2 Cutting Conditions

Although the actual drilling operation is a complicated oblique and orthogonal cutting process it is expected that simulating simple orthogonal cutting will provide some insight into the effects of ultrasonic vibration.

The model consists of a cutting tool and a workpiece. The tool geometry and cutting conditions can be summarized in table 3.1.

Flank Angle	Rake Angle	Depth of Cut	Feed Rate
7°	10°	0.05mm	30mm/s

Table 3.1: Tool geometry and cutting conditions.

Fig. 3.1 shows the tool and workpiece configurations. The displacement, stress and strain on the edge of element 16 are monitored.

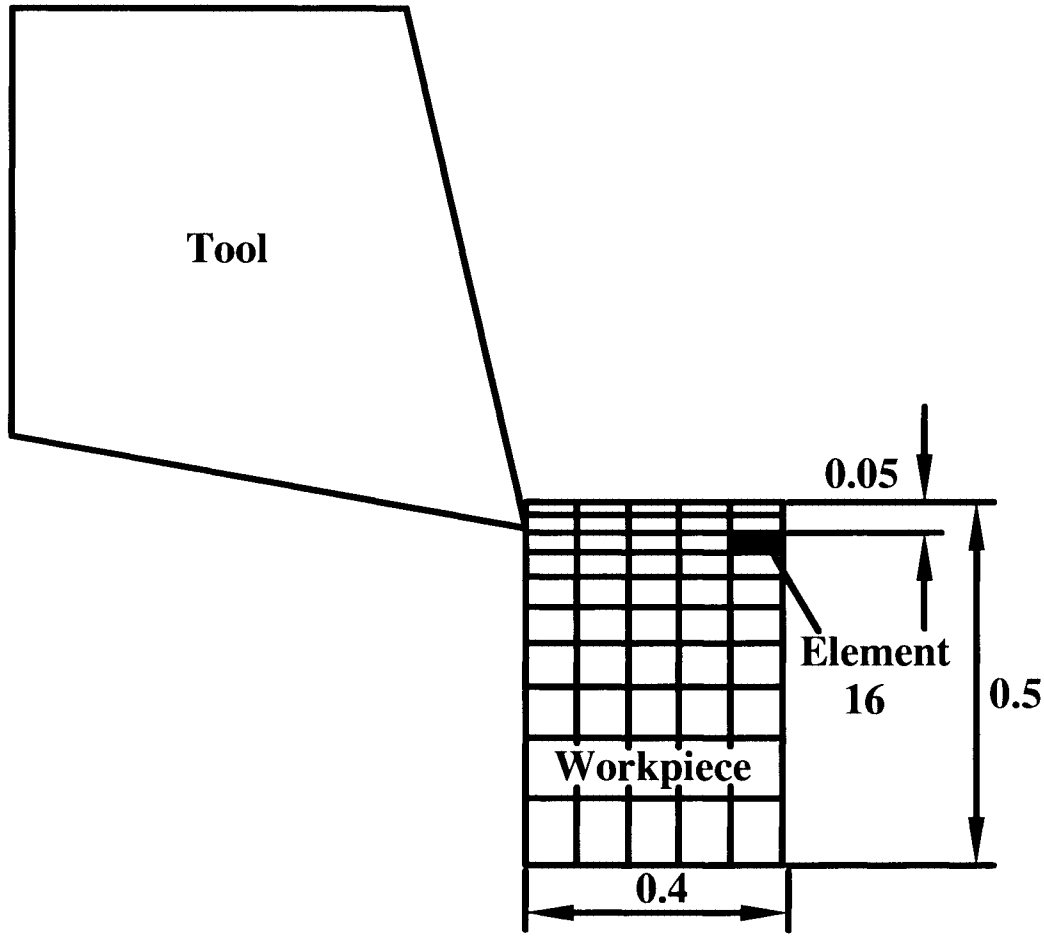

a) Side view of tool and workpiece configuration.

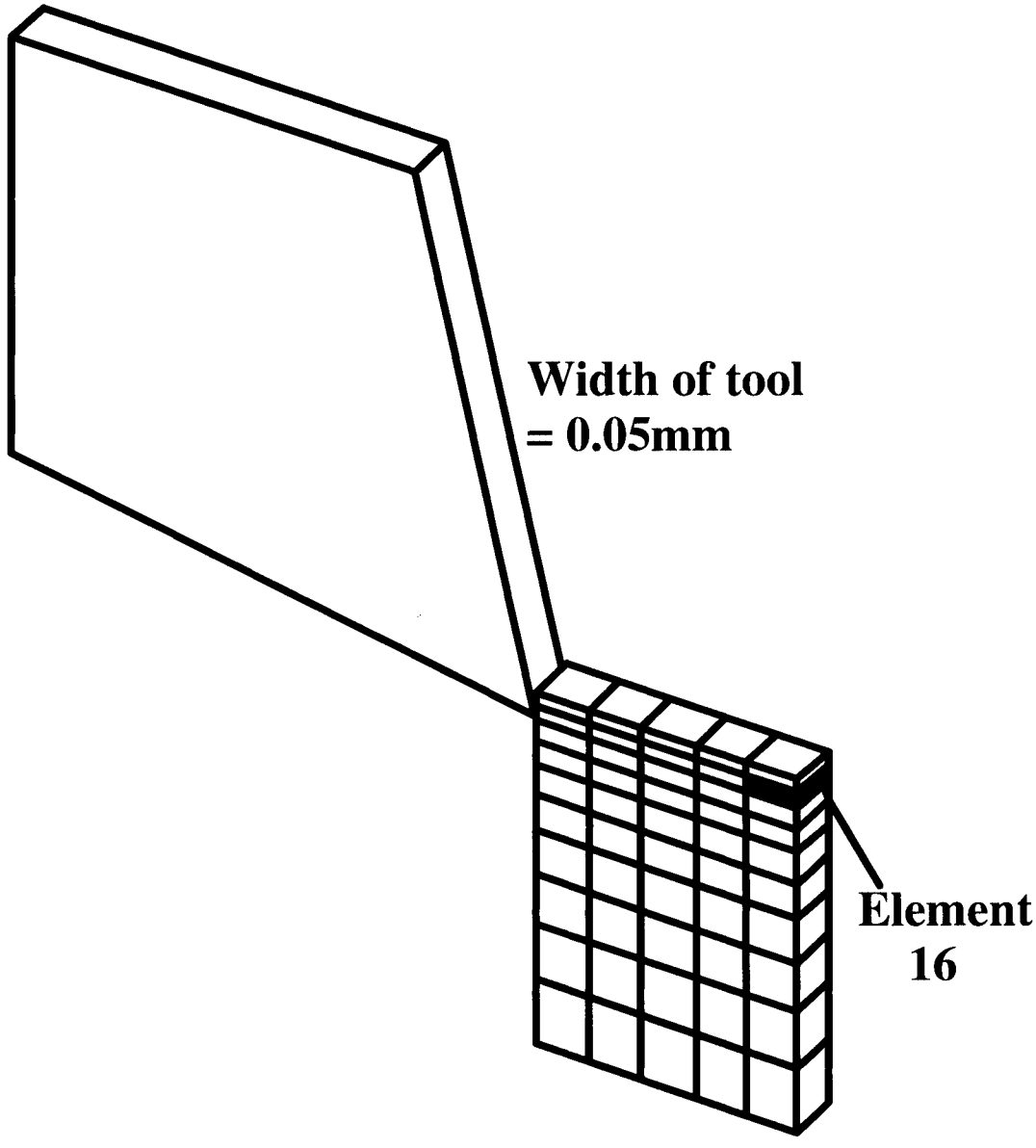

b) Isentropic view of tool and workpiece configuration.

Figure 3.1: Tool and workpiece configuration.

3.3 Boundary Condition

Two sets of simulations will be preformed. The first set simulates the conventional cutting process, and the second set simulates cutting with ultrasonic assistance. In order to solve for the difficulty of two sources of motion in ultrasonic cutting (due to the feed and ultrasonic vibration) in the second set, all eight nodes describing the cutter are prescribed with a harmonic oscillation. The base elements of the workpiece are prescribed with a constant velocity moving towards the cutter. The combined motion models for cutting with ultrasonic assistance. For consistency, the conventional cutting motion for the first set is also modeled by prescribing the base elements of the workpiece with the same velocity moving towards the cutter. The cutter is held stationary. This contradicts most cutting process models, where the cutter moves towards the workpiece. With the presence of body forces, this approximation will not be valid because the motion of workpiece will induce internal forces. Hence, body forces are neglected in the model. This is a reasonable assumption because in most cutting processes, body forces are either internally conservative (body forces cancel each other, such as turning process) or equal 0.

All free nodes are restricted to be fixed along the z-axis to remove the effect of round off and approximation errors. This assumption is acceptable because in metal cutting no translation along this axis exists. However, due to these errors, the simulated workpiece materials may deform along z-axis. Once deformation along this axis occurs, the workpiece is imbalanced, will deform further, and the simulation will return inaccurate results.

3.4 Meshing

The mesh for the workpiece was chosen to be coarse for fast solution convergence. Solid 3D elements with 8 nodes were used. Biases were set in order to make the mesh finer closer to the cutter. This produces a more accurate solution. The rectangular element and coarse meshing will reduce the accuracy of the calculation. However, since only a comparison between two cutting operation is being made with the same mesh, this faster (but less accurate) approach was considered acceptable.

3.5 Explicit Method

The software 'h3dmap' [12] will be used to solve the finite element computation using the explicit method. The explicit method is well suited to non-linear systems with transient loading. Hence it is appropriate to solve the proposed problem, where loading is coupled with oscillation and forward cutting motion.

3.6 Tied Nodes

The workpiece model consists of upper and lower parts, which are connected together using tied nodes. As the tool approaches, shear forces are generated and when they reach a threshold, the tie breaks, and the upper part of workpiece forms the chip. Fig.3.2 shows the orientation of the tied nodes. The constraint, or failure model, of breaking the tie is held constant for the two sets of simulations, so that a valid comparison is possible.

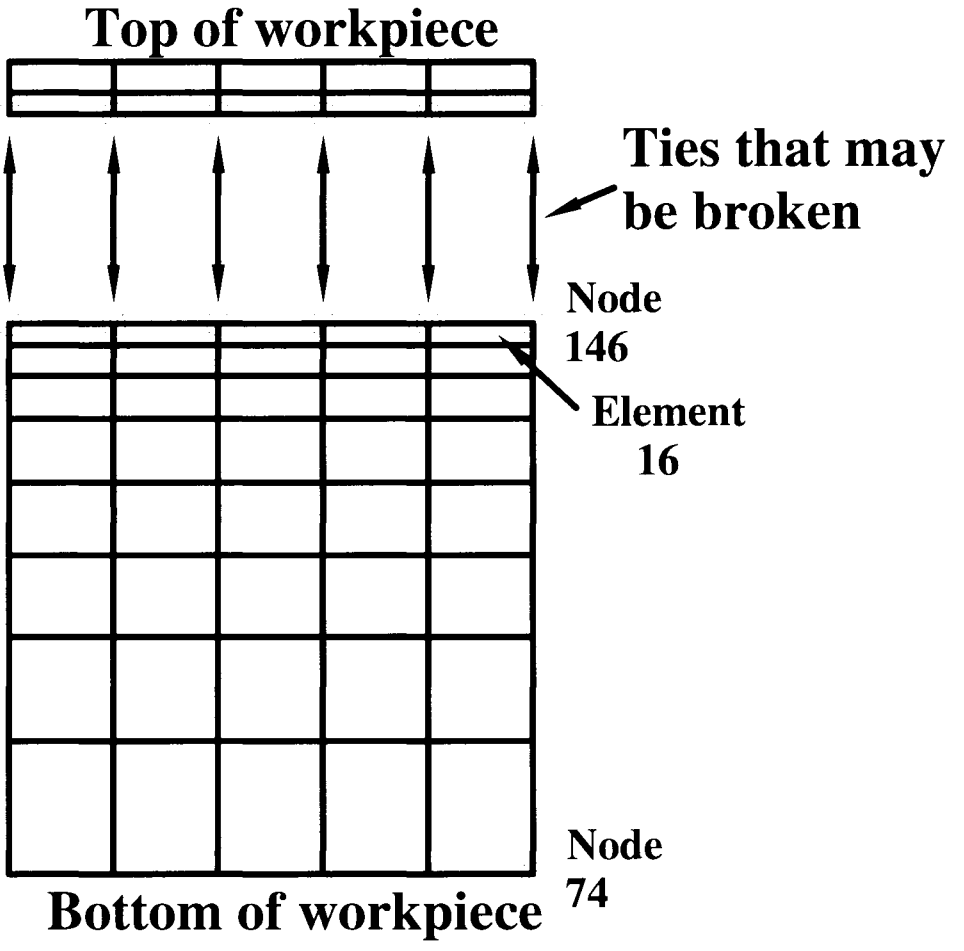

Figure 3.2: Tied nodes on workpiece.

3.7 Contact Surfaces

Contact surfaces on the workpiece are specified as slave surfaces, whereas those on the cutting tool are specified as master surfaces. As the tool approaches, the slave elements penetrate the master surface, inducing a contact force between them. These

contact forces contribute to the shear forces, which break the ties eventually. The contact forces are modeled as a spring force, and are computed as follow:

$$F_S = k_C \delta \hat{n} \tag{3.1}$$

where δ is the penetration distance of the slave node relative to the master surface, and $\hat{n}$ is the normal vector perpendicular to the master surface. The penalty stiffness, k_C, is computed by:

$$k_C = \beta \frac{K_m A_m}{t_m} \tag{3.2}$$

where A_m is the area of the master segment, K_m is the bulk modulus of the solid element (workpiece), and t_m is the thickness of the master segment, β is a scale factor. For master and slave elements whose size is roughly equal, β = 0.1. In the simulation, since the size of master element is roughly 10 times larger than the slave elements, β has been chosen to be 0.001. Fig. 3.3 shows the contact surfaces for the tool and workpiece.

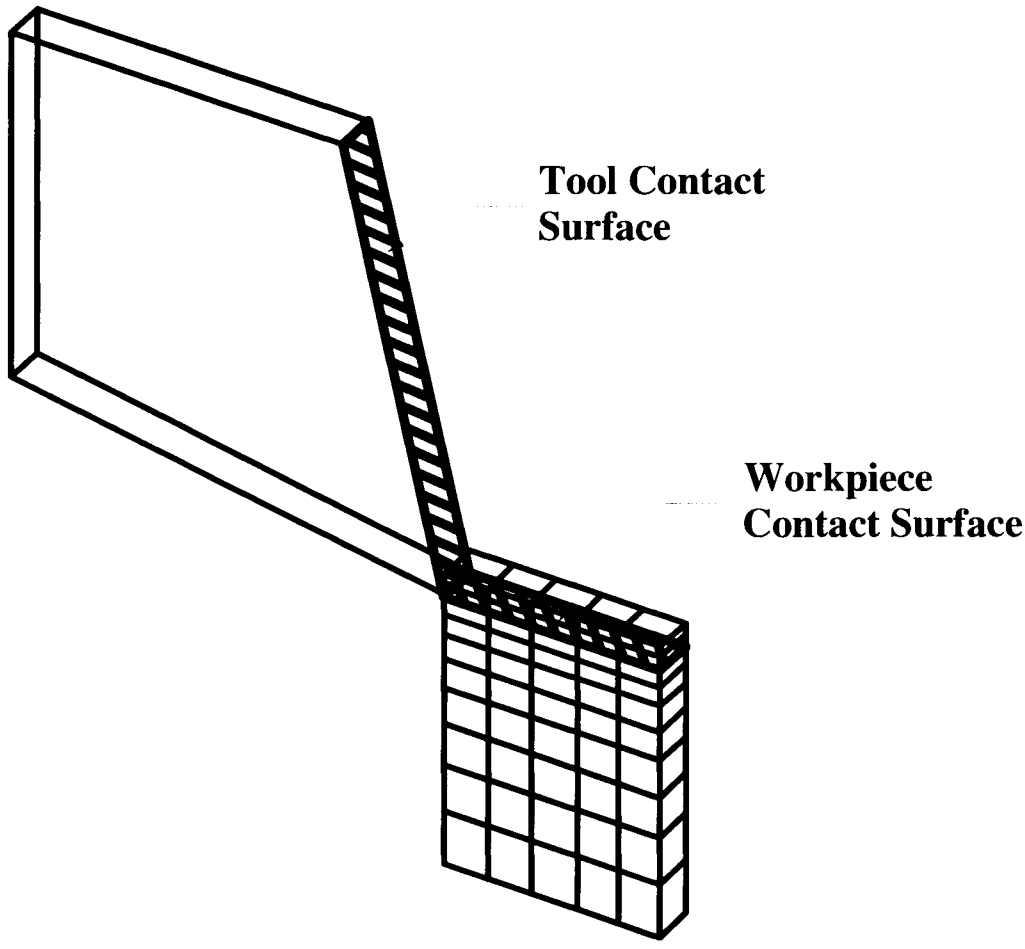

Figure 3.3: Contact surfaces.

3.8 Simulation Results

3.8.1 Overview

Fig.3.4 shows the workpiece response under the conventional cutting process with duration of 0.020s. Note that the chip has just been detached from the workpiece. The rolling action of the chip is expected, but the surface finish is poor. A burr exists at the exit edge of the workpiece.

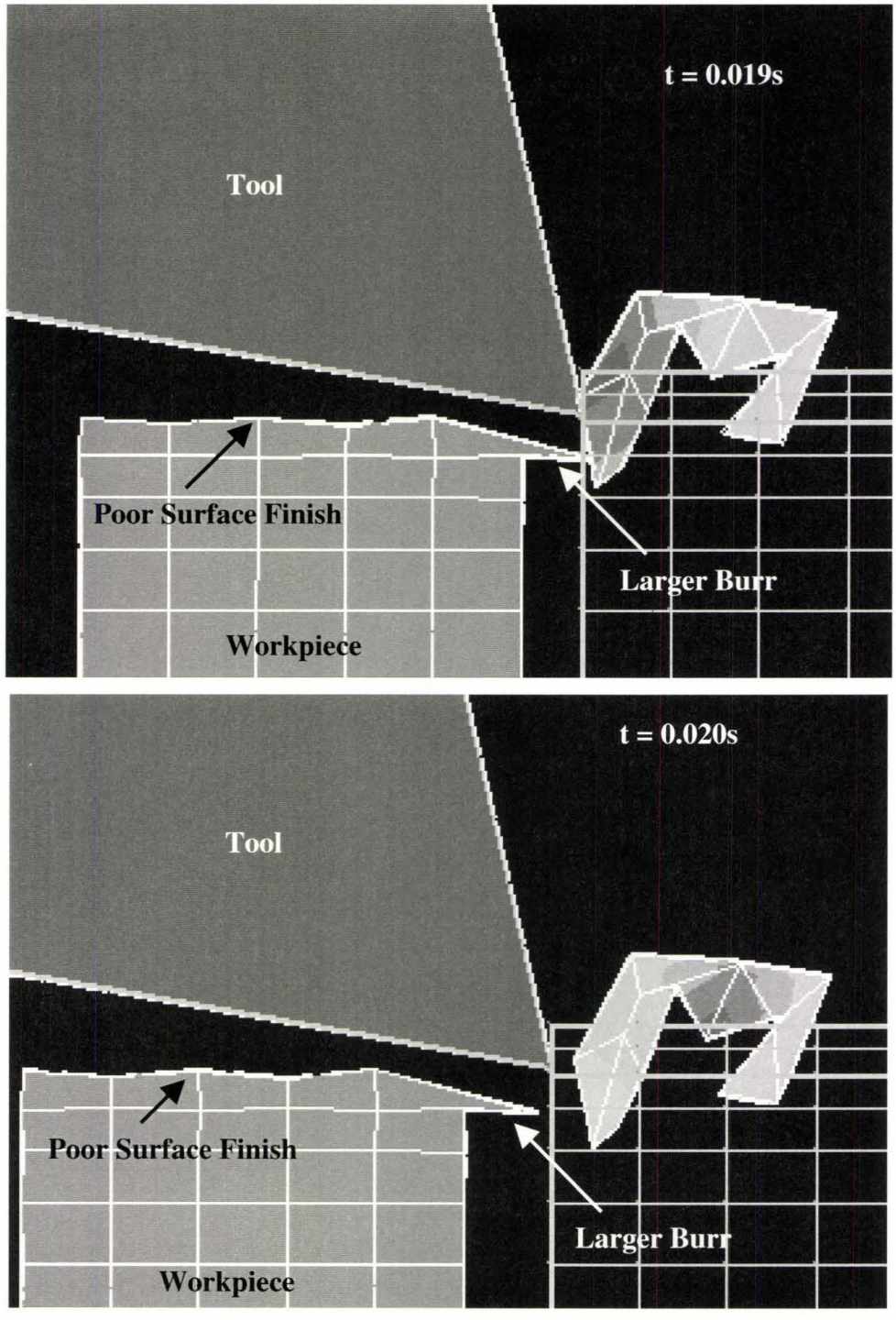

Figure 3.4: Workpiece response without ultrasonic assistance.

Fig.3.5 shows the workpiece response under the ultrasonic assisted cutting process. The surface finish has improved, and the burr size has been reduced. The ultrasonic vibration amplitude was chosen to be 10μm, and the vibration frequency is 10000Hz. These values were chosen to demonstrate the effect of ultrasonic assistance clearly. In the latter simulations, different values of amplitude and frequency are used to determine the effect of these parameters on the performance of ultrasonic assisted machining.

It should be note that the shear plane will be rotated to form a negative shear plane when the tool approaches the exit surface of the workpiece [6-9], which was not observed from the simulation. The predicted burr sizes are therefore an approximation only, but the comparison between ultrasonic assisted and conventional cutting is still valid.

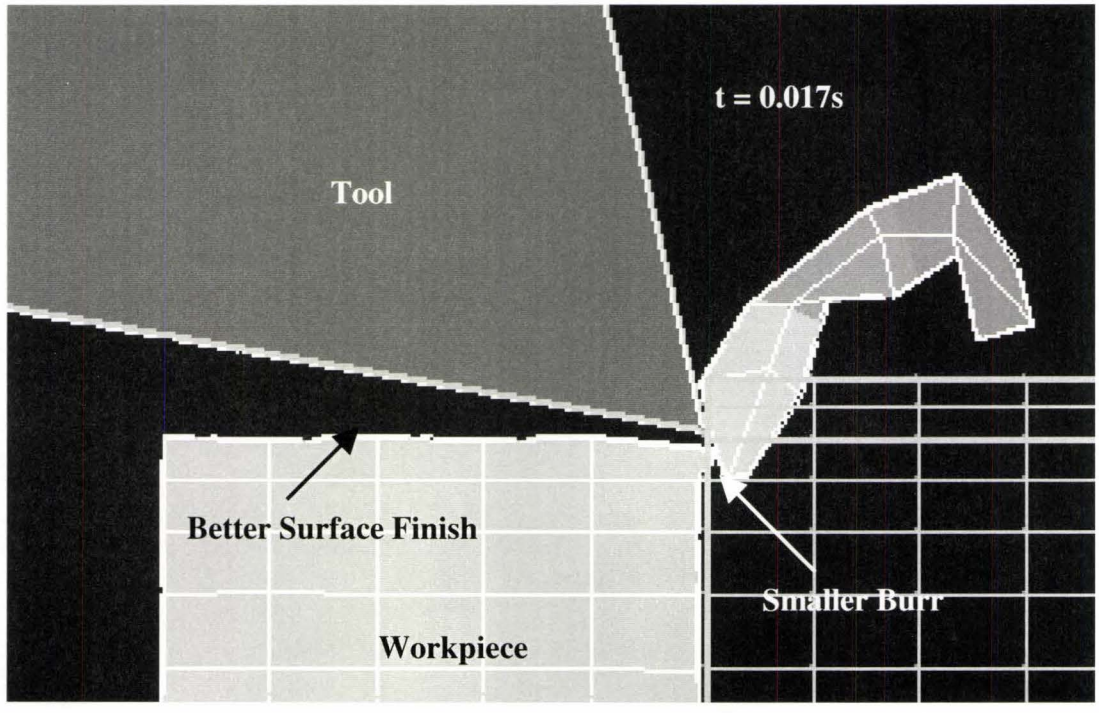

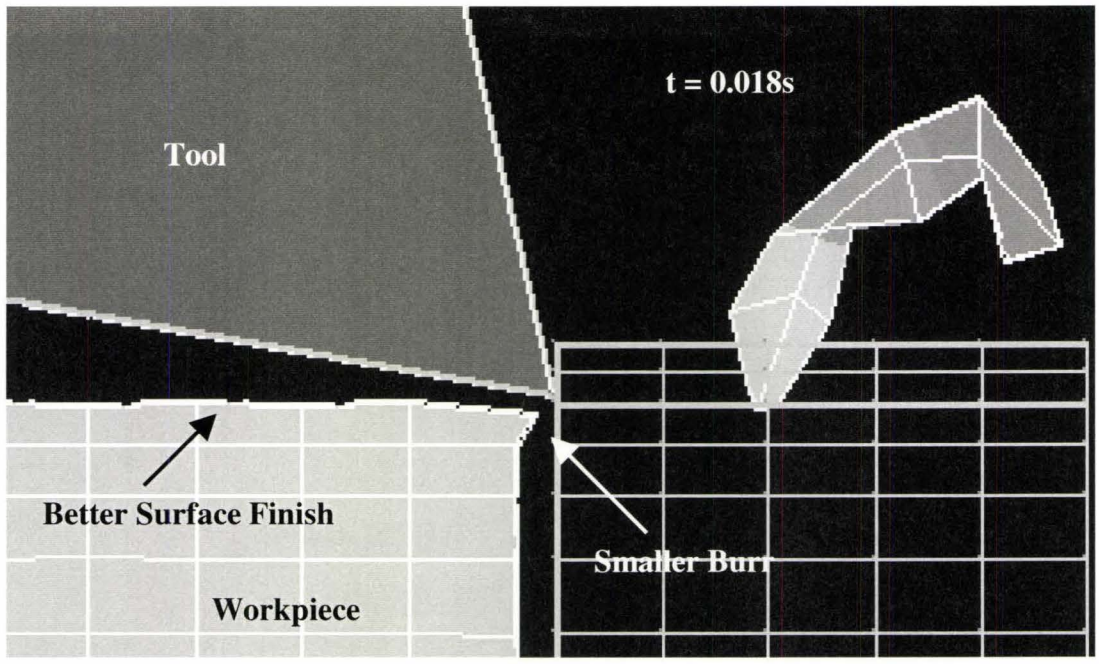

Figure 3.5: Workpiece Response with Ultrasonic Assistance.

3.8.2 Effect of Ultrasonic Vibration on the Mechanics of the Cutting Process

Fig. 3.6 shows the difference in x-direction displacement between node 146 and node 74. This value represents the instantaneous burr height. As the tool approaches the end edge, the burr height of workpiece under traditional cutting process is significantly greater than that of ultrasonic assisted cutting. The oscillation in ultrasonic assisted cutting allows the elastic deformation of the workpiece to be released. As the tool oscillates towards the workpiece, stresses are high and deformations are large. As the tool oscillates back, stresses in the workpiece are relaxed, and the node moves back due to the material elasticity.

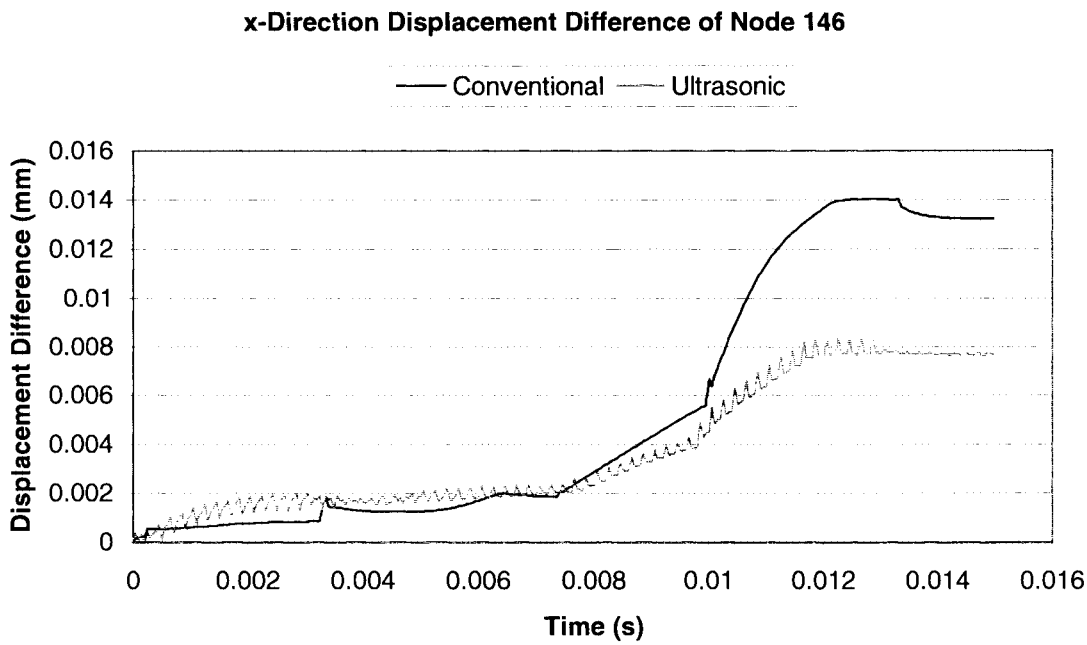

Figure 3.6: x-direction displacement difference of node 146.

In the analysis of the behavior of the workpiece, element 16 is being analyzed. Element 16 is the last element on the cutting path on the lower part of workpiece (see fig.3.2). Fig. 3.7 shows the von Mises stress acting on this element. The average value of the stress in ultrasonic assisted cutting is significantly lower than that of conventional cutting. Consider first the stress curve for conventional cutting. In roughly the first 0.003s, stress is being propagated through the workpiece to element 16. Next, the force acting on the first tied node set is great enough to break the tie, and immediately the stress is being relaxed, causing a decrease at roughly 0.0033s. Subsequent drops can be shown to consistence with the tie breaking time, hence it is concluded that all stress relaxation in conventional cutting process is caused by tie breaking.

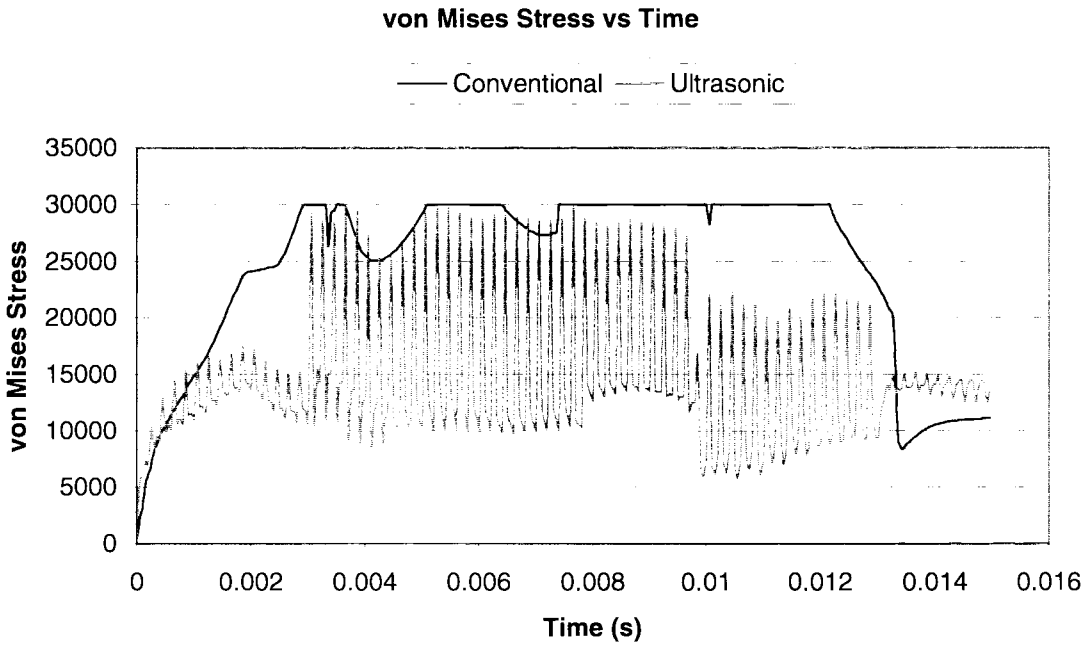

Figure 3.7: von Mises stress vs time.

In contrast with conventional cutting, relaxation of stress occurs periodically in ultrasonic cutting. This allows the material to be relaxed from its elastic deformation. This reduces the resulting plastic deformation. Together with the lower average stress value, this proves that ultrasonic vibration can reduce burr size, which is verified by the simulation. Fig. 3.8 shows the x-directional force acting on element 16. The average value of force in ultrasonic cutting is smaller, causing smaller stress as mentioned previously.

Fig. 3.9 shows the effective plastic strain of the two operations. The final steady state value of the plastic strain of the workpiece under ultrasonic assisted cutting is almost half of that under the conventional cutting process.

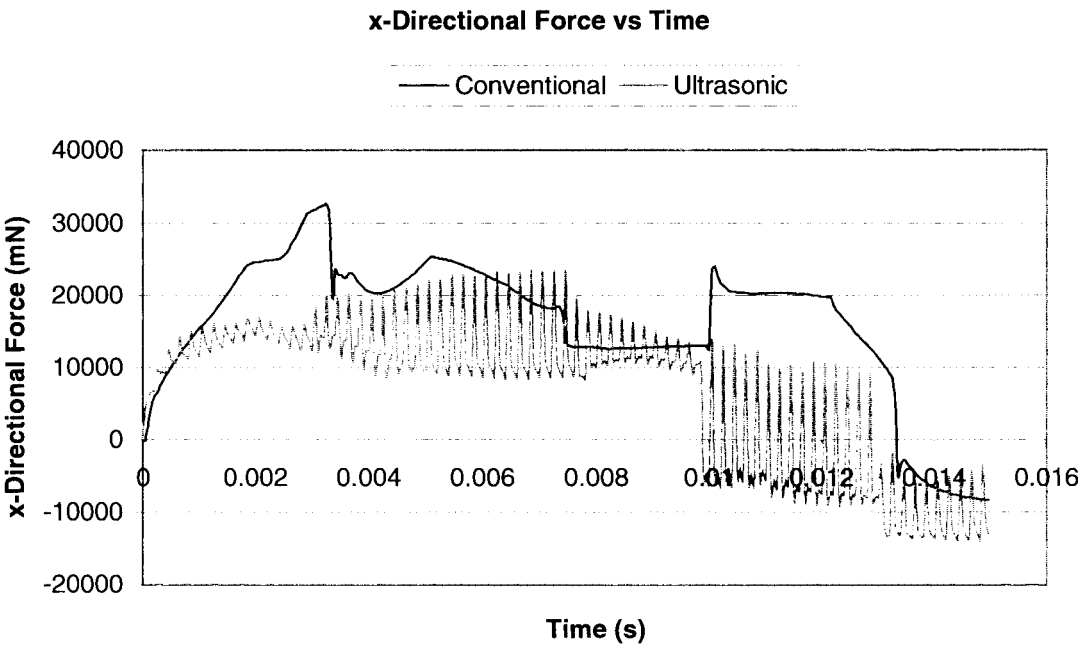

Figure 3.8: x-directional force vs time.

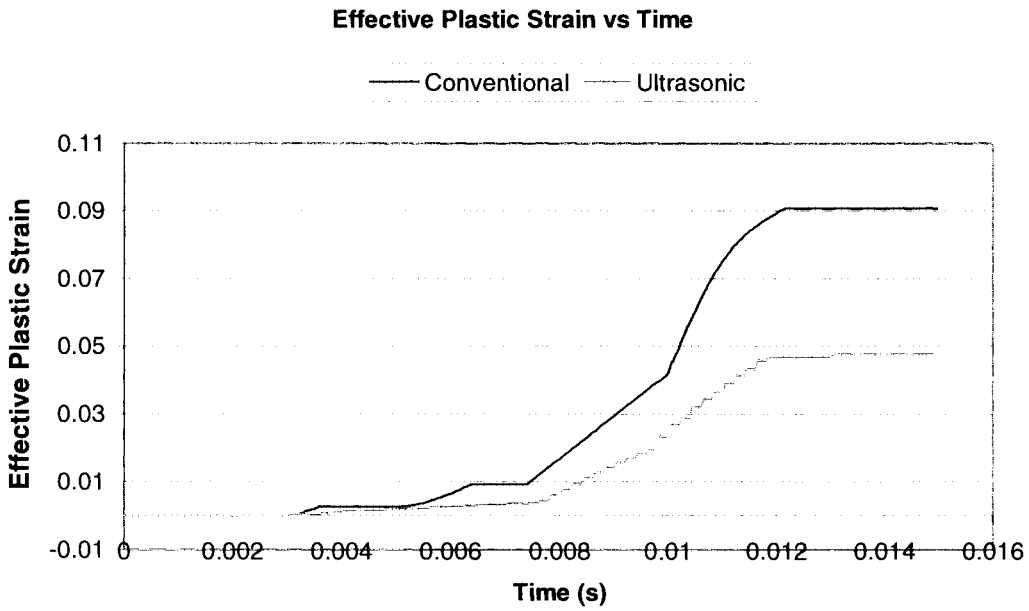

Figure 3.9: Effective plastic strain vs time.

3.8.3 Effect of Vibration Amplitude

Fig. 3.10 shows the burr height of workpiece under ultrasonic assisted cutting with different vibration amplitudes. It is clear that with a higher vibration amplitude and the same frequency, the burr height decreases significantly.

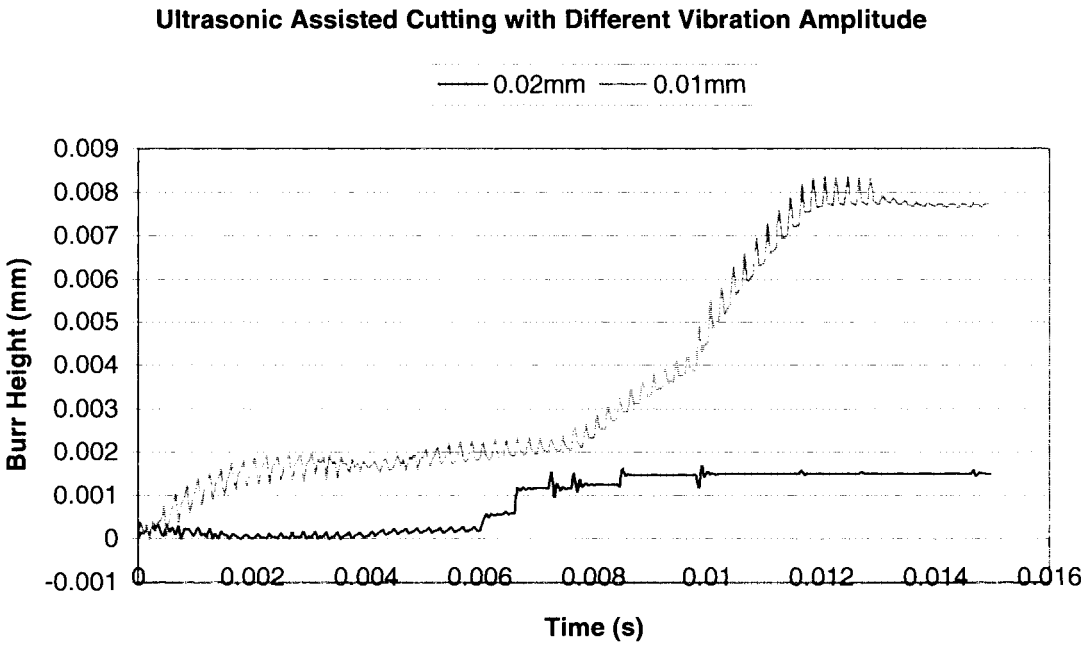

Figure 3.10: Ultrasonic assisted cutting with different vibration amplitudes.

Fig. 3.11 shows the corresponding von Mises stresses. The average value of the stresses with higher vibration amplitude is smaller than that with lower vibration amplitude. Similar experimental findings were presented by Takeyama and Kato [11]. The reason is in ultrasonic assisted cutting, the impact actions of the tool form a secondary cutting mechanism. It is believed that with high amplitude, more material is removed by the ultrasonic impact actions. These impact actions produce small average

stress, which reduce the plastic deformation along the negative shear plane, resulting in more effective prevention/reduction of burr formation.

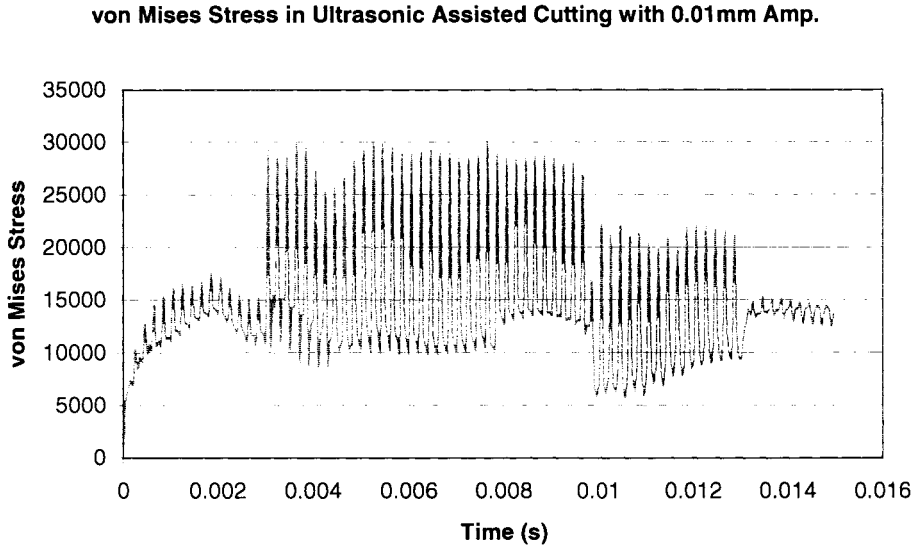

a) Vibration amplitude = 0.01mm.

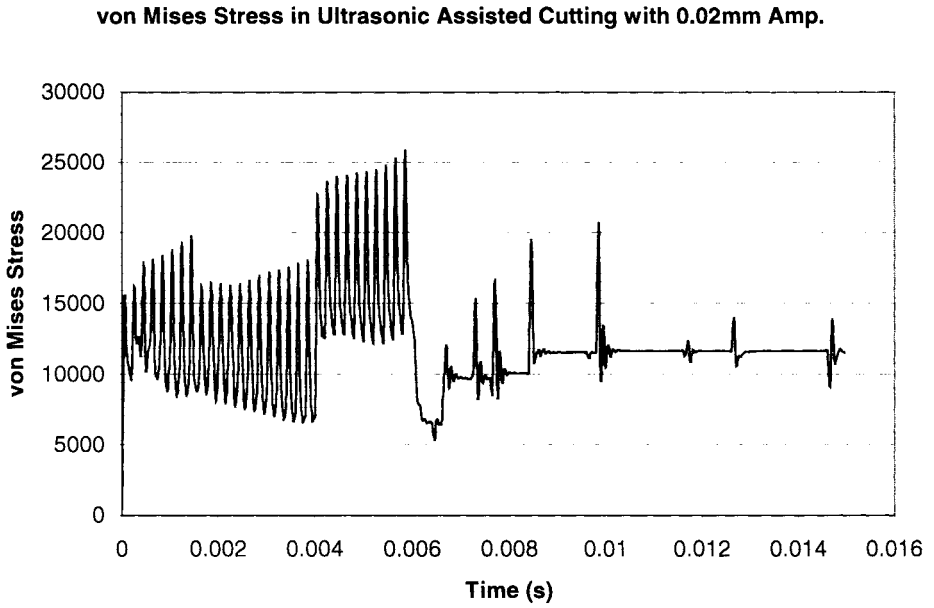

b) Vibration amplitude = 0.02mm.

Figure 3.11: von Mises stress in ultrasonic assisted cutting under different amplitudes.

3.8.4 Effect of Excitation Frequency

Fig 3.12 shows the burr height of workpiece under ultrasonic assisted cutting with the same vibration amplitude (10μm) and different frequencies. The burr height is reduced significantly with the increase in vibration frequency.

Fig. 3.13 shows that the von Mises stress of ultrasonic assisted cutting with a higher vibration frequency is smaller than with a lower frequency. It is believed that with the higher frequency, the rate of stress relaxation is higher, hence less stress is accumulated and the overall stress is reduced.

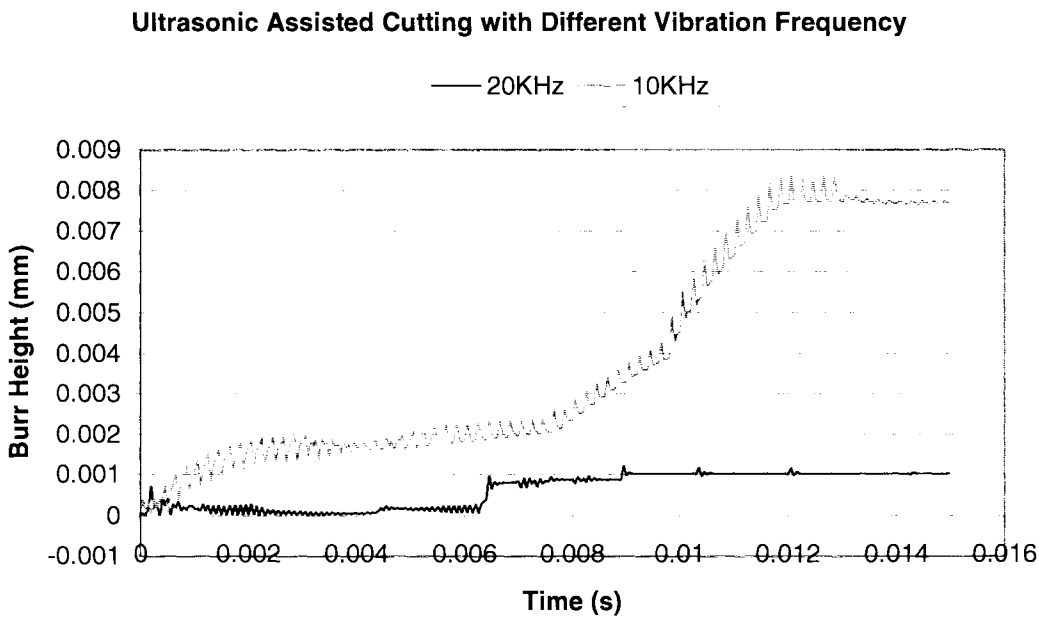

Figure 3.12: Ultrasonic assisted cutting with different vibration frequencies.

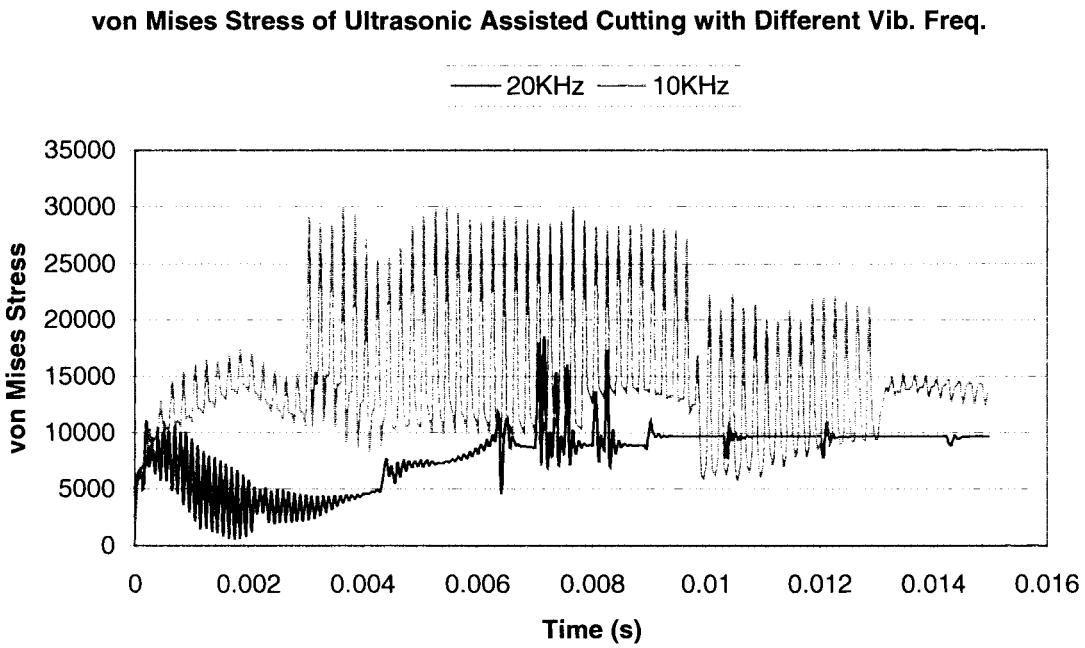

Figure 3.13: von Mises stress of ultrasonic assisted cutting under different Vib. Freq.

3.8.5 Combine Effect of Amplitude and Frequency

From the above simulations one might conclude that the burr size is inversely related to both vibration amplitude and excitation frequency, such that:

$$h \cong CA^{-1} f^{-1} \tag{3.3}$$

where h is the burr height, A the vibration amplitude, f the excitation frequency, and C is a proportionality constant. However, the relationships between these parameters are not as trivial as equation (3.3) states. Fig. 3.14 shows the burr height with different values of controlling parameters.

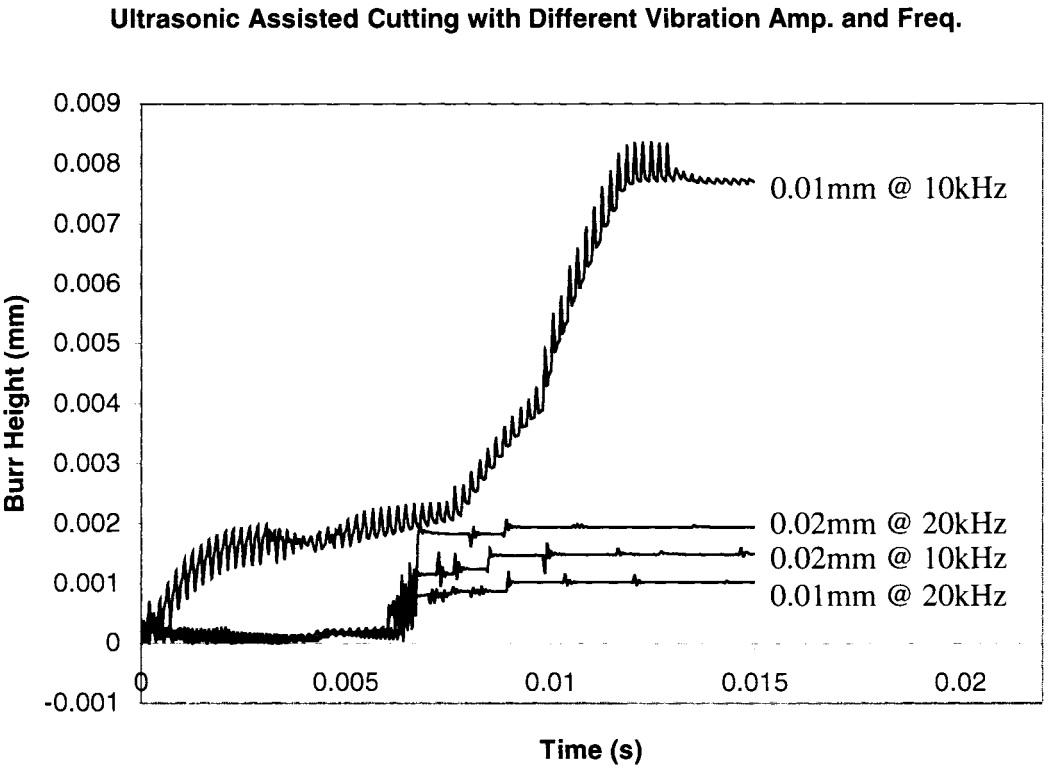

Figure 3.14: Ultrasonic assisted cutting with different vibration conditions.

Although increasing both amplitude and frequency will reduce burr size, the effect is non-linear. Hence, instead of equation (3.3), the following relation is concluded:

$$h = C(A, f)A^{-1}f^{-1} \qquad (3.4)$$

where $C(A,f)$ is a non-linear function with arguments A and f.

3.9 Conclusions

These simulation results show that ultrasonic vibration allows stress relaxation that reduces the average stress acting on the workpiece. This in turn reduces plastic deformation. This characteristic enables cutting with ultrasonic assistance to produce a

higher quality of surface finish and smaller burrs. Ultrasonic vibration has a significant influence on stresses, forces and deformation on the workpiece.

The controlling parameters of ultrasonic assisted cutting are the vibration amplitude and frequency. It was found that increasing both the amplitude and frequency can reduce burr size, although the exact relationship was not found. It is important to note that the results obtained for the simple orthogonal cutting process may not necessary apply to more complex cutting processes.

CHAPTER 4

EXIT BURR MODEL IN ULTRASONIC ASSISTED DRILLING

4.1 Introduction

Exit burr models for machining exist in the literature, but few account for drilling, and none specifically for ultrasonic assisted drilling. Leuderbaugh and Mauch [10] developed an exit burr model predicting only the height of the burr. They used the idea of bending a circular plate under uniformly distributed load, and their experimental results showed consistency with model predictions.

In this chapter an exit burr model for ultrasonic assisted drilling that is primarily based on the work of Leuderbaugh and Mauch [10] is presented. This model predicts both the height and the thickness of the burr. Predicting the thickness is important since the difficulty of deburring is mainly a function of burr thickness.

4.2 Cutting Forces Model

The drill is divided into three cutting regions as in [10]. They are the indentation region on the chisel edge, the orthogonal cutting region on chisel edge, and the oblique cutting region on the cutting lips, as illustrated in Fig. 4.1.

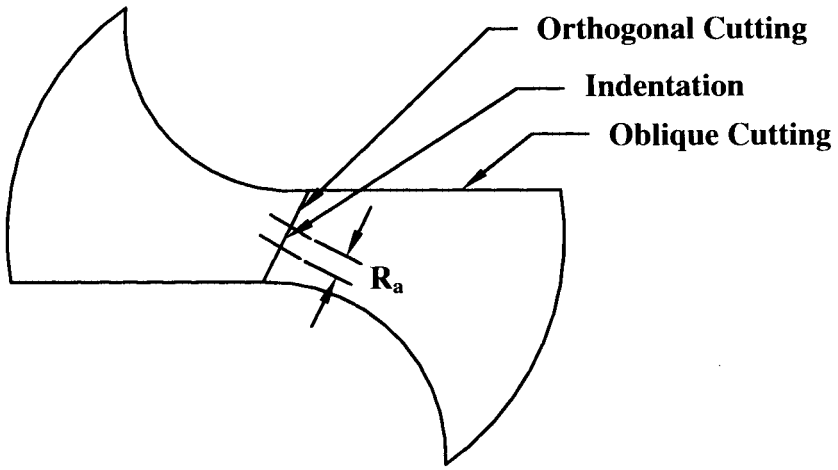

Figure 4.1: Drill cutting region.

4.2.1 Indentation Region

The thrust force on indentation region can be expressed as in [10]:

$$F_I = \frac{8\tau h(1+\varepsilon)\sin p}{\cos p - \sin(p-\varepsilon)} R_a \tag{4.1}$$

where $$2p = \varepsilon + \arccos\left(\tan\left(\frac{\pi}{4} - \frac{\varepsilon}{2}\right)\right) \tag{4.2}$$

$$R_a = \frac{f/2}{\tan(\pi/2 - p)} \tag{4.3}$$

In equations (4.1) to (4.3), τ is the material shear yield strength, h is the depth of indentation, ε can be found from equation (4.2), $2p$ is the point angle, f is the feedrate, and R_a is the transition point of indentation to orthogonal cutting region on the chisel edge.

4.2.2 Orthogonal Cutting Region

The rake angle of a drill varies with its radius, hence, in this cutting region, an effective rake angle is defined as a function of radius [10].

$$\alpha_{e.c} = \alpha + \arctan\left(\frac{f}{2\pi r_i}\right) \tag{4.4}$$

where α is the specified drill rake angle, f is the feedrate and r_i is the instantaneous radius at point of interest on the chisel edge. The corresponding differential thrust force can now be expressed as:

$$dF_o = \frac{t_c \tau \sin(\beta - \alpha_{e.c})}{\sin\phi_c \cos(\phi + \beta - \alpha_{e.c})} dr \tag{4.5}$$

where r is evaluated from R_a, defined above, to R_c, the half length of the chisel edge, and $t_c = f/2$ is the depth of cut, β = arctan μ is the friction factor, μ is the friction coefficient, and ϕ_c is the shear angle. Using Lee and Shaffer's model [13], ϕ_c can be found from:

$$\phi_c + \beta - \alpha_{e.c} = \frac{\pi}{4} \tag{4.6}$$

The total thrust on the orthogonal cutting region is:

$$F_o = 2\int dF_o = \int_{R_a}^{R_c} \frac{t_c \tau \sin(\beta - \alpha_{e.c})}{\sin\phi_c \cos\pi/4} dr \tag{4.7}$$

where the factor of 2 accounts for the two sides of chisel edge.

4.2.3 Oblique Cutting Region

Similar to the orthogonal cutting region in chisel edge, the rake angle of the cutting lip varies with the radius, and an effective rake angle is defined for the cutting lip as (from M. Elhachimi et. al. [2]):

$$\alpha_{e,l} = \alpha_r - \xi \tag{4.8}$$

where $$\alpha_r = \frac{\tan\delta\cos\omega}{\sin p - \cos p\tan\delta\sin\omega} \tag{4.9}$$

$$\xi = \arctan(\tan\omega\cos p) \qquad where \quad 0 \le \xi \le \frac{\pi}{2} \tag{4.10}$$

$$\omega = \arcsin\frac{R_c'}{r} \qquad where \quad 0 \le \omega \le \frac{\pi}{2} \tag{4.11}$$

$$\delta = \frac{d}{2r}\tan\delta_0 \tag{4.12}$$

$$R_c' = R_c\sin\psi' \tag{4.13}$$

In equations (4.9) to (4.13), d is the drill diameter, δ_0 is the drill helix angle at the periphery, R_c' is the half the distance between the two cutting lips, and ψ' is the web angle. The depth of cut along the cutting lips can be defined as (Elhachimi et al. [2]):

$$t_l = \frac{f\sin p\cos\xi}{2} \tag{4.14}$$

The length l and the differential dl length of the cutting lips can be computed by (Elhachimi et al. [2]):

$$l = \frac{1}{\sin p}\sqrt{r^2 - R_c'^2} + R_c\cos\psi \tag{4.15}$$

$$dl = \frac{1}{\sin p} \frac{r}{\sqrt{r^2 - R_c'^2}} dr \tag{4.16}$$

The cutting force components can be determined by oblique cutting theories.

$$dF_Q = \frac{t_l \tau \sin(\beta - \alpha_{e.l})}{\sin \phi_l \cos(\phi_l + \beta - \alpha_{e.l})} dl \tag{4.17}$$

$$dF_P = \frac{t_l \tau \cos(\beta - \alpha_{e.l})}{\sin \phi_l \cos(\phi_l + \beta - \alpha_{e.l})} dl \tag{4.18}$$

where F_Q and F_P are defined in Fig. 4.2, and ϕ_l can again be determined by Lee and Shaffer's Model [13].

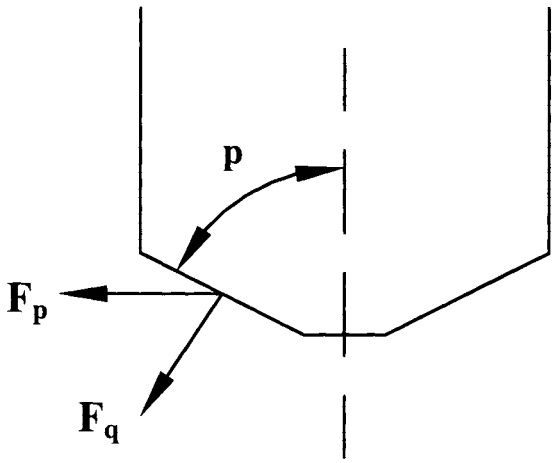

Figure 4.2: Cutting force components on cutting lips.

Hence the total thrust force on the cutting lips can be defined as:

$$F_l = 2\int dF_Q \sin p = 2\int_{R_c}^{R} \frac{t_l \tau \sin(\beta - \alpha_{e.l})}{\sin \phi_l \cos \pi/4} \left(\frac{r}{\sqrt{r^2 - R_c'^2}} \right) dr \tag{4.19}$$

where the factor of 2 accounts for the two cutting lips on a standard twist drill.

4.2.4 Implementation of Cutting Force Model

The cutting geometry of the drill varies with its radius. Therefore it is necessary to break down the cutting regions into elements. In this thesis, it is assumed that burr formation starts when the breakthrough diameter equals the length of the chisel edge (the breakthrough diameter is the instantaneous size of the hole being produced). Therefore only the thrust force acting on the cutting lips region will be computed.

Each cutting lip was broken down into 20 elements. The whole drilling process was broken down into time intervals. At each time interval, the thrust force for each element will be calculated based on equation (4.19). These thrust forces will be used to calculate the deflection of the material below the drill.

4.3 Exit Burr Model

The workpiece under the drill is modeled as a circular plate as in Leuderbaugh and Mauch [10]. The exit burr can then be modeled by studying the bending of this circular plate [10]. Thrust force is assumed to be uniformly distributed on the materials below the drill.

4.3.1 Bending of a Circular Plate Model

The shape and cross-section of the circular plate model is shown in Fig. 4.3.

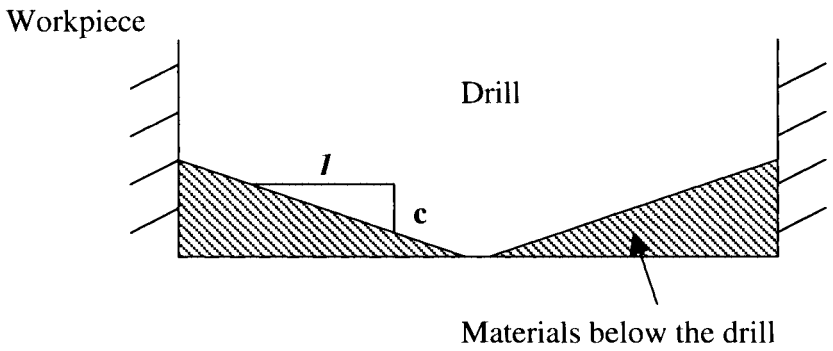

a) Cross section during drilling (prior to deflection).

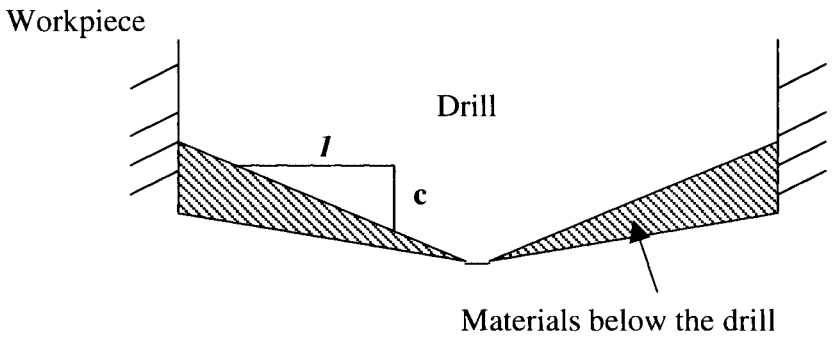

b) Cross section during drilling (deflected).

Figure 4.3: Circular plate bending model.

The solution of the slope of the bottom of a circular plate at a radius r under uniformly distributed load q is [14]:

$$m(r) = A + \frac{B}{r^3} - \frac{16}{3Ec^3}\left(\frac{1}{3}\ln r + \frac{r_i^2}{2r^2}\right) \tag{4.20}$$

where E is the Young's modulus, c is the slope of surface of drill defined in Fig. 4.3, r_i is the radius of the internal edge initially equals half length of chisel edge R_c, r is the instantaneous radius, and A and B are constants that are determined by the boundary conditions.

A and B can be computed as in Leuderbaugh and Mauch [10]:

$$A = \frac{16q}{3Ec^3}\left(\frac{1}{3}\ln a + \frac{r_i^2}{2a^2}\right) + \left(\frac{r_i^3}{r_i^3 - a^3}\right)\left\{\frac{16q}{3Ec^3}\left[\frac{1}{3}\ln\frac{r_i}{a} + \frac{1}{2}\left(1 - \frac{r_i^2}{a^2}\right)\right] - m_i\right\} \tag{4.21}$$

$$B = \left(\frac{a^3 r_i^3}{r_i^3 - a^3}\right)\left\{\frac{16q}{3Ec^3}\left[\frac{1}{3}\ln\frac{r_i}{a} + \frac{1}{2}\left(1 - \frac{r_i^2}{a^2}\right)\right] - m_i\right\} \tag{4.22}$$

The deflection of plate w can be computed by:

$$w = \int m(r)\,dr = Ar - \frac{B}{2r^2} - \frac{16}{3Ec^3}\left(\frac{r}{3}\ln r - \frac{r}{3} - \frac{r_i^2}{2r}\right) + C \tag{4.23}$$

where C is the constant of integration, which can be computed by the boundary condition:

$$r = a, \quad w = 0 \tag{4.24}$$

hence,

$$C = \frac{16}{3Ec^3}\left[\frac{a}{3}(\ln r - 1) - \frac{r_i^2}{2a}\right] - Aa + \frac{B}{2a^2} \tag{4.25}$$

The radial and tangential stresses can be computed as [14]:

$$\sigma_r = \frac{6}{a^2} D\left[\frac{dm(r)}{dr} + \nu_P \frac{m(r)}{r}\right] \tag{4.26}$$

$$\sigma_t = \frac{6}{a^2} D\left[\frac{m(r)}{r} + \nu_P \frac{dm(r)}{dr}\right] \tag{4.27}$$

where ν_P is the Poisson's ratio, and D is the flexural rigidity and can be computed by:

$$D = \frac{Ec^3 r^3}{12\left(1 - \nu_P^2\right)} \tag{4.28}$$

Using the von Mises criterion, the material will not fail if:

$$\sigma_r^2 - \sigma_r \sigma_t + \sigma_t^2 < \sigma_Y^2 \tag{4.29}$$

where σ_Y is the yield stress of the material. This criterion will be used to determine if the plate will form a burr or continue being cut.

4.3.2 Implementation of Bending of a Circular Plate Model

With the thrust force calculated in section 4.2.4, deflection can be calculated for each element. The effective depth of cut in the next time interval for each element will be calculated as the advance of the drill at each interval less this deflection, or the thickness of the remaining material below the drill (in the corresponding element), whichever is less.

The stress in the element closest to the periphery of the hole will also be calculated and monitored. This element represents the support of the circular plate. If this element failed based on the von Mises criterion, the support of the circular plate fails. The material below the drill will not be cut and pure deformation occurs (transition period). This material will form a burr, and its thickness equals the width of the burr, its length equals the height of the burr.

4.4 Ultrasonic Assistance Model

In this thesis, only ultrasonic assistance in the feed direction is modeled. The displacement of the tool is calculated as:

$$d_u(t) = A_u \sin(2\pi f_u t) + ft \tag{4.30}$$

where A_u is the vibration amplitude, f_u the vibration frequency, f is the feed of drill, and t is the instantaneous time. Hence the effective drill feed is:

$$f_u(t) = 2\pi F_u A_u \cos(2\pi F_u t) + f \tag{4.31}$$

In the computation of the thrust force, when the uncut chip thickness less than or equal to zero, the drill is not in contact with the material, and the force equals zero. The effect of the relaxation of the elastic deformation of material included in Chapter 3 was not included in the current model.

4.5 Exit Burr Simulation for Ultrasonic Assisted Drilling

4.5.1 Overview

A Matlab program was written to estimate the burr height and width produced after drilling with and without ultrasonic assistance. Different frequencies and peak to peak magnitudes were considered and are summarized in Table 4.1. The cutting and ultrasonic assistance conditions are summarized in Table 4.2.

Simulation #	Ultrasonic Assistance Condition
1	None
2	10kHz @ 4μm
3	15kHz @ 4μm
4	20kHz @ 4μm
5	20kHz @ 2.66μm
6	20kHz @ 1.33μm

Table 4.1: Simulated ultrasonic assistance conditions.

Spindle speed	Feed	Drill diameter	Helix angle at periphery	Web angle	Point Angle
4000 rpm	1.905 mm/s	3.175 mm	60°	45°	115°

Table 4.2: Cutting condition being simulated.

4.5.2 Simulation Results

Table 4.3 to 4.4 and Fig. 4.4 to 4.7 can summarize the simulated burr size.

Frequency (kHz)	Height (mm)	Width (mm)
0	0.5156	0.0952
10	0.49739	0.09134
15	0.49715	0.0913
20	0.49706	0.09127

Table 4.3: Simulated burr size vs vibration frequency @ 4μm Pk-Pk magnitude.

Magnitude (μm)	Height (mm)	Width (mm)
0	0.5156	0.0952
1.33	0.50978	0.09397
2.67	0.50318	0.09257
4	0.49706	0.09127

Table 4.4: Simulated burr size vs vibration magnitude @ 20kHz frequency.

The model predicts burr size decreases when vibration frequency increases. It also predicts burr size varies linearly with vibration amplitude. However, the magnitude of the reduction is not significant. This contradicts the findings from previous literature and the simulation in Chapter 3. It is important to note that the relaxation of the elastic deformation of the material below the drill is not included in the current model. This dynamic behavior may contribute significantly to the reduction of burr size.

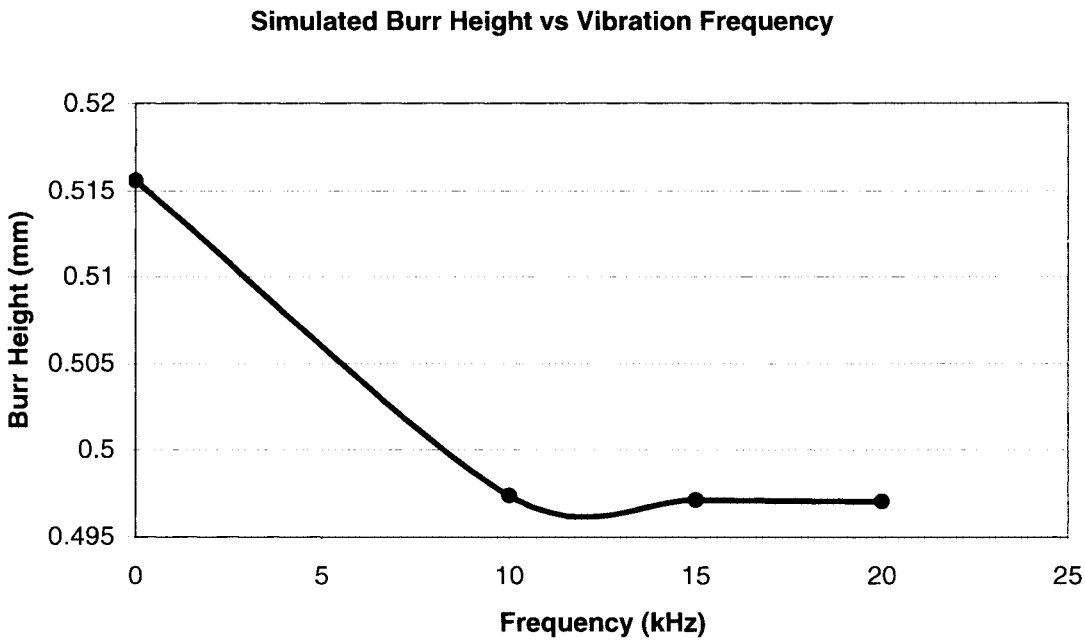

Figure 4.4: Simulated burr height vs vibration frequency.

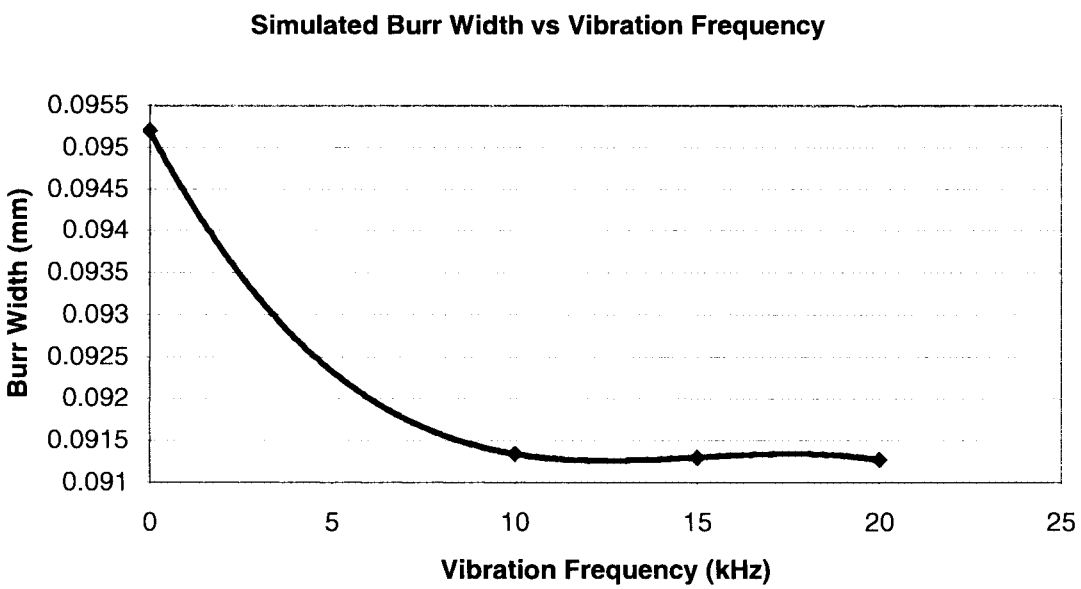

Figure 4.5: Simulated burr width vs vibration frequency.

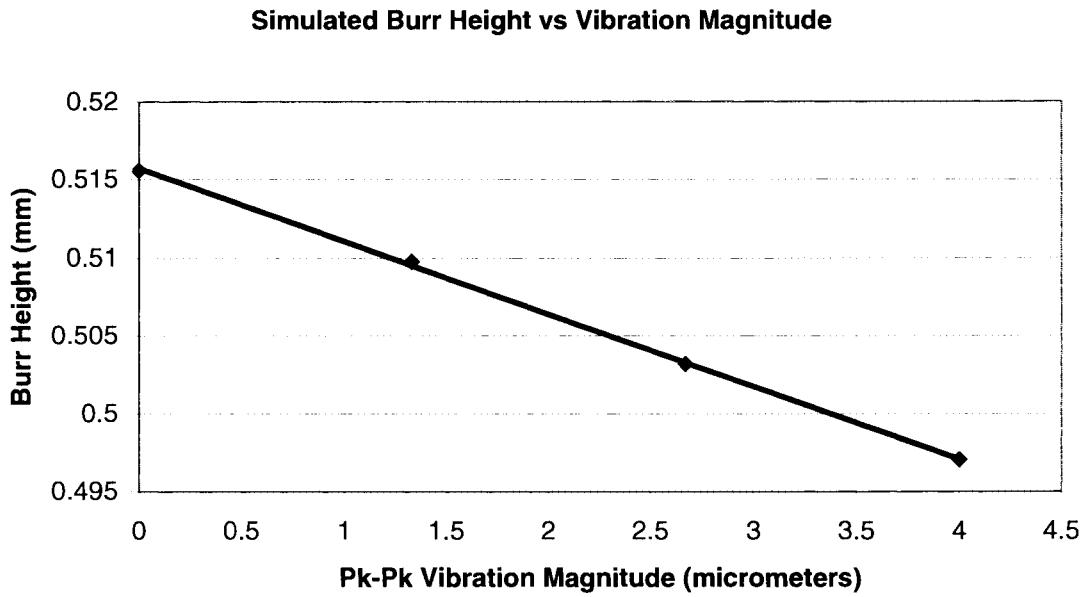

Figure 4.6: Simulated burr height vs vibration amplitude.

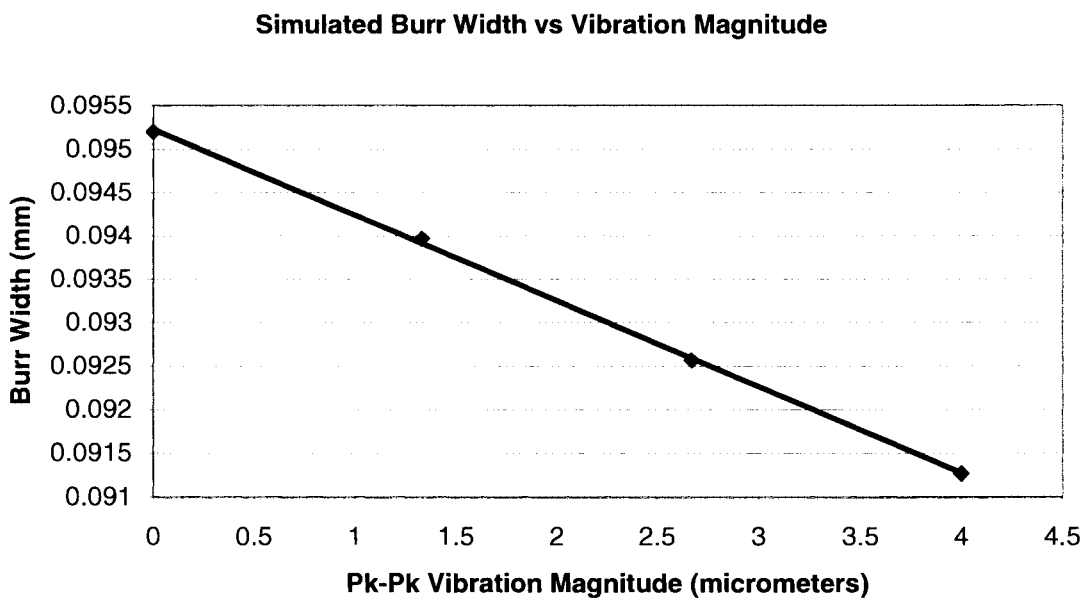

Figure 4.7: Simulated burr width vs vibration amplitude.

4.5 Conclusion

A simplified exit burr model for ultrasonic assisted drilling was presented. The model extends prior work by estimating the burr width and by incorporation the ultrasonic assistance. The model assumed burr initialization occurs when the breakthrough diameter equals the length of chisel edge, hence simplifying the force analysis to oblique cutting on cutting lips only. This assumption is valid in this thesis because small drills are being used (drill diameter < 1/8"), and the effects of the thrust force produced on the chisel edge are relatively insignificant. Bending of a circular plate with time varying thickness under a uniformly distributed load is used to model the bending behavior and to predict the deflection of the material in front of the drill. The von Mises criterion is used to determine when the transition period occurs. Ultrasonic assistance is modeled by superimposing the vibration displacement in onto the feed direction.

Simulation results show inconsistencies with the finite element modeling presented in Chapter 3. This is most likely due to ignoring of the dynamic behavior of the material below the drill. Improvement in this model is necessary before it can be uses to predict burr size accurately.

CHAPTER 5

DESIGN OF THE TESTING EQUIPMENT

5.1 Introduction

In the chapter the required testing equipment for ultrasonic assisted drilling is developed. A suitable actuator was selected and purchased. A workpiece holder and a drive circuit for the actuator was then designed, built and tested.

5.2 Selection of the Actuator

5.2.1 Overview

The required performance of the actuator must first be defined. The actuator will be used to vibrate the workpiece. The basic design is shown in Fig. 1.4(b). The desirable vibration condition is 20kHz and 10μm (after Takeyama and Keto [11]). The actuator must be capable to produce sufficient force to drive the combined mass of the diaphragm, workpiece holder and workpiece at this condition.

5.2.2 Force Analysis

The vibration of the workpiece can be modeled by simple harmonic motion. Referring to the free body diagram of an actuator and workpiece as shown in Fig. 5.1, the vibration displacement *X(t)* of the workpiece is:

$$X(t) = A_u \sin(2\pi f_u t) \tag{5-1}$$

and the corresponding velocity *V(t)* and acceleration *a(t)* can be expressed as:

$$V(t) = \dot{X}(t) = 2\pi f_u A_u \cos(2\pi f_u t) \tag{5-2}$$

$$a(t) = \ddot{X}(t) = -4\pi^2 f_u^2 A_u \sin(2\pi f_u t) \tag{5-3}$$

In equation (5-1) to (5-3), A_u is the vibration amplitude and F_u is the vibration frequency. Hence, driving a mass m_w, representing the combined mass of the diaphragm, workpiece holder and workpiece, requires a force of:

$$F_w = m_w a(t) = -4\pi^2 f_u^2 m_w A_u \sin(2\pi f_u t) \tag{5-4}$$

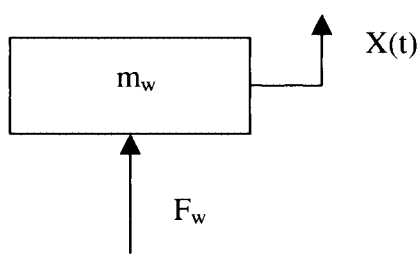

Figure 5.1: Free body diagram of an actuator and workpiece.

The maximum force magnitude is given by:

$$F_{wMAX} = 4\pi^2 f_u^2 m_w A_u \tag{5-5}$$

In this thesis, the maximum drill size being tested is 3mm. The thickness of the specimen must be large enough to ensure the whole cutting lip is in contact with the workpiece. In this case, a thickness of 1mm is sufficient, and a thickness of 1.6mm was chosen. The size of the workpiece was chosen to be 25.4mm x 25.4mm. Such an aluminum workpiece will have a mass of 10g. m_w was then chosen to be 100g in the design criteria. Substituting f_u = 20kHz, A_u = 10μm and m_w = 100g into (5-5), the maximum force required is F_{wMAX} = 7.9kN.

The required specification of the actuator is summarized in Table 5.1.

Frequency Range	Displacement Range	Force Delivery
0-20kHz	0-10μm	8kN

Table 5.1: Required specification of the actuator.

5.2.3 Available Industrial Actuators

The actuators available in the current market were investigated. It was found that an actuator satisfying the requirement summarized in Table 5.1 is not readily available. Although a custom designed actuator can be made, it's cost exceeds the available budget. In Table 5.2 the prices of different actuators are summarized.

	Freq. Range (kHz)	Disp. Range (μm)	Force Delivery (kN)	Price (CAD)
Sensor Tech (BM532)	0-20	0-4	5	200
PI Tech (P-802.00)	0-13	0-6	1	250
Custom Design [15]	0-20	0-10	8	7000

Table 5.2: Summary of industrial survey on actuator.

Among the available options, a stack actuator manufactured by Sensor Tech. Ltd. (BM532 series) was chosen. A stack actuator consists of layers (33 layers in the chosen actuator) of piezoelectric disks bonded together. Although this actuator does not fully meet the required specifications it offered the best combination of performance and price.

It is expected that the amount of burr reduction will be reduced due to the lower available actuator displacement. However, it is believed that the chosen actuator can demonstrate the effect of ultrasonic assistance in burr size reduction. Some of the specifications of this actuator are presented in table 5.3. The total thickness of the actuator is 25.4mm (this includes the insulators on both ends), and the outer diameter is 25.4mm.

Number of layers	Layers thickness	Voltage	Displacement	Charge coefficient	Capacitance
33	0.5mm	200V	4μm	280×10^{-12} C/N	290nF

Table 5.3: Manufacturer's specification of the actuator.

A simplified relationship between the voltage V_a and displacement D is:

$$D = V_a N d_a \tag{5-6}$$

where N is the number of layers and d_a is the charge coefficient of the piezoelectric material. It should be noted that equation (5-6) serves only as an approximated prediction for displacement of the actuator.

5.3 Selection of the Power Amplifier

5.3.1 Requirement of the Power Amplifier

A suitable power amplifier is required to drive the actuator properly. The chosen actuator requires a drive voltage of 200V to produce its maximum displacement (4μm). The power amplifier is then required to produce a potential difference of 0-200V periodically at 20kHz.

Another important factor in choosing the power amplifier is the drive current it can deliver (in other words, its power delivery). In general, an actuator can be electrically modeled as a capacitor and a resistor connected in parallel as shown in Fig. 5.2 (Kim and Nam [16]). The internal resistance of the actuator is relatively high (typically higher than 1MΩ). Most of the current delivered by the power amplifier will pass through the capacitor in the model. The required charging current can be computed as:

$$C\frac{dV_C}{dt} = i_C \tag{5-7}$$

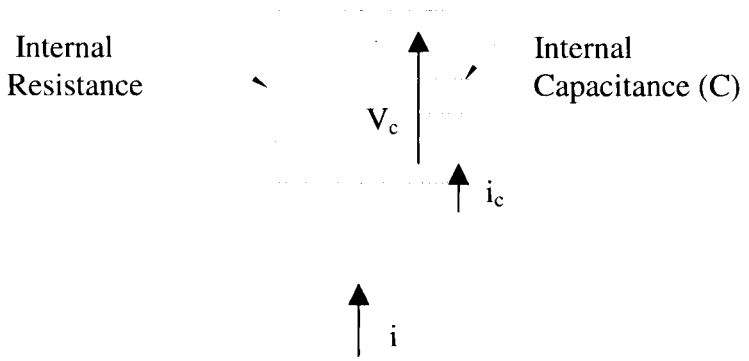

Figure 5.2: Piezoelectric actuator electrical model.

The desired actuator's voltage is presented in Fig. 5.3. A linear approximation (dash line) is used to estimate the required drive current.

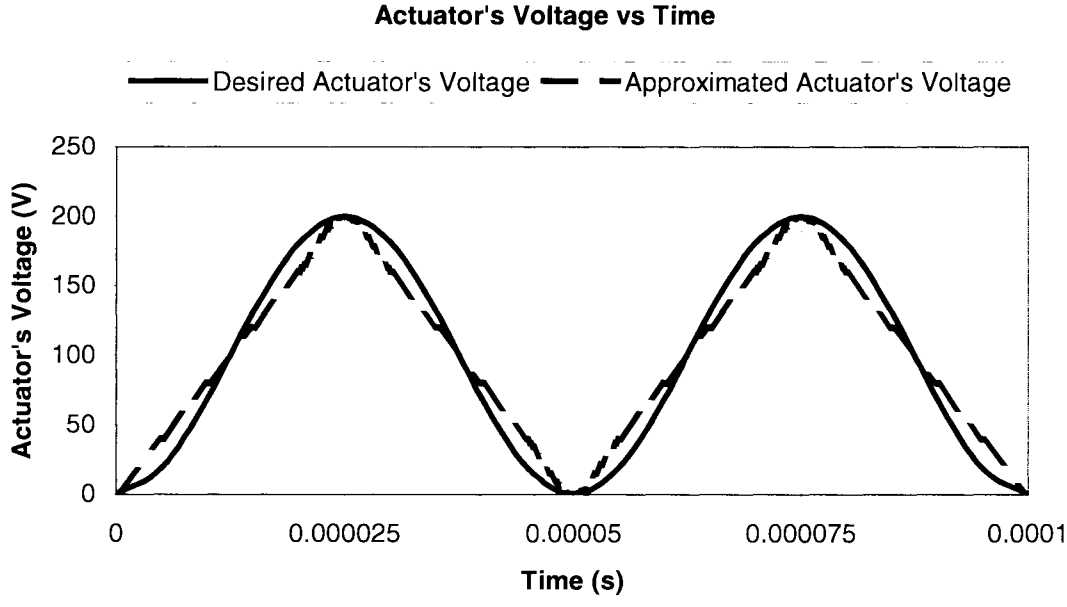

Figure 5.3: Actuator's voltage vs time.

From Fig. 5.3 the actuator's voltage will rise from 0 to 200V in 25μs. Therefore in (5-7), $\frac{dV_C}{dt} \approx \frac{200V}{25\mu s} = 8\times10^6\, V/s$. Substituting the actuator's capacitance (290nF), the required drive current $i_C = C\frac{dV_C}{dt} = \left(290\times10^{-9}\right)\left(8\times10^6\right) = 2.3A$. In reality, it is always higher. The minimum requirement of the power amplifier is summarized in table 5.4.

Frequency Range	Voltage Delivery	Current Delivery
0-20kHz	0-200V	2.3A

Table 5.4: Required specification of the power amplifier.

5.3.2 Survey of Industrial Power Amplifier

The available power amplifiers in the current market were investigated. It was found that although a suitable power amplifier is readily available, it cost around $7000CAD, exceeding the budget for this thesis. It is believed that these power amplifiers have many different functions that are not required in this thesis. Hence a custom drive circuit will be designed. The design will be presented in section 5.5.

5.4 Design of Workpiece Holder

5.4.1 Overview

The workpiece is driven by the Sensor Tech. piezoelectric stack actuator. Because the actuator consists of bonded layers, it cannot withstand large tensile forces. It was shown in section 5.2.2 that the maximum force required to drive the workpiece is 7.9kN. This exceeds the maximum allowable tensile load for the chosen actuator (1kN). A preloading mechanism is required to assist the workpiece's withdrawal action and to protect the actuator, as shown in Fig. 5.4.

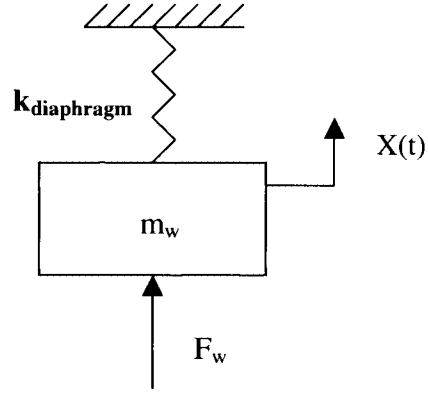

Figure 5.4: Free body diagram of actuator and workpiece with preload mechanism.

5.4.2 Design of the Preloading Mechanism

A circular diaphragm is used to preload the actuator. For a displacement of 4μm at 20kHz, the maximum actuator force delivery will be 3.16kN according to (5-5). The stiffness of the diaphragm must therefore be capable of delivering 3.16kN at a deflection of 4μm to prevent tensile loading. Type 302 stainless steel will be used to build the diaphragm. It is expected that its yield stress is high enough such that the diaphragm can deliver the required load without plastically deformed.

A finite element analysis was performed to determine the required thickness of the diaphragm. The model assumes constant load is evenly distributed on the area where the actuator will be in contact with the diaphragm, as shown in Fig. 5.5. It was found that a circular disk with a 76.2mm (3 inches) diameter and a 0.794mm (1/16 inch) thickness is capable of delivering the required preload at 4μm displacement. The maximum stress on the diaphragm is 3.24MPa, which is smaller than its yield stress (255MPa). This verified that no plastic deformation will occur. The simulation result is shown in Fig. 5.6.

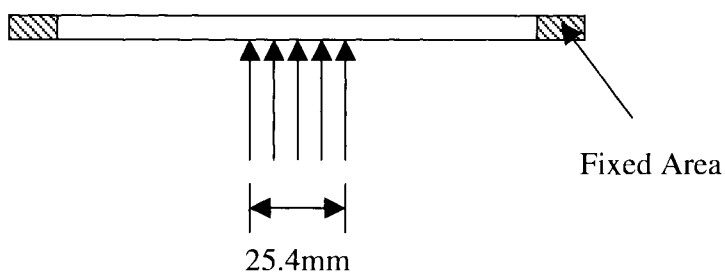

Figure 5.5: Cross section of the loading distribution on the diaphragm.

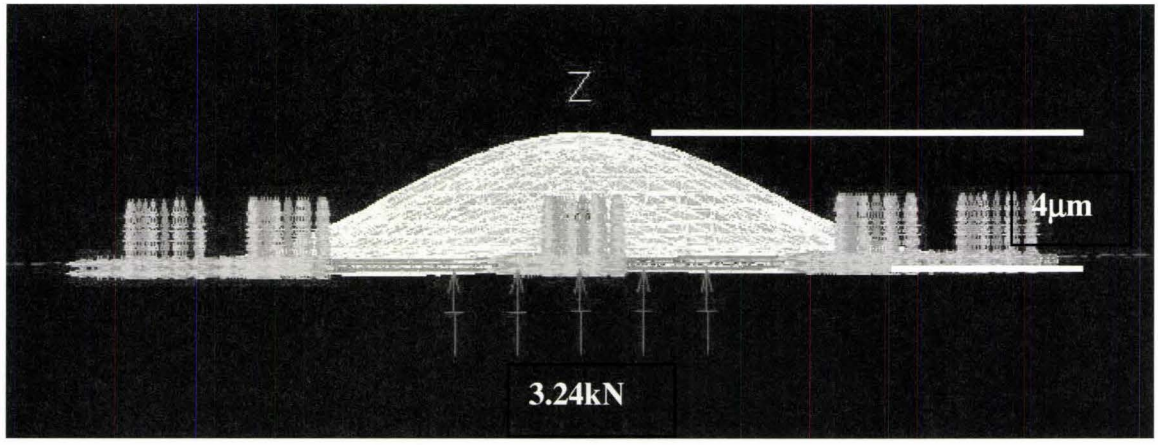


```
RESULTS: 3- B.C. 1,STRESS_3,LOAD SET 1
STRESS - VON MISES MIN: 5.55E-05 MAX: 3.24E+00
DEFORMATION: 1- B.C. 1,DISPLACEMENT_1,LOAD SET 1
DISPLACEMENT - MAG MIN: 0.00E+00 MAX: 3.97E-03
FRAME OF REF: PART
```

Figure 5.6: Simulation results.

It is important to note that this model simulated the static response of the diaphragm only. However, the stiffness of the diaphragm will be higher under dynamic loading, as long as the operating frequency is away from the combined mass's resonance frequency. The stiffness of the diaphragm $k_{diaphragm} = \frac{3.16kN}{4\mu m} = 7.9 \times 10^5 N/m$. Since the combined mass m_w = 0.1kg, the resonance frequency of the diaphragm is therefore $f_{n.diaphragm} = \frac{1}{2\pi}\sqrt{\frac{k}{m}} = \frac{1}{2\pi}\sqrt{\frac{7.9 \times 10^5}{0.1}} = 450Hz$. Since the operating frequency is 20kHz, which is far above the combined mass's resonance frequency, this approximation is considered acceptable.

5.4.3 Workpiece Holder

An aluminum holder is used to hold the workpiece on top of the diaphragm. It has a 7.94mm (5/16 inch) diameter by 7.62mm (0.3 inch) deep cavity at the center. This cavity provides room for the tool to penetrate the workpiece. The mass of this holder is less than 50g, and the actuator can deliver sufficient force to drive the holder and workpiece dynamically.

The workpiece holder is bonded to the diaphragm by a #4 bolt. The whole structure was fixed on a stainless steel shell and bottom plate. Stainless steel is chosen to avoid rust and ensure the rigidity of the whole structure. The actuator is squeezed between the diaphragm and the bottom plate. Fig. 5.7 shows the cross section of the design. Part drawings are presented in Appendix A.

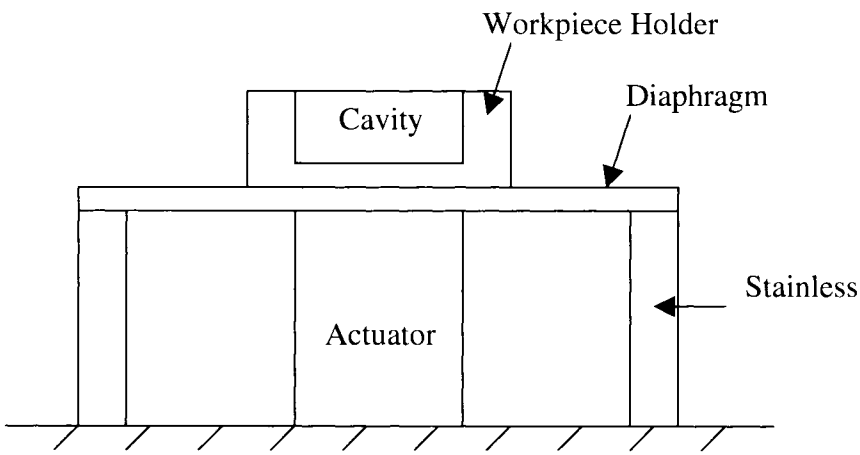

Figure 5.7: Cross section of workpiece holder.

5.5 Design of the Drive Circuit

5.5.1 Overview

The design of the drive circuit is more complicated than that of the workpiece holder. An appropriate drive circuit for the actuator is critical for proper operation. The circuit must provide all the necessary signal characteristics to the actuator at the desired frequency. These include the supply voltage, current and the corresponding power. To keep it as simple and inexpensive as possible, a circuit that switches the voltage supplied to the actuator will be used. The resulting motion of the workpiece will not be a smooth sine curve. However, it is believed that the form of motion is not important in burr size reduction.

5.5.2 On/Off Drive Circuit Design

Fig. 5.8 shows the initial design of the drive circuit. Recall from Table 5.4 that the minimum voltage and current requirements are 200V and 2.3A respectively. The full-wave rectifier (by International Rectifier) converts the ac current to a positive ac wave, which charges up the capacitor. The capacitor is used to hold the voltage at 200V. Its capacitance (2200μF) was chosen to ensure the ripple of the voltage is acceptable. The combination of rectifier and capacitor converts the ac current to dc current.

A power MOSFET was carefully chosen to switch the lower part of the circuit on and off at a maximum of 20kHz switching frequency. IRF710 MOSFET from International Rectifier was selected. Its allowable drain to source voltage and current is higher than 200V and 2.3A respectively. When the MOSFET is on, there is a voltage

difference between the high voltage side (200V, from the capacitor) and the low voltage side (0V, from the ground). Current passes through the actuator, which responds with a mechanical displacement that pushes the diaphragm upwards.

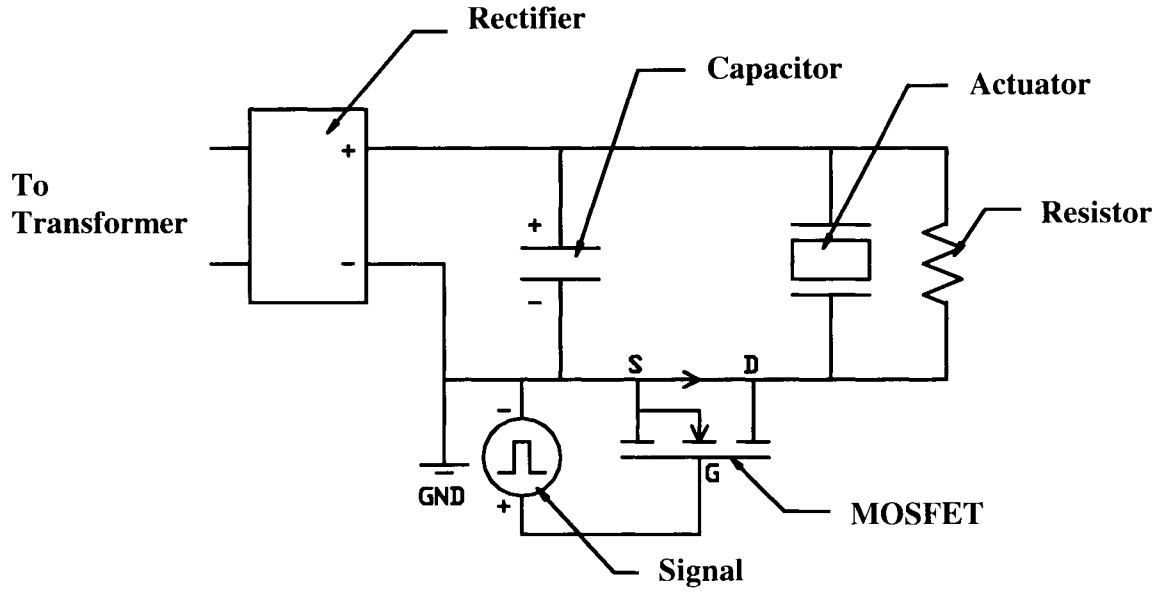

Figure 5.8: On/Off drive circuit design layout.

When the MOSFET is off, no current flows between the drain and source, and the only closed circuit is the loop consisting the actuator and the resistor. The actuator then discharges until there is no voltage difference between its two ends and its displacement returns to zero. The resistor value is chosen carefully to ensure the loop allows sufficient current to discharge the actuator. The governing equation is:

$$R = \frac{V}{I} \tag{5-7}$$

With a voltage difference of $200V$, and a required minimum current of $2.3A$, the maximum allowable resistance is 87Ω. A 50Ω resistor is chosen to ensure sufficient

current is available. Fig. 5.9 shows the simulated response of the circuit operating at $200V$ and $20kHz$.

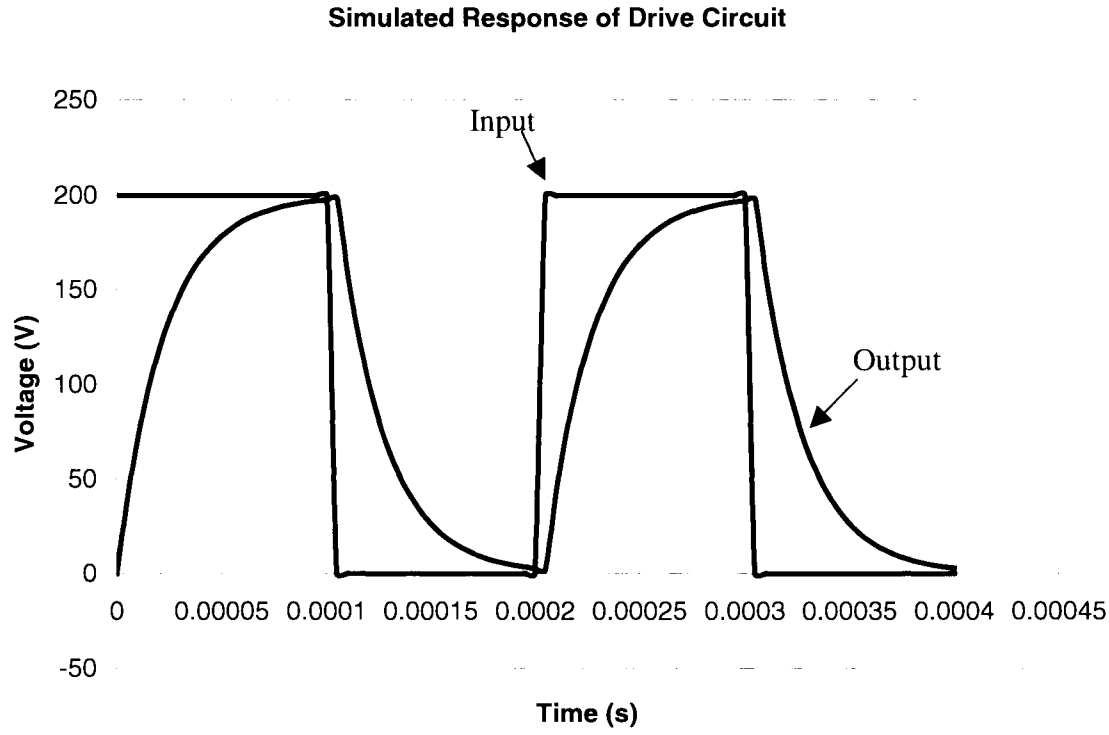

Figure 5.9: Simulated response of the drive circuit.

However, experiments demonstrated that the drive circuit failed to drive the actuator properly. Investigations show that the current circuit overlooked the following issues.

i) Overheating Resistor

It is believed that, when the MOSFET is off, the power dissipated by the resistor can be very high. This occurs for fractions of a second only, and the dissipation decreases drastically as the actuator discharges. This argument can be supported by the power equation:

$$P = VI = \frac{V^2}{R} \tag{5-8}$$

Hence, the power is proportional to V^2, which means if voltage drops by half, the power drops by a factor of 4. It was therefore believed that the power dissipation from the resistor would be acceptable. Most of the power is dissipated as heat. In practice the heat dissipated from the resistor too slowly, causing it to overheat and fail.

ii) Overloading Capacitor

The capacitor was chosen to be able to supply 2.5*A* of current constantly. However, two issues were being overlooked. The resistor (which used to discharge the actuator) also drains current, increasing the current load on the capacitor. Moreover, although the actuator requires a minimum current of 2.3*A* to operate at the desired condition, the corresponding capacitive reactance of the actuator at 20kHz is 27.3Ω, which implies it will drain 5.9*A* of current directly from the capacitor. Hence, the capacitor was overloaded, and failed during one of the tests.

5.5.3 Series RLC Resonance Circuit

Another possible solution is a series RLC resonance circuit. This circuit involves adding an inductor and resistor to the actuator. By carefully choosing the resistor and the inductor and some fine tuning, it is possible to drive the actuator to the circuit resonance. Hence it is possible to drive the actuator at 200V with only a 10V supply, reducing the overall power consumption of the circuit and the power dissipation from individual

component. A typical circuit layout of a series RLC resonance circuit is being shown in Fig. 5.10.

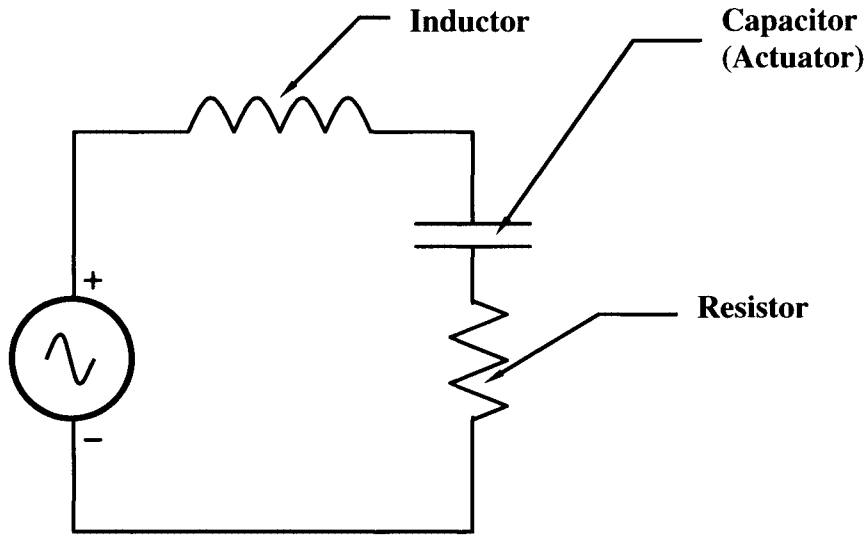

Figure 5.10: Typical Series RLC Resonance Circuit

The voltage that passes through the capacitor can be determined by:

$$V_C = V_{IN}\left(\frac{1}{R}\right)\sqrt{\frac{L}{C}} \tag{5.9}$$

The resonant frequency of the circuit can be determined by:

$$\omega_0 = \frac{1}{\sqrt{LC}} \tag{5.10}$$

The required driving current can be determined by:

$$I_C = \frac{V_C}{\sqrt{R^2 + \left(\omega_0 L - \frac{1}{\omega_0 C}\right)^2}} \tag{5.11}$$

Hence, to deliver 200V through actuator at 20kHz using a 10V supply signal generator, a 0.34H inductor and 54.1Ω resistor is required, and the required minimum current is 4.7mA. With some tuning, this method might be a solution. However, in this thesis a different approach involving polarity switching was implemented.

5.5.6 Polarity Switching Drive Circuit

The proposed drive circuit switches the polarity of voltage supplied to the actuator. Fig. 5.11 shows the corresponding circuit layout. IRF710 MOSFETs and IR2108 half bridge drivers from International Rectifier are used.

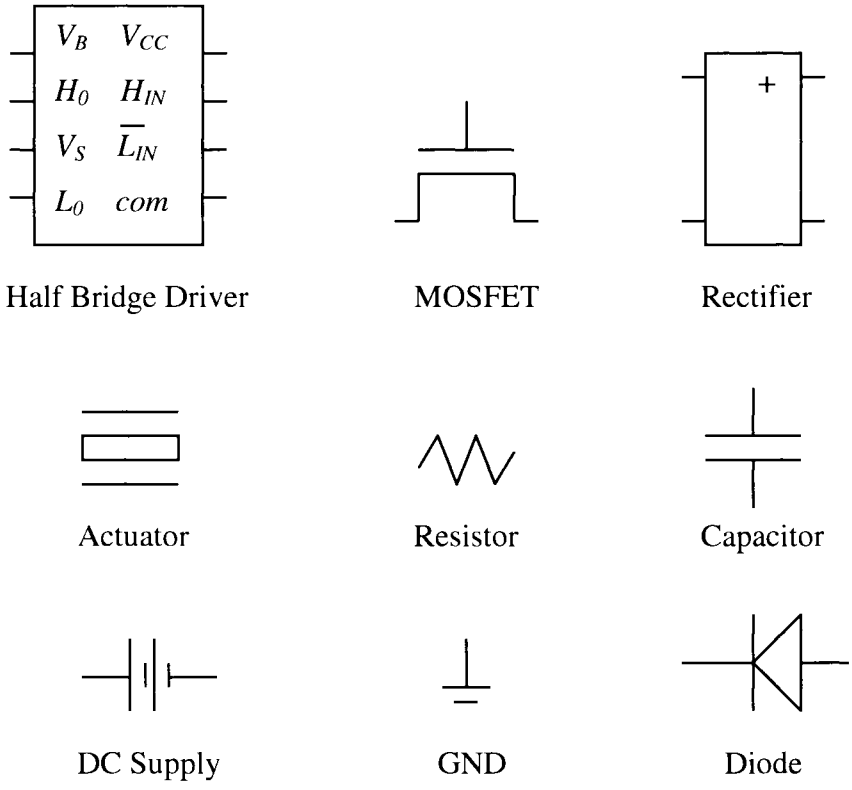

a) Polarity switching circuit components.

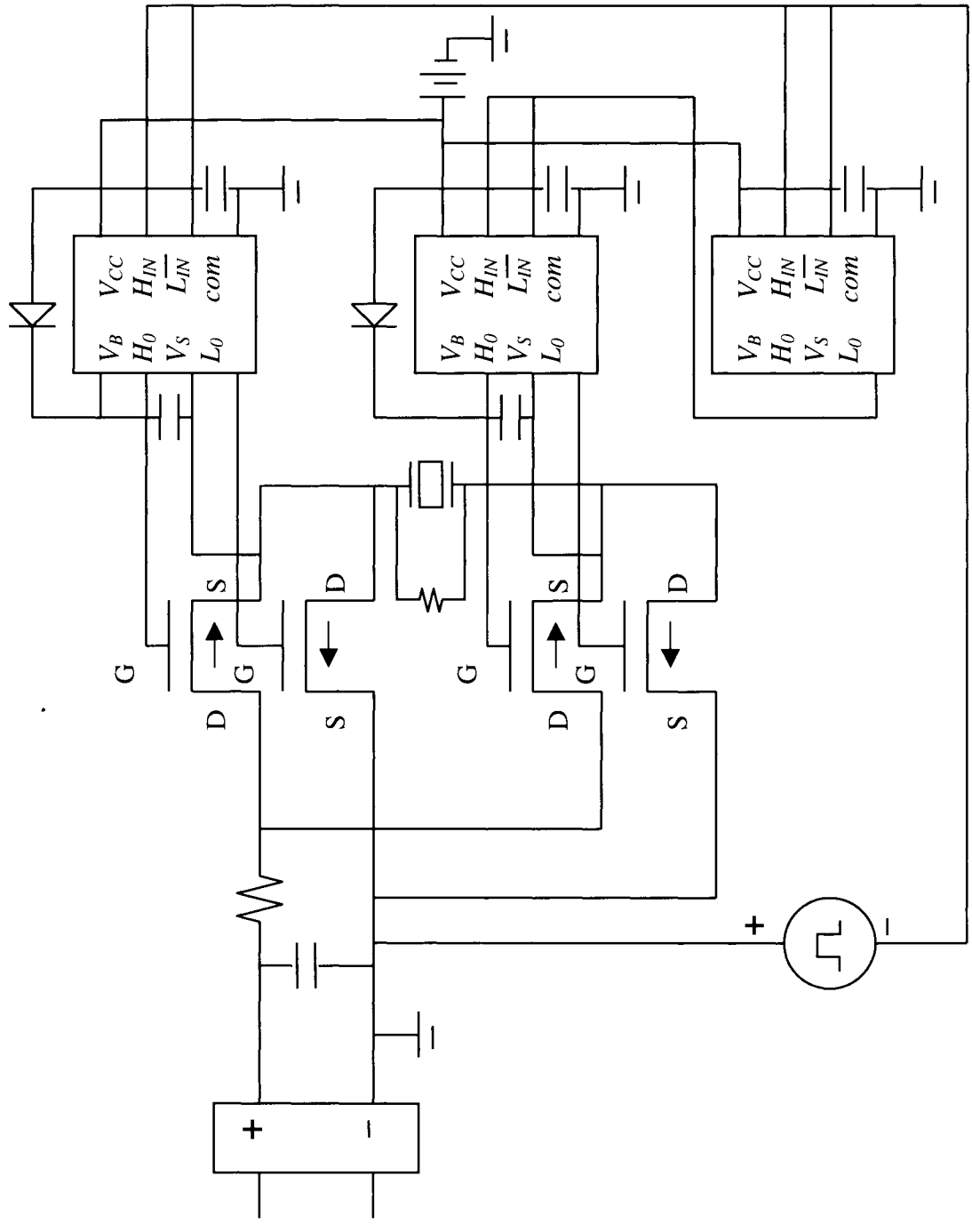

b) Polarity circuit layout.

Figure 5.11: Polarity circuit design.

The polarity of the actuator is monitored by two sets of MOSFETs. Each set contains two MOSFETs, one connects to the positive voltage supply, and one connects to the ground. By switching each set of MOSFETs correctly, the polarity of the actuator can be switched. The actuator is now being charged at $\pm 100V$, and a total of $200V$ voltage difference is achieved.

The switching of the MOSFETs are monitored by three half bridge drivers. When a high signal (10V) from the signal generator enters the two half bridge drivers as shown in Fig. 5.11 b), the high output (H_0) of the drivers will return a high signal, and the low output (L_0) will return a low signal because its corresponding input is a 'not low' ($\overline{L}_{IN}$) input (a 'not low' input will returns a high signal in response to a low signal input, and vise versa). The low output of one of these two drivers enters the third driver, causing the high and low output of this driver to be opposite to the previous two drivers. As a result, the MOSFETs sets connecting to the two oppositely operated drivers will also switch in an opposite manner. The circuit is controlled by one signal source such that minimum phase error can be obtained.

The resistor connected in series with the actuator limits the current being drained from the capacitor, protecting the capacitor from being overloaded, and its power rating was chosen to avoid overheating.

Experiments demonstrated that the polarity switching circuit successfully delivers the required voltage difference to the actuator. At a $20kHz$ operating frequency, the actuator experiences a maximum voltage difference of $200V$.

The workpiece holder and the circuit hardware are shown in Fig. 5.12.

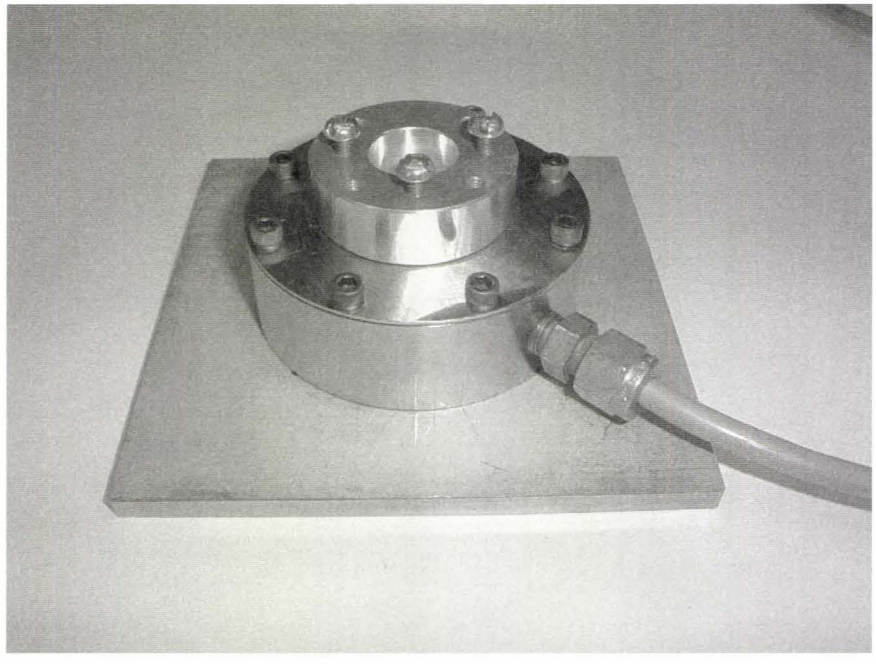

a) Workpiece holder.

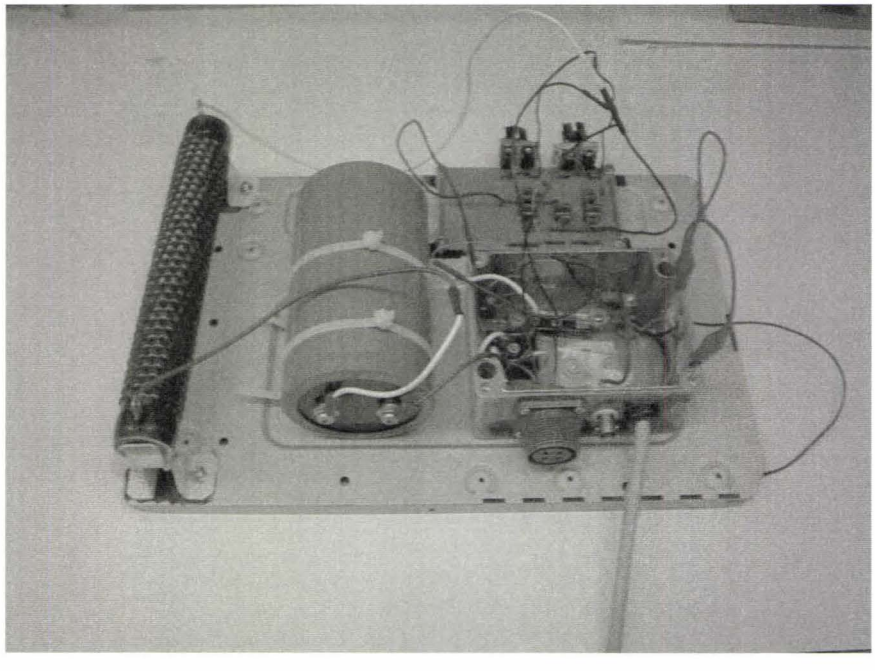

b) Drive circuit.

Figure 5.12: Polarity circuit hardware.

5.6 Conclusion

In the design of the workpiece holder, careful consideration is required to ensure the workpiece can be properly oscillated. A force analysis was carried out to determine the required force delivery from the actuator at a desired frequency and displacement. Actuators available in the current market were investigated, and a BM532 stack actuator manufactured by Sensor Tech. Ltd., which offered the best combination of performance and price, was purchased.

Preload is necessary to protect the actuator, because a piezoelectric stack actuator cannot withstand a high tensile force. In the current design, a circular diaphragm is used to produce the preload. Stainless steel 302 was used to build the diaphragm. Finite element analysis was used to determine the required thickness of the diaphragm to deliver sufficient preload without plastically deformed. The workpiece holder was then designed and built.

Suitable amplifiers available in the current marker were investigated. However, to keep the amplifier as simple and inexpensive as possible, a custom circuit design was considered. The design of the drive circuit involves detailed circuit analysis to ensure sufficient electric power is being delivered. Different drive methods were considered, including an on/off switching circuit, a series RLC resonance circuit, and a polarity switching circuit.

The on/off switching and polarity switching circuits were built and tested. The on/off switching circuit failed in practice. The polarity switching circuit proved to be

successful. This circuit along with the actuator and workpiece holder are used for the ultrasonic assisted drilling experiments presented in the next chapter.

CHAPTER 6

EXPERIMENTS AND DISCUSSION

6.1 Introduction

In this chapter, various experimental investigations on ultrasonic assisted drilling will be presented. Some of the results will be compared with the model predictions presented in Chapter 4.

6.2 Experimental Procedures

Experiments have been carried out with the equipment discussed in chapter 5. Experiments were conducted with a CNC milling machine under different cutting and vibrating conditions. The testing specimens were 25.4 x 25.4 x 1.59 mm (1" x 1" x 1/16") aluminum (1100-0). New standard high speed steel twist drills, which were finished by 'pre-drilling' 3 holes, were used to drill 5 specimens for each test. The maximum burr heights on the tested specimens were measured under a scaled microscope under four different views (see Fig. 6.1). The average was then taken. Burr widths were measured by first measuring the diameter at the base of the burr as well as the actual diameter of the hole using a vernier caliper, then dividing the difference by two. Force measurement was taken during the test by a Kistler table dynamometer. The sampling

frequencies used for 4000, 6000 and 8000RPM spindle speed were 2112, 3200 and 4256Hz respectively.

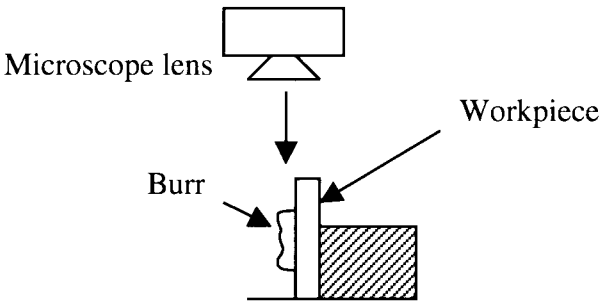

Figure 6.1: Measurement of burr height.

In each set of experiments, the cutting and vibrating conditions were chosen to isolate the vibration frequency, vibration amplitude, spindle speed, cutting feed, and drill diameter and determine their corresponding effect on burr height and width. Table 6.1 summarizes the experiments that have been performed.

The experiments concluded that if the vibration conditions are chosen correctly, ultrasonic assisted drilling could reduce burr size. However, if the vibration conditions are chosen incorrectly, the burr size could increases. It is therefore important to investigate how to choose the suitable vibration conditions. Fig. 6.1 shows some examples of the tested workpieces. All photos were taken under the same scale.

Test #	Sample #	Drill Diameter (mm)	Spindle Speed (rpm)	Feed (mm/s)	Vibration Freq. (kHz)	Pk to Pk Vibration (μm)
1	1-5	3.175	4000	1.905	20	4
2	6-10	3.175	4000	1.905	0	0
3	11-15	3.175	4000	1.905	20	1.33
4	16-20	3.175	4000	1.905	20	2.67
5	21-25	3.175	4000	1.905	15	4
6	26-30	3.175	4000	1.905	10	4
7	31-35	1.587	8000	3.810	0	0
8	36-40	1.587	8000	3.810	20	4
9	41-45	1.587	8000	3.810	20	2.67
10	46-50	1.587	8000	3.810	20	1.33
11	51-55	1.587	8000	3.810	15	4
12	56-60	1.587	8000	3.810	10	4
13	61-65	3.175	6000	1.905	20	4
14	66-70	3.175	6000	1.905	0	0
15	71-75	3.175	8000	1.905	20	4
16	76-80	3.175	8000	1.905	0	0
17	81-85	3.175	8000	3.810	20	4
18	86-90	3.175	8000	3.810	0	0
19	91-95	3.175	8000	5.715	20	4
20	96-100	3.175	8000	5.715	0	0
21	101-105	2.981	8000	3.810	20	4
22	106-110	2.981	8000	3.810	0	0

Table 6.1: Cutting and vibration conditions of the performed experiments.

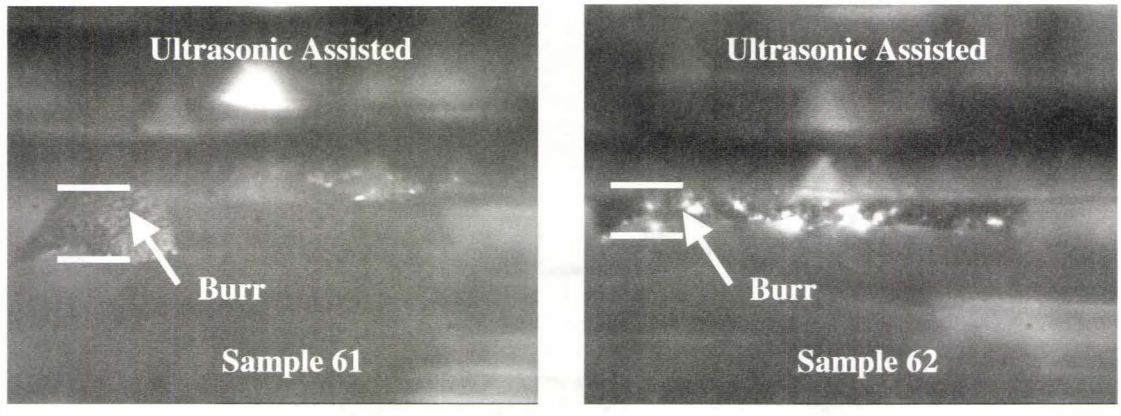

a) 3.175mm drill 6000RPM 1.905mm/s feed; vibrating at 20kHz and 4μm (T13).

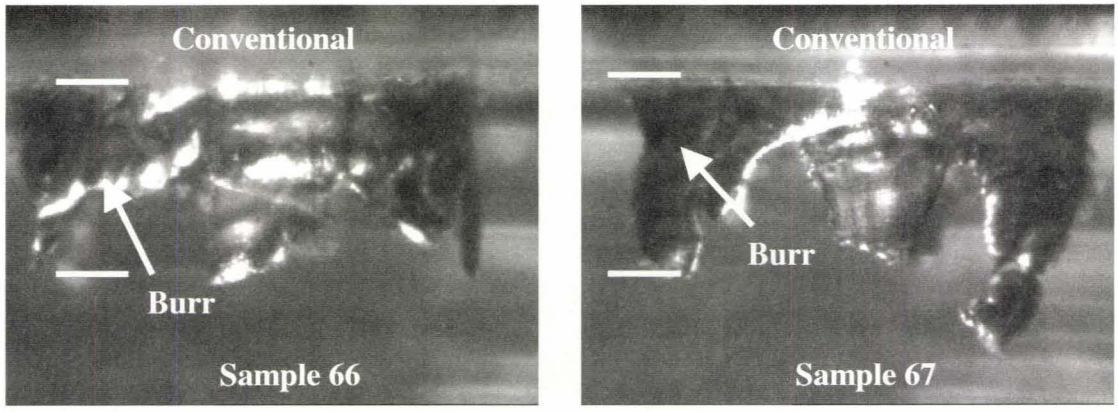

b) 3.175mm drill 6000RPM 1.905mm/s feed without ultrasonic assistance (T14).

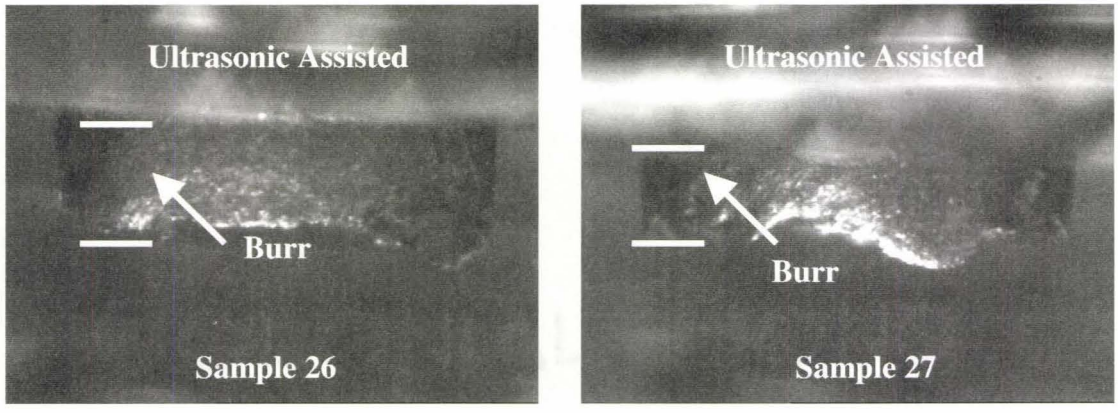

c) 3.175mm drill 4000RPM 1.905mm/s feed; vibrating at 10kHz and 4 μm (T6).

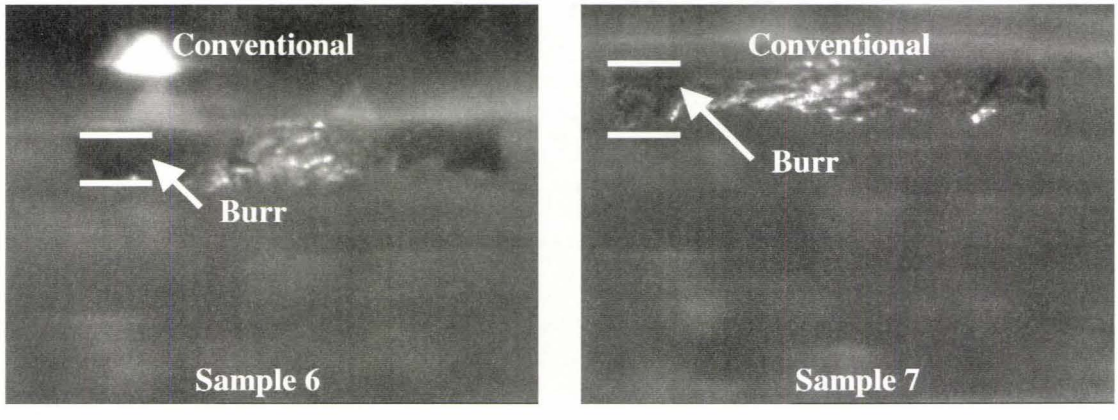

d) 3.175mm drill 4000RPM 1.905mm/s feed without ultrasonic assistance (T2).

Figure 6.2: Some examples of the machined workpiece.

6.3 Experimental Results

6.3.1 Effect of Vibration Frequency

Tests 1, 2, 5 and 6 isolated the vibration frequency by varying the frequency while keeping all other conditions constant. Frequencies tested were 0, 10, 15 and 20kHz. Table 6.2, Fig. 6.3 and 6.4 summarized the results.

Frequency (kHz)	Ave. Burr Height (mm)	Ave. Burr Width (mm)
0	0.546	0.131
10	0.929	0.191
15	0.763	0.174
20	0.384	0.176

Table 6.2: Ave. Burr Height and Width vs Vibration Frequency.

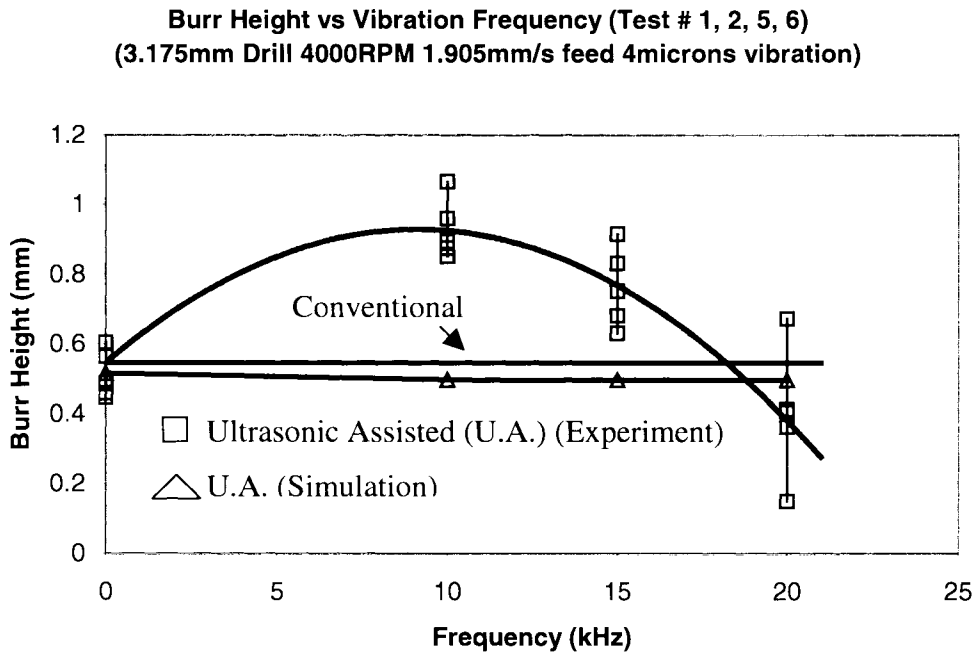

Figure 6.3: Ave. Burr Height vs Vibration Frequency

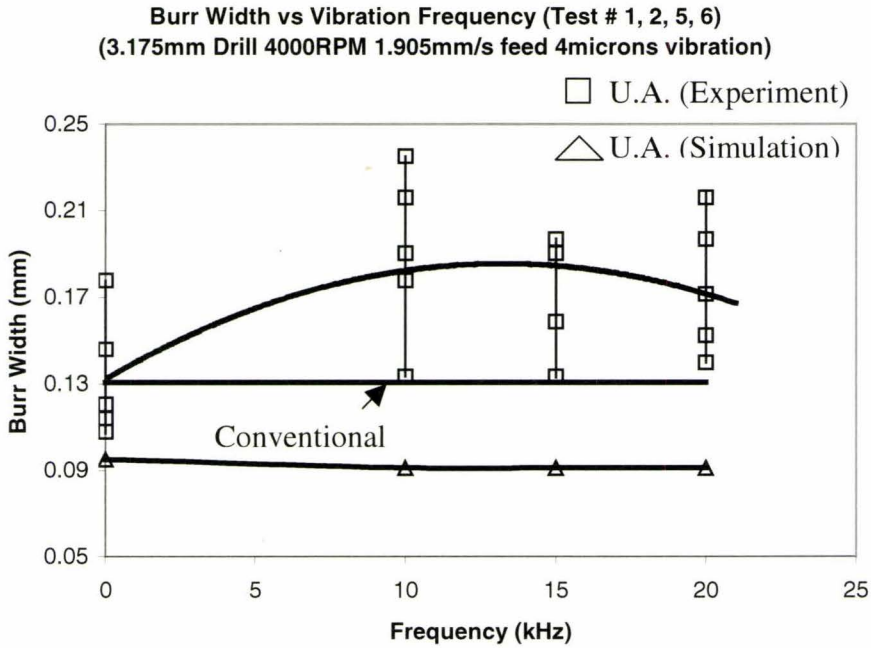

Figure 6.4: Ave. Burr Width vs Vibration Frequency

The results at 20kHz (Test 1) show that the average burr height was decreased by 29% but the average burr width increased by 35%. The trend indicates that the burr height and width decreases after the frequency reaches a threshold. A second order prediction indicates that further increasing the vibration frequency, both burr height and width could reduce. This implies that the higher vibration frequency it is, the smaller the burr height and width are. It was also found that at low vibration frequency, long saw-tooth like chips were formed (Fig. 6.5).

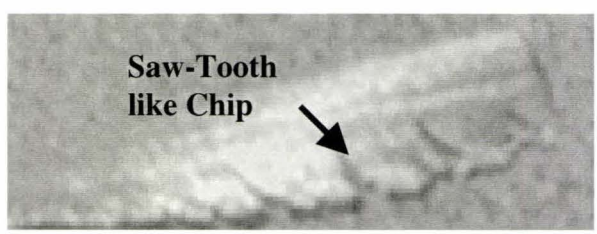

Figure 6.5: Saw-Tooth like Chip

One possible explanation for the formation of these chips is that at low vibration frequency, the axial displacement of the tool due to the feed per each vibration cycle is large enough that the cutting is continuous. In this case no ultrasonic impact action occurs because the tool is always in contact with the workpiece. As a result, long continuous chips were formed, with saw-tooth like shape caused by the ultrasonic vibration. At a higher frequency, the axial feed displacement per each vibration cycle is smaller, allowing the occurrence of ultrasonic impact action, forming fine powdered chips. These fine chips were easy to remove, reducing the thrust force acting on the workpiece. The thrust force measurements of the sample 26 (10kHz) and sample 1 (20kHz) are shown in Fig. 6.6 and 6.7. Fig. 6.8 showed the thrust force comparison between the two vibration frequencies by superimposing the trends of the thrust force within the time where cutting occurs into one graph.

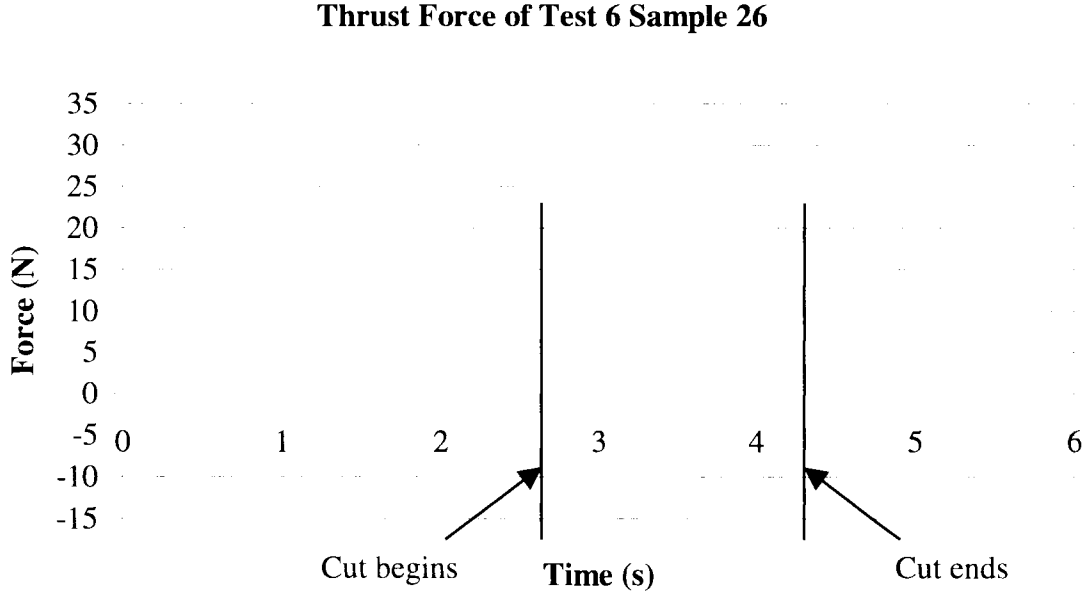

Figure 6.6: Thrust force on sample 26 (U.A. 10kHz 4μm).

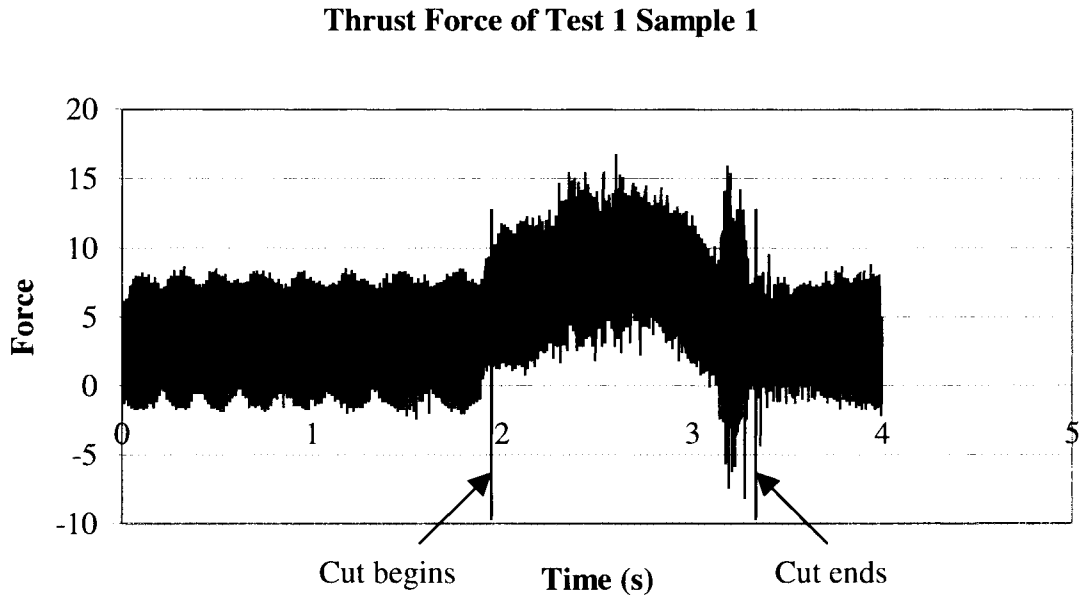

Figure 6.7: Thrust force on sample 1 (U.A. 20kHz 4μm).

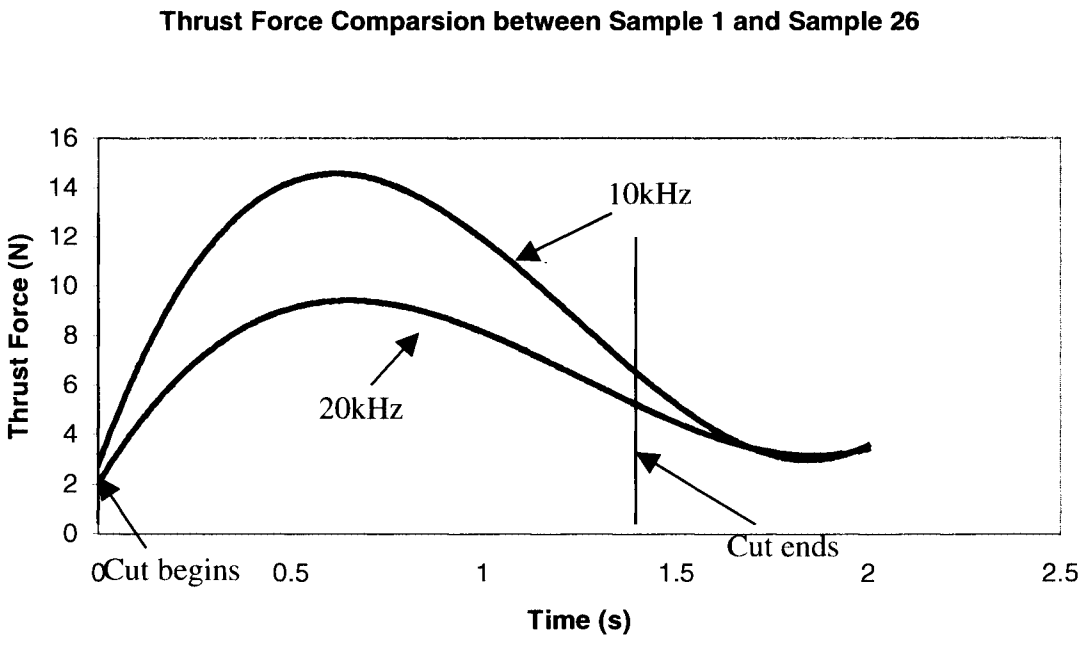

Figure 6.8: Thrust force comparison.

The above results also show the simulation presented in Chapter 4 fails to predict the trend of the burr size. This is most likely due to neglecting the dynamic behavior of the material within the theoretical model.

6.3.2 Effect of Peak to Peak Vibration

Tests 1-4 isolated the effect of the vibration magnitude on the burr size. Peak to peak vibration tested were 0, 1.33, 2.67 and 4μm. Table 6.3, Fig. 6.9 and 6.10 summarize the results.

Peak to Peak (μm)	Ave. Burr Height (mm)	Ave. Burr Width (mm)
0	0.546	0.131
1.33	0.629	0.122
2.67	0.639	0.141
4	0.384	0.177

Table 6.3: Ave. Burr Height and Width vs Vibration Amplitude

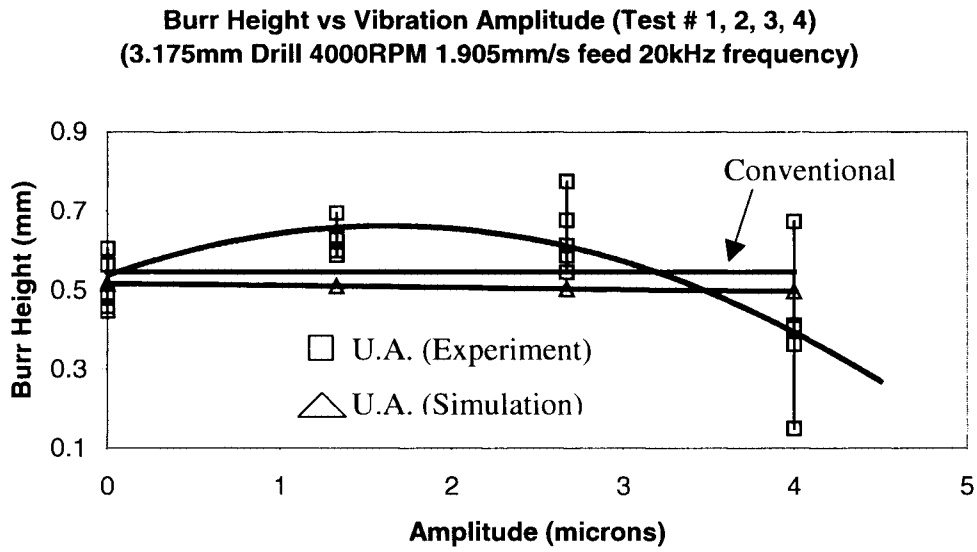

Figure 6.9: Ave. Burr Height vs Vibration Amplitude

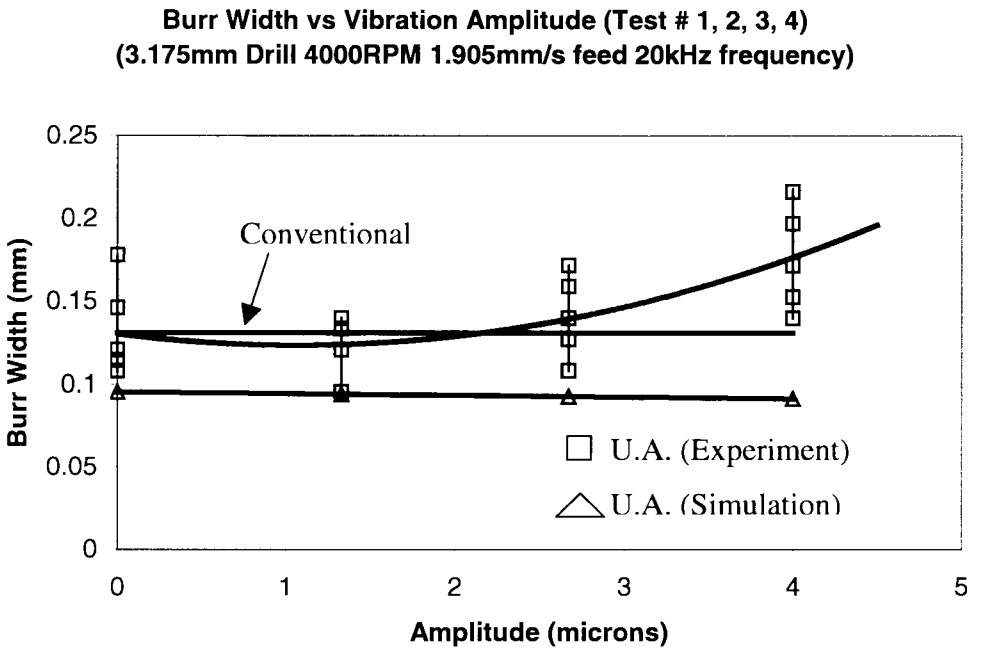

Figure 6.10: Ave. Burr Width vs Vibration Amplitude

Fig. 6.9 and 6.10 demonstrated that the relationship between burr height and width and vibration amplitude is non-linear. After passing through a threshold, as the vibration amplitude increases, the burr height decreases while the burr width increases. Hence, there exists a better operating condition such that burr height can be reduced and the increase in burr width is acceptable. The simulation once again fails to predict the burr width trend.

Similar to vibration frequency, when the peak to peak vibration is small enough, continuous cutting occurs, forming larger chips and burrs. Increasing the peak to peak vibration produces fine chips by the ultrasonic impact actions, reducing the thrust force and the burr height and width.

It is believed that as vibration amplitude increases, the cutting by the ultrasonic impact action dominates. This will cause the force normal to the rake face to be larger than with conventional drilling. This larger force will in turn cause the material to begin to rollover earlier in the cut, resulting in a thicker burr. It is also believed that the higher stiffness of this thicker burr causes it to maintain stronger contact with the cutting lips, causing it to be cut shorter. This is illustrated in Fig. 6.11.

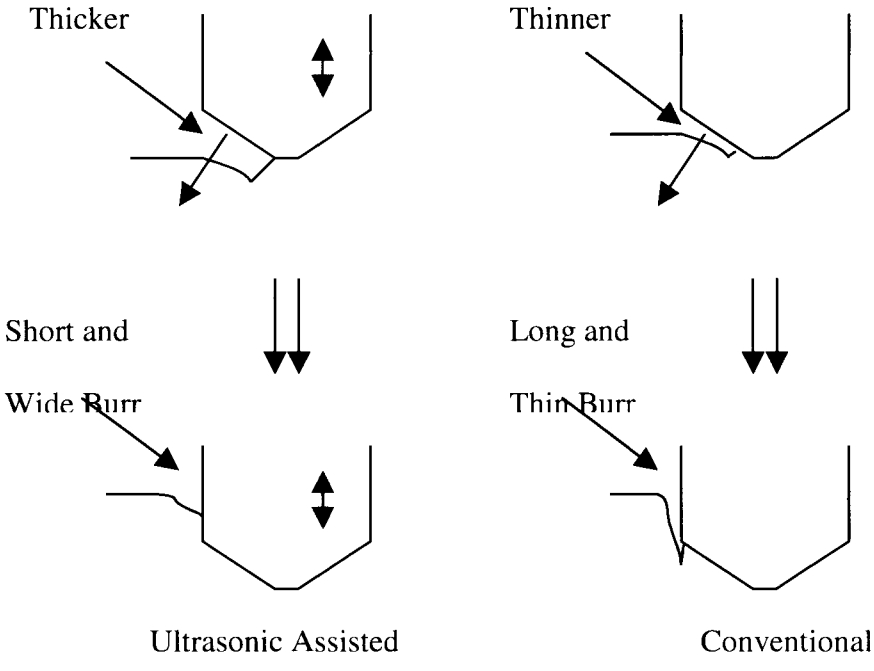

Figure 6.11: The formation of short and wide burr in ultrasonic assisted drilling.

6.3.3 Effect of Spindle Speed

Tests 1, 2 and 13-16 isolated the influence of the cutting speed. Spindle speeds tested were 4000, 6000 and 8000RPM. Table 6.4, fig. 6.12 and 6.13 summarized the results.

	Ultrasonic Assisted		Conventional	
Spindle Speed (RPM)	Burr Height (mm)	Burr Width (mm)	Burr Height (mm)	Burr Width (mm)
4000	0.384	0.176	0.546	0.131
6000	0.285	0.119	0.601	0.244
8000	0.347	0.177	0.784	0.323

Table 6.4: Ave. Burr Height and Width vs Spindle Speed

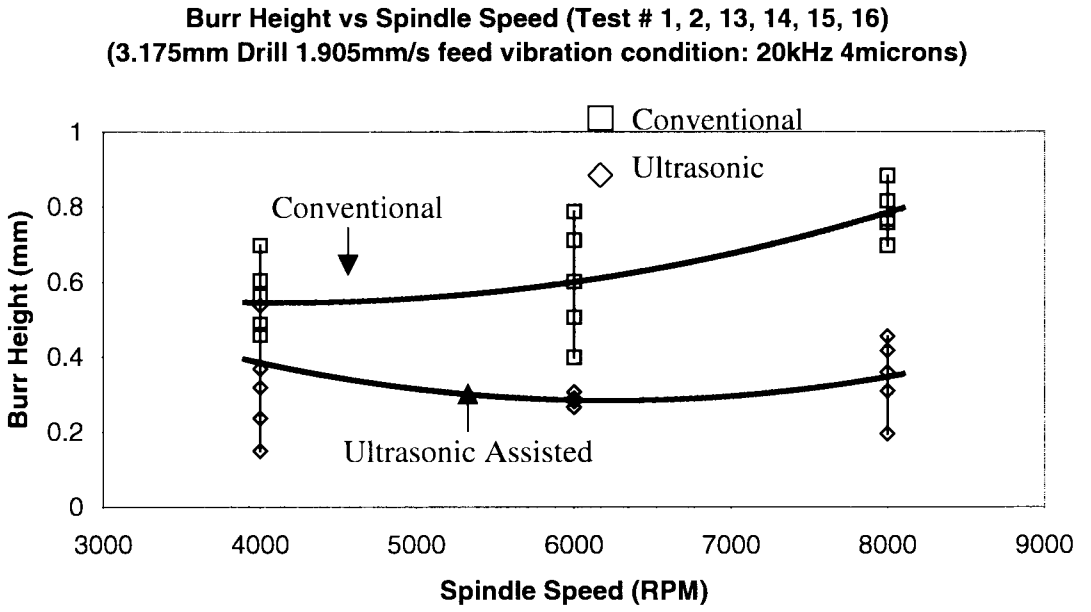

Figure 6.12: Ave. Burr Height vs Cutting Speed

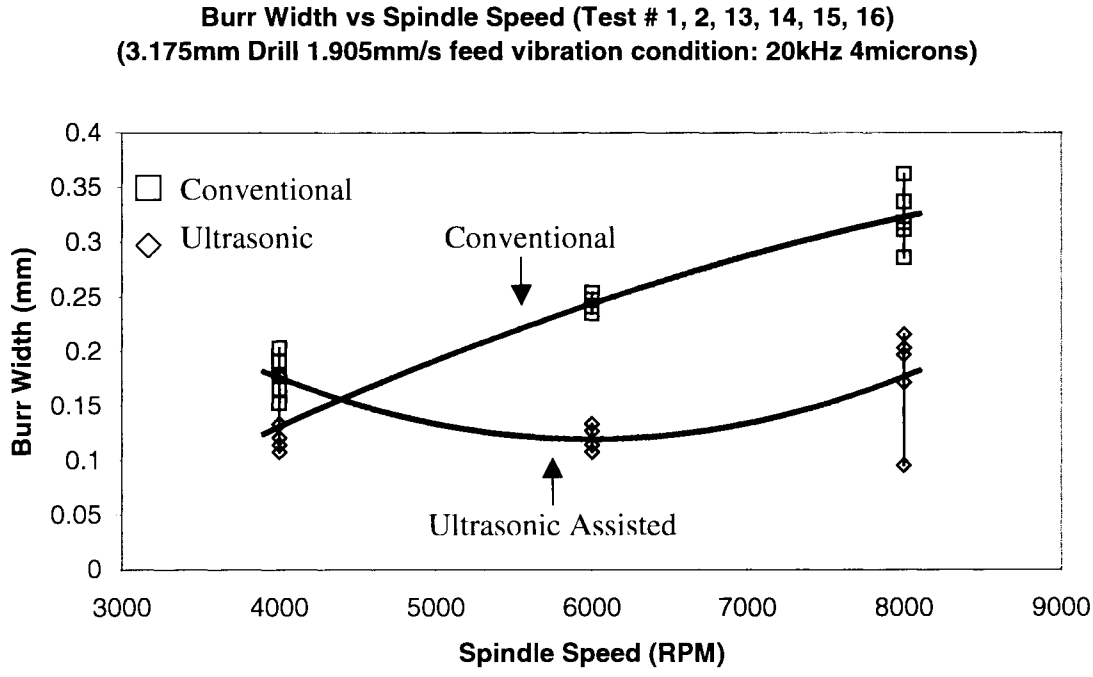

Figure 6.13: Ave. Burr Width vs Cutting Speed

In conventional drilling, the burr size increases with the spindle speed. This is because the thrust force increases with spindle speed and more materials are deformed plastically. However, in ultrasonic drilling, the burr height and width reaches a minimum at 6000RPM with 20kHz and 4μm vibration. This suggested that for a particular cutting condition, there may exists a certain vibration condition that significantly reduces burr size but not necessary with the largest possible vibration frequency and amplitude as others have suggested [11].

On the other hand, there exists a range of vibration conditions that produces a larger burr. Carefully chosen vibration condition is critical for ultrasonic assisted drilling.

The combination of spindle speed and feed determines the primary cutting direction. In general, for conventional drilling, increasing spindle speed with constant feed increases the thrust force. This is because increasing the spindle speed alone will increase the angle between the spindle axis and cutting velocity vector [2]. The result is a decrease in the dynamic rake angle as shown in Fig. 6.14. This will increase the cutting forces.

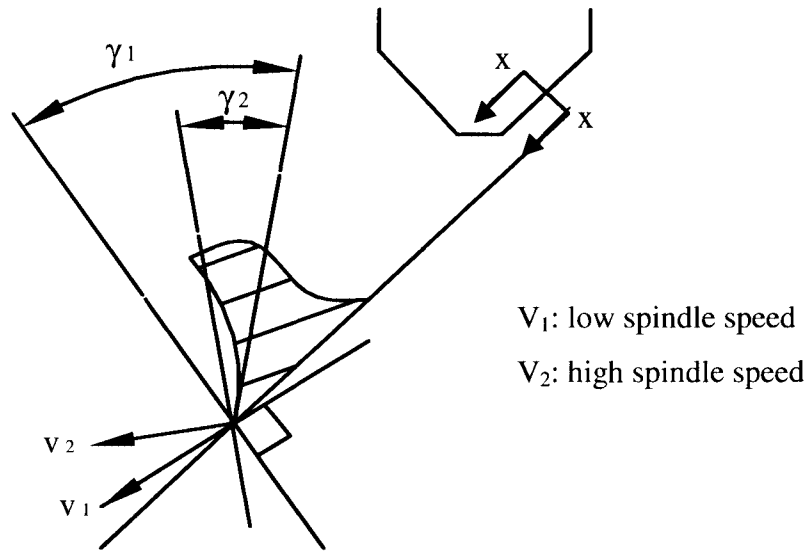

Figure 6.14: Effect of cutting velocity direction on the dynamic rake angle.

However, ultrasonic drilling interferes with feed, allowing exceptions from this general trend. High cutting speed and low feed forms thin chips, and with ultrasonic assistance fine and broken chips are formed and removed from the hole efficiently. Moreover, the direction of the cutting velocity vector changes periodically because of the high frequency oscillation. Therefore the dynamic rake angle changes with time,

reducing the effect of a small dynamic rake angle in conventional drilling. This shows that ultrasonic assisted drilling is particularly beneficial in high speed drilling.

6.3.4 Effect of Cutting Feed

Tests 15-20 isolated the influence of the cutting feed. Cutting feed tested were 1.905, 3.810 and 5.715mm/s (4.5, 9 and 13.5in/min). Table 6.5, Fig. 6.15 and 6.16 summarized the results.

	Ultrasonic Assisted		Conventional	
Cutting Feed (mm/s)	Burr Height (mm)	Burr Width (mm)	Burr Height (mm)	Burr Width (mm)
1.905	0.347	0.177	0.784	0.323
3.810	0.616	0.262	0.504	0.348
5.715	0.374	0.222	0.399	0.251

Table 6.5: Ave. Burr Height and Width vs Cutting Feed

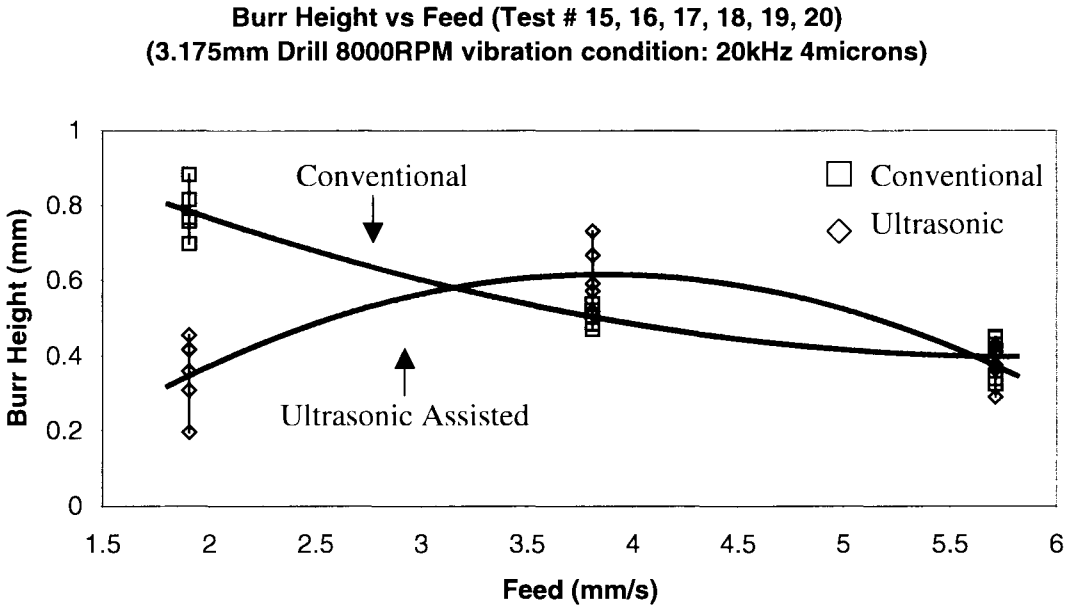

Figure 6.15: Ave. Burr Height vs Cutting Feed

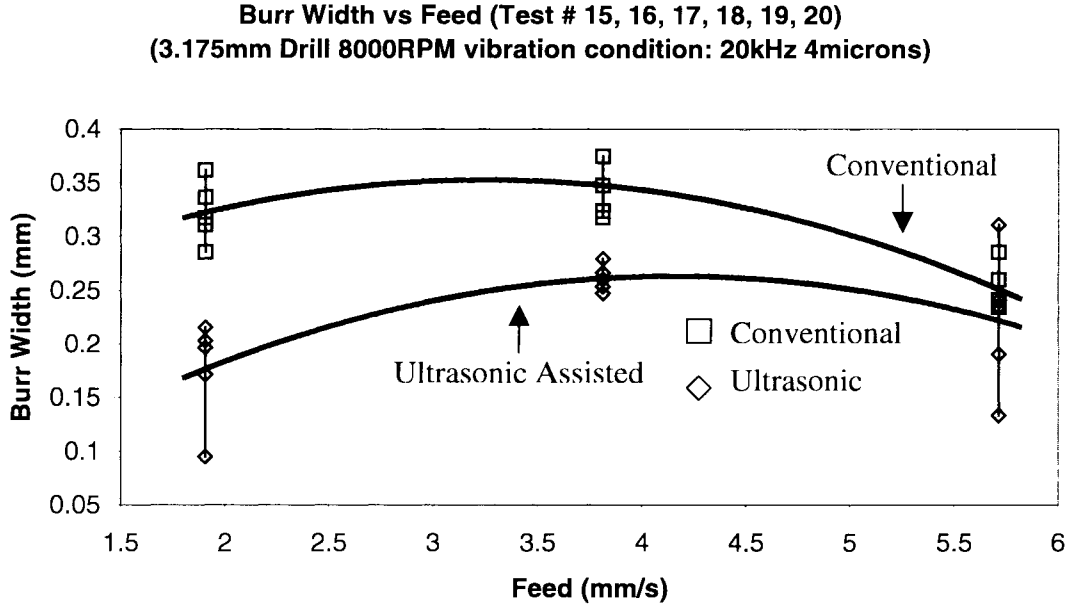

Figure 6.16: Ave. Burr Width vs Cutting Feed

In contrast to the relationship with cutting speed, the burr height and width shows a maximum at 3.810mm/s (9in/min) feed in ultrasonic assisted drilling. It is important to avoid cutting at that point. When compares to conventional drilling, burr height and width were reduced at 5.715mm/s (13.5"/min) feed, which reaches the area of heavy feed, but not significantly. It is also important that ultrasonic assistance reduces burr size significantly under normal feed (4.5"/min).

A similar argument to that presented in section 6.3.1 can be made here. At low feed, primary cutting action in ultrasonic assisted drilling is oblique cutting on the cutting lips. Ultrasonic assistance provides secondary cutting with the ultrasonic impact actions, producing smaller chips and burrs. As the feed increases, the chip segmentation effect is reduced because the larger chips are more difficult to break. It is believed that the burr

height and width can be reduced with high feed drilling by increasing the peak to peak vibration.

6.3.5 Effect of Drill Diameter

Tests 7, 8, 17, 18, 21 and 22 isolated the influence of drill diameter. Drill diameter tested were 1.587, 2.381 and 3.175mm (1/16, 3/32 and 1/8 inch). Table 6.6, fig. 6.17 and 6.18 summarize the results.

	Ultrasonic Assisted		Conventional	
Drill Diameter (mm)	Burr Height (mm)	Burr Width (mm)	Burr Height (mm)	Burr Width (mm)
1.587	0.787	0.255	0.503	0.221
2.981	0.387	0.145	0.287	0.096
3.175	0.616	0.262	0.503	0.348

Table 6.6: Ave. Burr Height and Width vs Drill Diameter

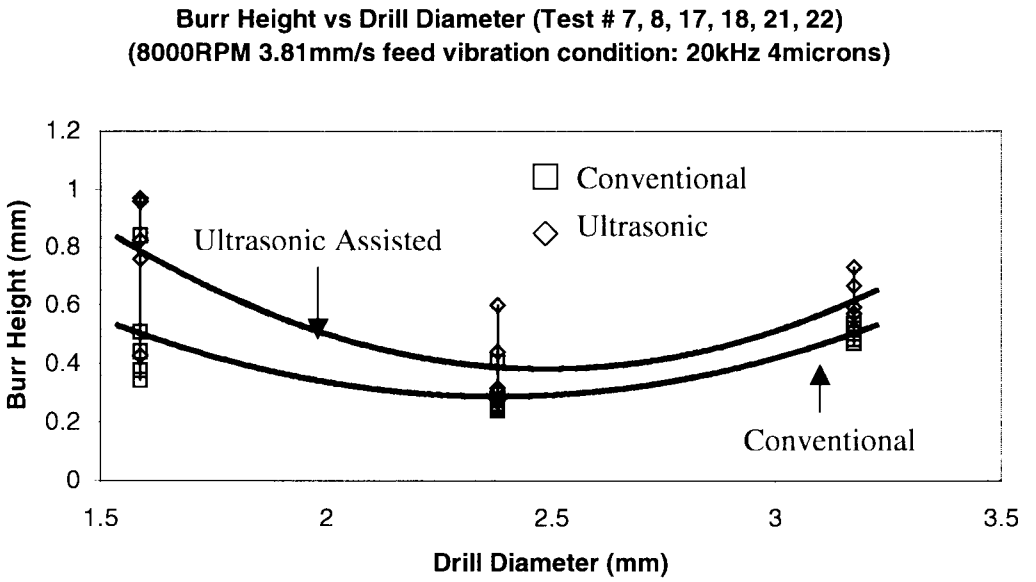

Figure 6.17: Ave. Burr Height vs Drill Diameter

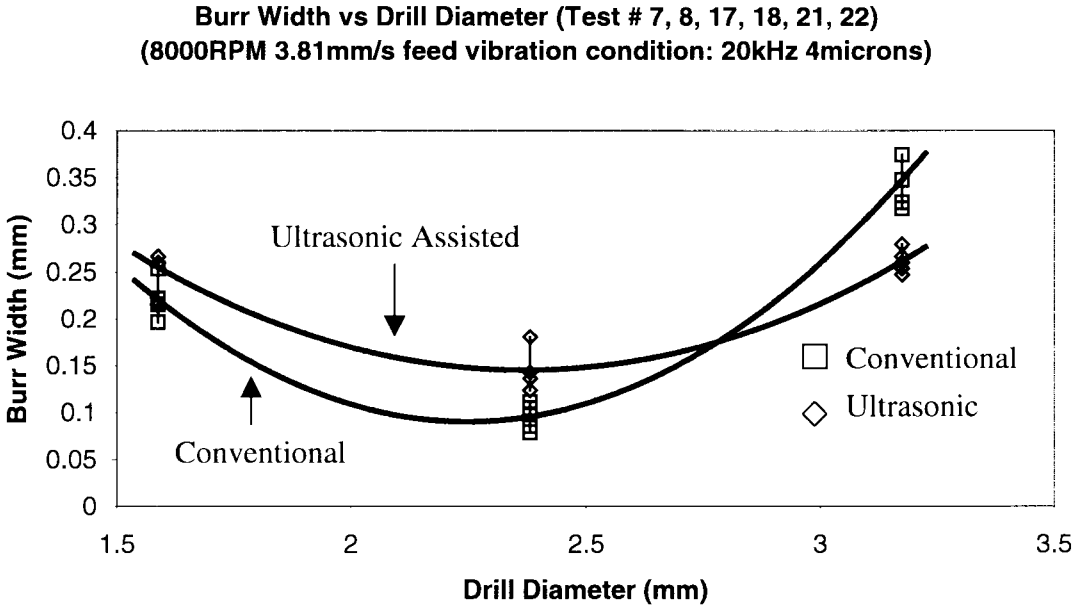

Figure 6.18: Ave. Burr Width vs Drill Diameter

Fig. 6.17 and 6.18 show that there exists a better drill size for a particular cutting condition. 2.981mm (3/32 inch) drill produces the smallest burr height and width at 8000RPM and 9"/min, which is the recommended cutting condition provided by the manufacturer of the drill. Drill diameter determines the total thrust force acting on the workpiece. It is well known that a specific range of cutting conditions is suitable for a particular drill size, and if chosen carefully, burr size can be minimized.

The trends of ultrasonic assisted drilling and conventional drilling are relatively similar, hence it may be concluded that drill size has insignificant effect on the efficiency of ultrasonic assisted drilling. This is logical since the ultrasonic action is axial and therefore not significantly affected by the changes in the radial direction.

6.3.6 Tool Wear

Tool wear plays an important role in metal cutting. Worn tools increase the burr size, cutting forces and undesired vibration. They also reduce the accuracy of the cut. Ultrasonic assisted drilling has demonstrated serious tool wear experimentally. Fig. 6.19 shows two tools, after finishing them with the same method and drilling the same number of holes, one with ultrasonic assistance at 20kHz and 4μm and the other without.

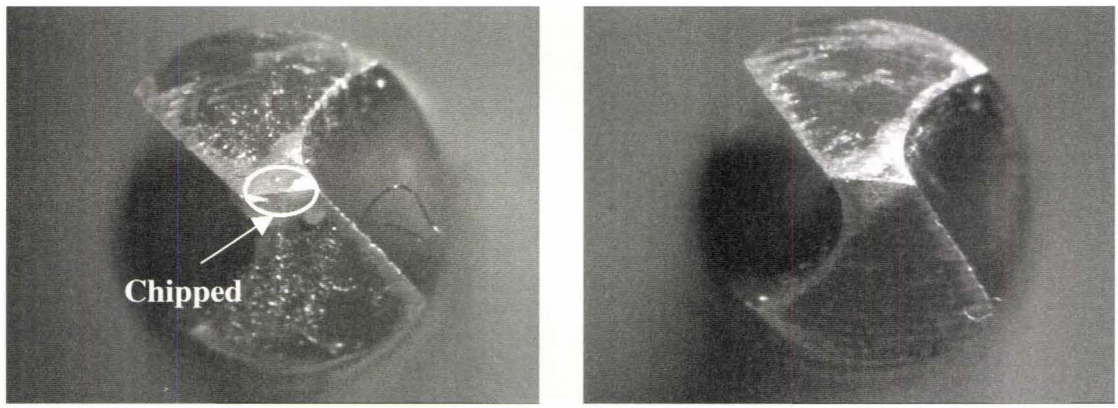

4000RPM
1.905mm/s Feed
Ultrasonic Assisted

4000RPM
1.905mm/s Feed
Conventional

Figure 6.19: Tool Wear Comparison

Both drills are 3.175mm (1/8 inch) diameter standard twisted drill and were used to drill 10 specimens at 4000RPM and 1.905mm/s (4.5in/min) feed. It was found that part of the chisel edge (an area of approximately 0.05mm^2) of the tool after ultrasonic tests was chipped away after the ultrasonic assisted tests. Both chisel wear and cutting lip wear areas were also significantly larger than the tool after conventional tests (0.20mm^2 compared with 0.18mm^2 chisel wear area, and 0.26mm^2 compared with 0.18mm^2 cutting lip wear area). Similar results were found for the other drilling tests discussed in this

thesis. More examples are shown in Fig. 6.20. It was concluded that although ultrasonic assisted drilling serves as an effective way in reducing burr size, it increases tool wear, and therefore reduces tool life.

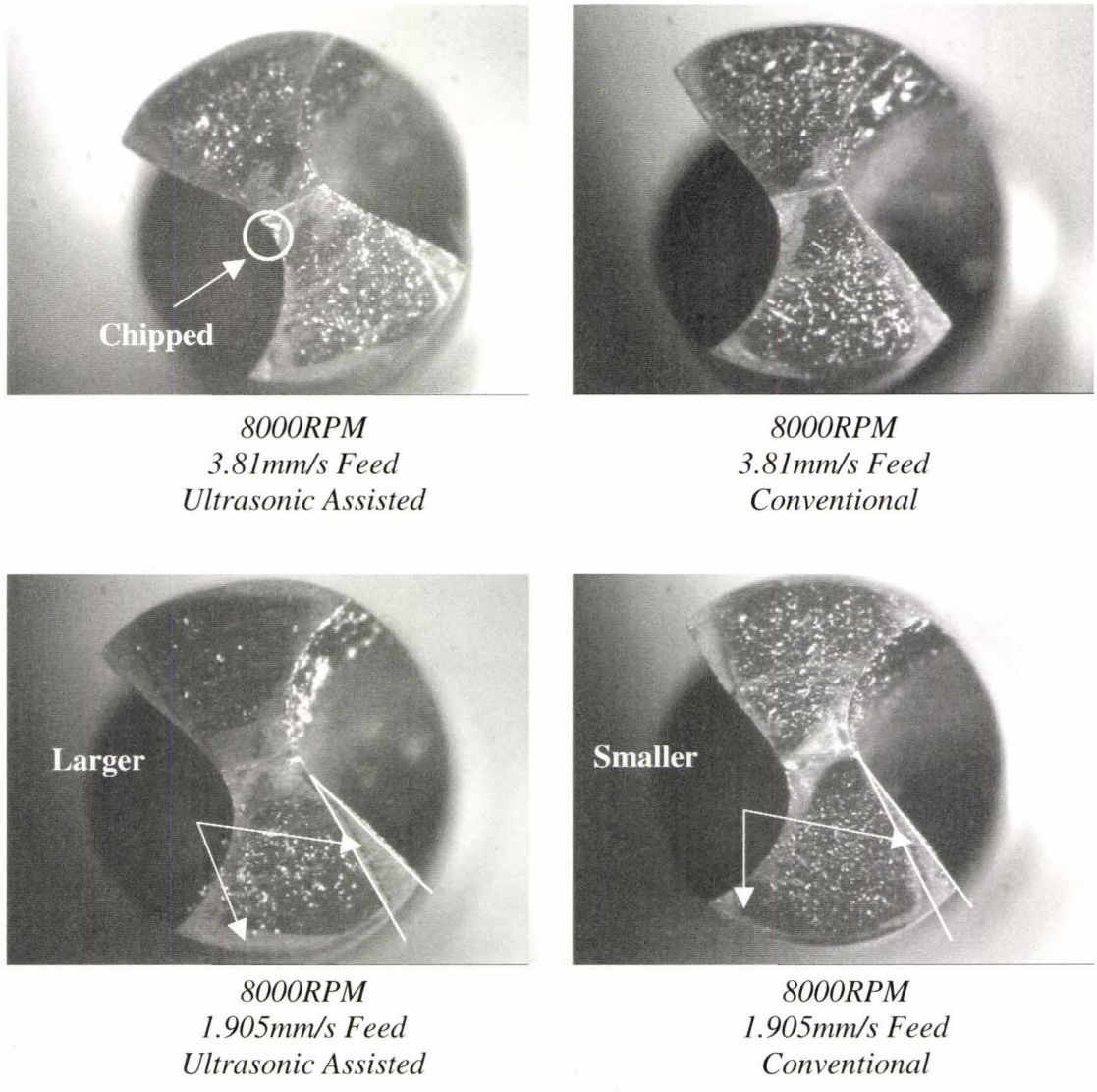

8000RPM
3.81mm/s Feed
Ultrasonic Assisted

8000RPM
3.81mm/s Feed
Conventional

8000RPM
1.905mm/s Feed
Ultrasonic Assisted

8000RPM
1.905mm/s Feed
Conventional

Figure 6.20: Tool wear comparison.

Although it has not been analyzed in details, it is clear that the ultrasonic impact actions and interrupted feed affects the stress level on the tool. The hammering action significantly increases stress concentration on chisel edge and the end of cutting lips, increasing tool wear in these region. It is believed that this is the major causes of tool wear in ultrasonic assisted drilling. Applying suitable coatings on the drill can solve this problem easily, but it will not be discussed in this thesis.

6.3 Conclusion

The experiments have shown that ultrasonic assistance has the potential to reduce burr size. However, under different cutting conditions, different vibration conditions have different effect on burr size and if not chosen carefully, ultrasonic assistance can increases burr size.

The effect of vibration frequency was considered. It was concluded that the vibration frequency must be large enough such that discontinuous cutting can occur. Otherwise long saw-tooth like chip will form, which result in the formation of larger burr.

In the investigation of the effect of peak to peak vibration, it was found that increasing the peak to peak vibration results in smaller burr height but larger burr width. It is believed that at high vibration amplitude, the ultrasonic impact actions dominate, causing the force normal to the rake face to be larger. This larger force will cause the material to rollover earlier in the cut, resulting in a thicker burr. This thicker burr is stiffer, hence maintaining a stronger contact with the cutting lips, resulting in a shorter burr.

It was also found that ultrasonic assisted drilling enables high speed (spindle speed) drilling without increasing the burr size, which conventional drilling does. It is believed that the periodic change in the direction of the cutting velocity vector due to the ultrasonic vibration reduces the effect of small dynamic rake angle compared with conventional drilling. This in turn reduces the thrust force and burr height and width.

In the investigation of the effect of cutting feed, it was found that ultrasonic assisted drilling can significantly reduce the burr size under normal feed. However, in heavy feed drilling, burr size is increased. It was suspected that the chip segmenting effect produced by ultrasonic assisted drilling at heavy feed is not efficient. It is believed that increasing the peak to peak vibration can solve this problem.

From the investigations in all of the experimental results, it is concluded that for each cutting conditions, there exists specific vibration conditions that reduces burr height and width significantly. This conclusion contradicts previous literature, in which recorded that higher frequency and amplitude increases the burr reduction. It was also concluded that the efficiency of ultrasonic assistance is not significantly affected by drill size.

Throughout the experiments, it was found that ultrasonic assistance significantly increases tool wear, especially in the chisel edge area, on standard high speed twist drill. Applying suitable coatings on the drill is recommended in ultrasonic assisted drilling.

CHAPTER 7

CONCLUSIONS AND RECOMMENDATIONS

7.1 Introduction

This thesis outlined the effect of ultrasonic vibration in the feed direction on burr height and width for drilling of 1100-0 aluminum. It was determined that ultrasonic assisted drilling can reduce the burr height and width if the vibration condition is chosen carefully.

Two simulation studies were conducted. A finite element model of orthogonal cutting with and without ultrasonic assistance was first developed. This model simulated the cutting of an aluminum workpiece. Secondly, an exit burr model was established based on a circular plate deflection model. This model also allowed ultrasonic vibration to be included.

Testing equipment was designed and built to obtain experimental results. A piezoelectric actuator was used to drive a workpiece holder at a maximum frequency of 20kHz and 4μm maximum peak to peak vibration. Three electrical circuits were considered to drive the piezoelectric actuator, including the on/off switching circuit, series RLC resonance circuit, and a polarity switching circuit. Both the on/off switching and polarity switching circuits were built and tested. It was shown that the on/off

switching circuit failed, but the polarity switching circuit successfully drove the actuator at the required vibration condition. With the aid of finite element modeling, a workpiece holder consisting of a vibratory diaphragm was design and built, and then used to hold the workpiece during testing.

7.2 Conclusions

1. The experimental results prove that ultrasonic assisted drilling can reduce burr height and width. When the vibration frequency was above a certain threshold (between 15-20 kHz) smaller burrs were produced. It is believed that when the vibration frequency is high enough for a given material and cutting condition, ultrasonic impact actions become significant and cause chip segmentation. This results in fine, powdered chips, reducing the thrust force and burr size. On the other hand, if the vibration frequency is too small, insignificant ultrasonic impact action occurs. Larger chips are formed, increasing thrust force and burr size.
2. It was found that as peak to peak vibration increased the burr height decreased but the burr width increased. It is believed that the ultrasonic impact action dominates when the peak to peak vibration increases, increasing the force normal to the rake face. This force causes the material to begin to rollover earlier, increasing the burr width. However, the deformed material is thicker and stiffer, causing it to maintain a stronger contact with the cutting lips, hence reducing the burr height.

3. The investigations on spindle speed and cutting feed have shown that there exists a better vibration condition for each particular cutting condition, where burr size can be reduced effectively. In other words, carelessly chosen ultrasonic assistance can produce larger burrs. It was also shown that ultrasonic assisted drilling allows a higher spindle speed and feed to be used without increasing the burr size.

4. The investigation on drill size concluded that although drill sizes affect burr sizes significantly, its effect on the efficiency of ultrasonic assisted drilling is insignificant. This is logical because the ultrasonic action is axial and therefore should not be significantly affected by changes in the radial direction.

5. Although ultrasonic assisted drilling demonstrated significant reduction in burr size, it also introduces increased drill wear. After drilling only 10 holes with a particular drill, part of the chisel edge was chipped off, and significant wear on cutting lips was also observed. Similar results were found in the rest of the experiments. Hence, ultrasonic assisted drilling introduces challenges in the context of tool strength and tool life. It must be noted that only standard high speed steel twist drills were tested so better performance may be achieved using drills with suitable coatings.

6. The equipment developed for ultrasonic assistance was cost effective, and successfully drove the workpiece at the necessary vibration conditions.

7. An exit burr model was established to model the effects of ultrasonic assistance on burr size. An effective feed, a combination of drill feed and ultrasonic

vibration, was used to calculate the effective dynamic uncut chip thickness. Deflection of a circular plate was used to model the deflection of the materials below the tool. Unfortunately, the simulation using this model failed to predict the actual burr height and width. It is believed that the failure was due to neglecting the dynamic behavior of the material within the theoretical model.

8. The results from the finite element simulation of orthogonal cutting suggested that ultrasonic vibration is beneficial in reducing burr height and width. However, this conclusion cannot be generalized since the simulations were only performed for one set of cutting conditions. These simulation results also do not necessarily apply to more complex cutting processes.

7.3 Recommendations for Future Work

The following future work is suggested:

- Developing a theoretical exit burr model that includes the dynamic behavior of the material below the tool into consideration.
- Investigating in the possibility of building a series RLC resonance circuit that enables the workpiece to be driven at a higher vibration amplitude with a relatively small power input.
- Extending the current experimental investigations to 30kHz and 10μm to validate the second order predictions regarding the effects of vibration frequency and peak to peak vibration.

REFERENCE AND BIBLIOGRAPHY

1. G. Bone, 1993, Development of an Automated Robotic Edge Deburring System, PhD Thesis, Department of Mechanical Engineering, McMaster University.
2. Elhachimi M., Torbaty S., Joyot P., 1999, Mechanical Modeling of High Speed Drilling (1 and 2), International Journal of Machine Tools and Manufacture 39 (1999), p. 553-581.
3. Zhang L.B., Wang L.J., Liu X.Y., Zhao H.W., Wang X., Luo H.Y., 2001, Mechanical Model for Predicting Thrust and Torque in Vibration Drilling Fibre-reinforced Composite Materials, International Journal of Machine Tools and Manufacture 41 (2001), p. 641-657.
4. Dornfeld D.A., Ko S.L., 1991, A Study on Burr Formation Mechanism, Transactions of the ASME, Journal of Engineering Materials and Technology, January 1991, Vol. 113, p. 75-87.b
5. Dornfeld D.A., Kim J.S., Dechow H., Hewson J., Chen L.J., 1999, Drilling Burr Formation in Titanium Alloy Ti-6Al-4V, Annals of CIRP, 1999, vol. 48, p.73-76.
6. Dornfeld D.A., Guo Y.B., 2000, Finite Element Modeling of Burr Formation Process in Drilling 304 Stainless Steel, Transactions of ASME, Journal of Manufacturing Science and Engineering, November 2000, Vol. 122, p.612-619.

7. Dornfeld D.A., Guo Y., 1998, Finite Element Analysis of Drilling Burr Minimization with a Backup Material, Transactions of NAMRI/SME, Vol. XXVI, 1998, p. 207-212.
8. Dornfeld D.A., Stein J.M., 1997, Burr Formation in Drilling Miniature Holes, Annals of CIRP, vol. 46, p.63-66.
9. Dornfeld D.A., Kim J.S., Dechow H., Hewson J., Chen L.J., 1999, Drilling Burr Formation in Titanium Alloy, Ti-6Al-4V, Annals of CIRP.
10. Saunders Lauderbaugh K.L, Mauch C.A., 2001, An Exit Burr Model for Drilling of Metals, Transactions of ASME, Journal of Manufacturing Science and Engineering, November 2001, Vol. 123, p.562-566.
11. Takeyama H., Kato S., 1991, Burrless Drilling by means of Ultrasonic Drilling, Annals of CIRP, 1991, vol. 40, p.83-86.
12. h3dmap, supplied program in course ME705, Department of Mechanical Engineering, McMaster University.
13. Trent and Wright, Metal Cutting, Butterworth Heinemann, 2000.
14. Conway H.D., Ithaca N.Y., 1948, The Bending of Symmetrically Loaded Circular Plates of Variable Thickness, Journal of Applied Mechanics, March, 1948, p.1-6.
15. Personal Communication, EDO representative, Sept. 15, 2001.
16. Kim J.D., Nam S.R., 1995, Development of a Micro-Depth Control System for an Ultra-Precision Lathe using a Piezo-electric Actuator, International Journal of Machine Tools and Manufacture, Vol. 37, No. 4, p. 495-509, 1997.

17. Chern G.L., Dornfeld D.A., 1996, Burr/Breakout Model Development and Experimental Verification, Transactions of the ASME, Journal of Engineering Materials and Technology, , April 1996, Vol.118, p. 201-206.

18. Gillespie L.K., Blotter P.T., 1976, The Formation and Properties of Machining Burrs, Transactions of the ASME, Journal of Engineering for Industry, February 1976, p.66-74.

19. Hashimura M., Ueda K., Dornfeld D.A., Manabe K., Analysis of three-dimensional Burr Formation in Oblique Cutting, Annals of CIRP, Vol. 44/1/1995, p.27-30.

20. Kim J.D., Kim D.S., 1998, Waviness Compensation of Precision Machining by Piezo-electric Micro Cutting Device, International Journal of Machine Tool and Manufacture 38 (1998), p.1305-1322.

21. Kim. J.D., Nam S.R., 1995, An Improvement of Positioning Accuracy by use of Piezoelectric Driven Micropositioning System Simulation, Mech. Mach. Theory, Vol.30, No.6, p.819-827, 1995.

22. Kim J., Min S. Dornfeld D.A., 2001, Optimization and Control of Drilling Burr Formation of AISI 304L and AISI 4118 based on Drilling Burr Control Charts, International Journal of Machine Tools and Manufacture 41 (2001), p.923-936.

23. Lin T.R., Shyu R.F., 2000, Improvement of Tool Life and Exit Burr using Variable Feeds when Drilling Stainless Steel with Coated Drills, International Journal of Advanced Manufacturing Technology (2000) Vol.16, p.308-313.

24. Moriwaki T., Shamoto E., 1995, Ultrasonic Elliptical Vibration Cutting, Annals of CIRP, Vol.44/1/1995, p.31-34.

25. Murakawa M., Jin M., 1998, Turning of Beta-Titanium Alloys by means of Ultrasonic Vibration, Transactions of NAMRI/SME, Vol. XXVI, 1998, p.153-158.

26. Nakayama K., Arai M., 1987, Burr Formation in Metal Cutting, Annals of CIRP, Vol.36/1/1987, p.33-36.

27. Pande S.S., Relekar H.P., 1986, Investigations of Reducing Burr Formation in Drilling, International Journal of Machine Tool Design and Research, 1986, Vol.26, No.3, p.339-348.

28. Park I.W., Dornfeld D.A., 2000, A Study of Burr Formation Processes using the Finite Element Method: Part I, Transactions of the ASME, Journal of Engineering Materials and Technology, April 2000, Vol.122, p.221-228.

29. Shamoto E., Moriwaki T., 1994, Study on Elliptical Vibration Cutting, Annals of CIRP, Vol.43/1/1994, p.35-38.

30. Takeyama H., Iijima N., 1998, Machinability of Glassfiber Reinforced Plastics and Application of Ultrasonic Machining, Annals of CIRP, Vol.37/1/1988, p.93-96.

31. Tzou H.S., 1991, Design of a Piezoelectric Exciter/Actuator for Micro-Displacement Control: Theory and Experiment, Precision Engineering, April 1991, Vol.13, No.2, p.104-110.

32. Wang L.P., Wang L.J., He Y.H., Yang Z.J., 1998, Prediction and Computer Simulation of Dynamic Thrust and Torque in Vibration Drilling, Proc. Instn. Mech. Engrs. 1998, Vol.212 Part B, p.489-497.

33. Weber H., Herberger J., Pilz R., 1984, Turning of Machinable Glass Ceramics with Ultrasonic Vibrated Tool, Annals of CIRP, Vol.31/1/1984, p.85-87.

34. Zhang D.Y., Wang L.J., 1998, Investigation of Chip in Vibration Drilling, International Journal of Machine Tools and Manufacture, 1998, Vol.38, No.3, p.165-176.

Appendix A

Ultrasonic Assisted Drilling Workpiece Holder Design Drawings

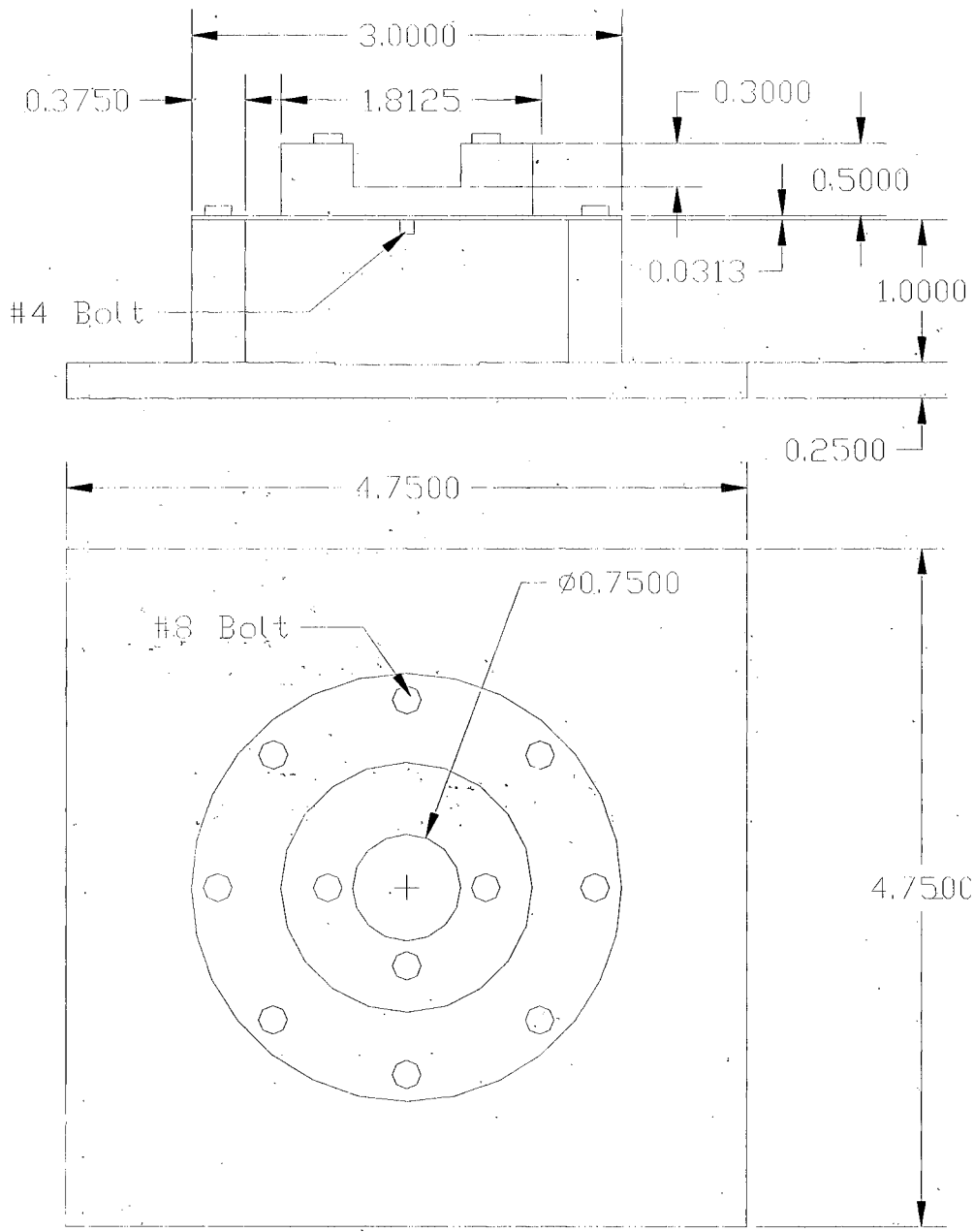

Ultrasonic Assisted Drilling
Workpiece Holder Design

McMaster University
Department of Mech. Eng.

Notes: Units in inches

Last Modified: Jan 31, 2002.